

Analysis Note of the Experiment

Supplementary note on diffractive analyses of 2015 proton-proton data:

- [1] Measurement of Central Exclusive Production of $h\bar{h}$ pairs ($h = \pi, K, p$) with Roman Pot detectors in diffractive proton-proton interactions at $\sqrt{s} = 200$ GeV
- [2] Measurement of particle production with Roman Pot detectors in diffractive proton-proton interactions at $\sqrt{s} = 200$ GeV

Leszek Adamczyk¹, Łukasz Fulek¹, and Rafał Sikora¹

¹*AGH University of Science and Technology, FPACS, Kraków, Poland*

June 5, 2018

Abstract

In this note we present supplementary material related to analyses of diffractive processes based on 2015 data from proton-proton collisions at $\sqrt{s} = 200$ GeV. This dataset was collected with newly installed Roman Pot detectors in Phase II* configuration which ensured efficient triggering and measuring diffractively scattered protons.

We focus on calculation of efficiencies, corrections to Monte Carlo simulations and derivation of systematic uncertainties of our measurements.

Contents

1 Efficiencies	3
1.1 TPC track acceptance and reconstruction efficiency	3
1.2 TOF acceptance, hit reconstruction and track-matching efficiency	16
1.3 TPC vertex reconstruction efficiency	29
2 Energy Loss Correction	30
3 Roman Pot simulation	31
4 dE/dx correction	32
5 TPC track pointing resolution adjustment	36
6 Dead material in front of TPC	39
7 Systematic errors	42
7.1 TPC track reconstruction efficiency systematics	42
7.2 TOF matching efficiency systematics	43
7.3 Dead material correction to TPC track reconstruction efficiency	44
Appendix A Energy Loss Correction	48
Appendix B Dead material correction to TPC track reconstruction efficiency	49
List of Figures	67
List of Tables	67
References	68

1. Efficiencies

1.1 TPC track acceptance and reconstruction efficiency

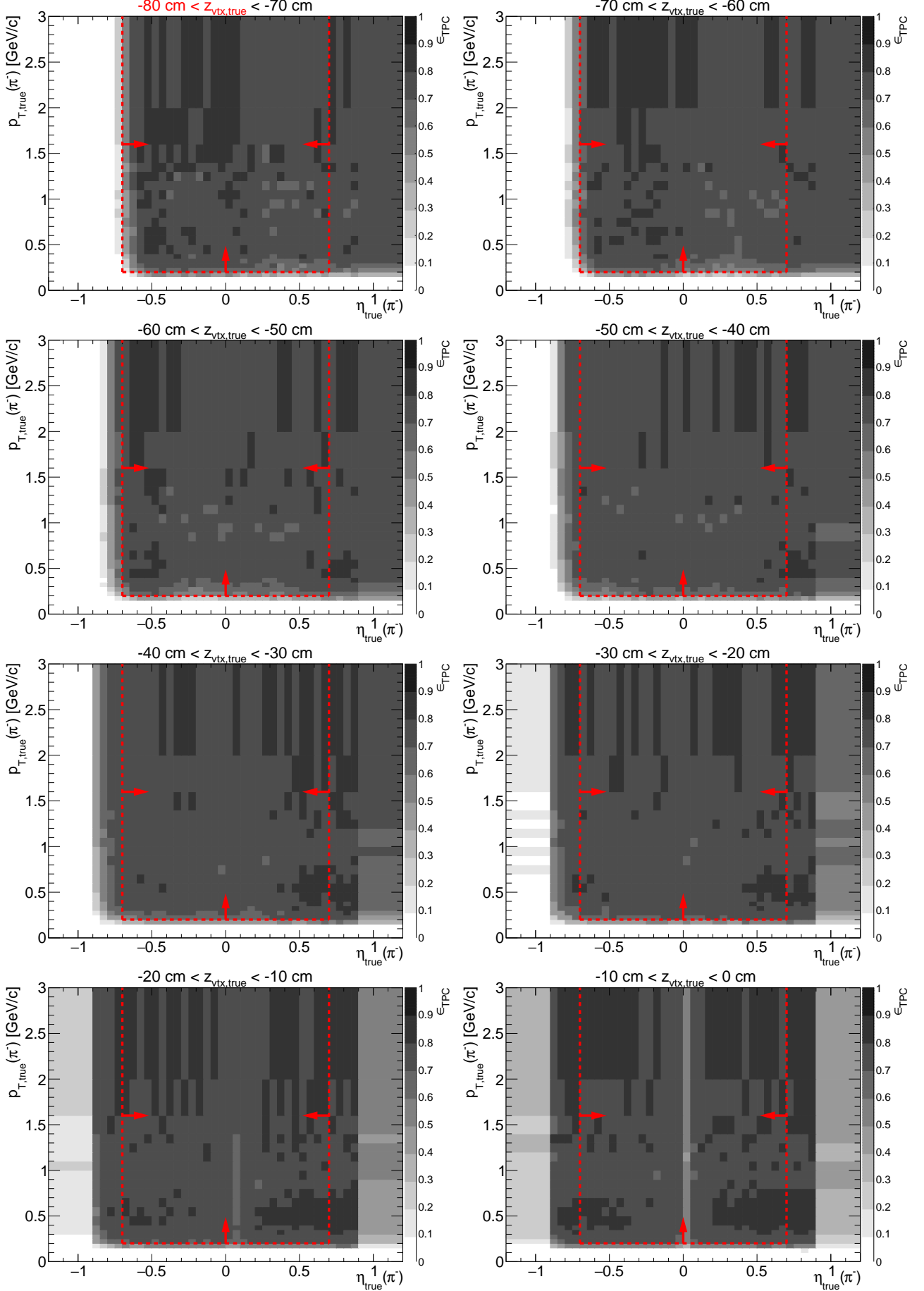
We define joint acceptance and efficiency of the reconstruction of a track in the TPC, ϵ_{TPC} , as the probability that particle from the primary interaction generates signal in the detector which is reconstructed as a track that satisfies all quality criteria and whose p_T and η are within the kinematic region of the measurement (cuts ?? and ??).

Thechnically this quantity is derived from STARsim MC embedded into zero-bias triggers in the following procedure:

1. True-level primary particles of given ID and charge, with all physics (p_T^{true} , η^{true}) and detector (z_{vx}) quantities within defined region of the measurement, are selected (*set A*).
2. Each particle from *set A* is checked if global TPC track with more than half of hit points generated by this particle, was reconstructed. All global tracks which are associated with true-level primary particles and satisfy kinematic and quality criteria (cuts ?? and ??), form *set B*.
3. The joint TPC acceptance and efficiency is calculated as the ratio of the histograms of true-level quantities (such as p_T , η , z_{vx}) for particles from *set B* and particles from *set A*:

$$\epsilon_{\text{TPC}}(p_T, \eta, z_{vx}; \text{sign, PID}) = \frac{(p_T, \eta, z_{vx}) \text{ histogram for particles of given sign and ID from } \textit{set B}}{(p_T, \eta, z_{vx}) \text{ histogram for particles of given sign and ID from } \textit{set A}}. \quad (1.1)$$

Figure 1.1: TPC acceptance and reconstruction efficiency of π^- . Each plot represents the TPC efficiency ϵ_{TPC} (z -axis) as a function of true particle pseudorapidity η (x -axis) and transverse momentum p_T (y -axis) in single z -vertex bin whose range is given at the top. Red lines and arrows indicate region accepted in analyses.



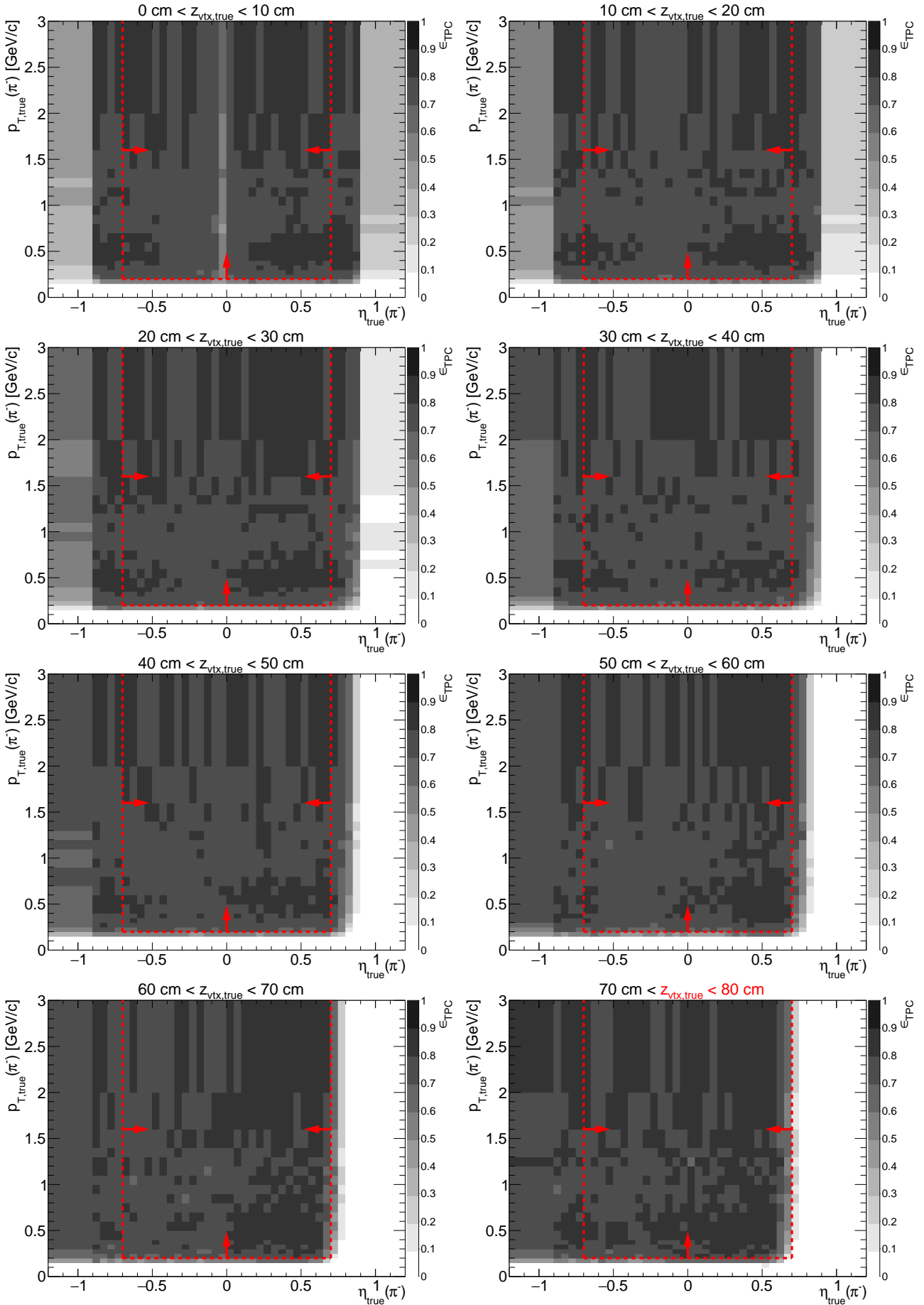
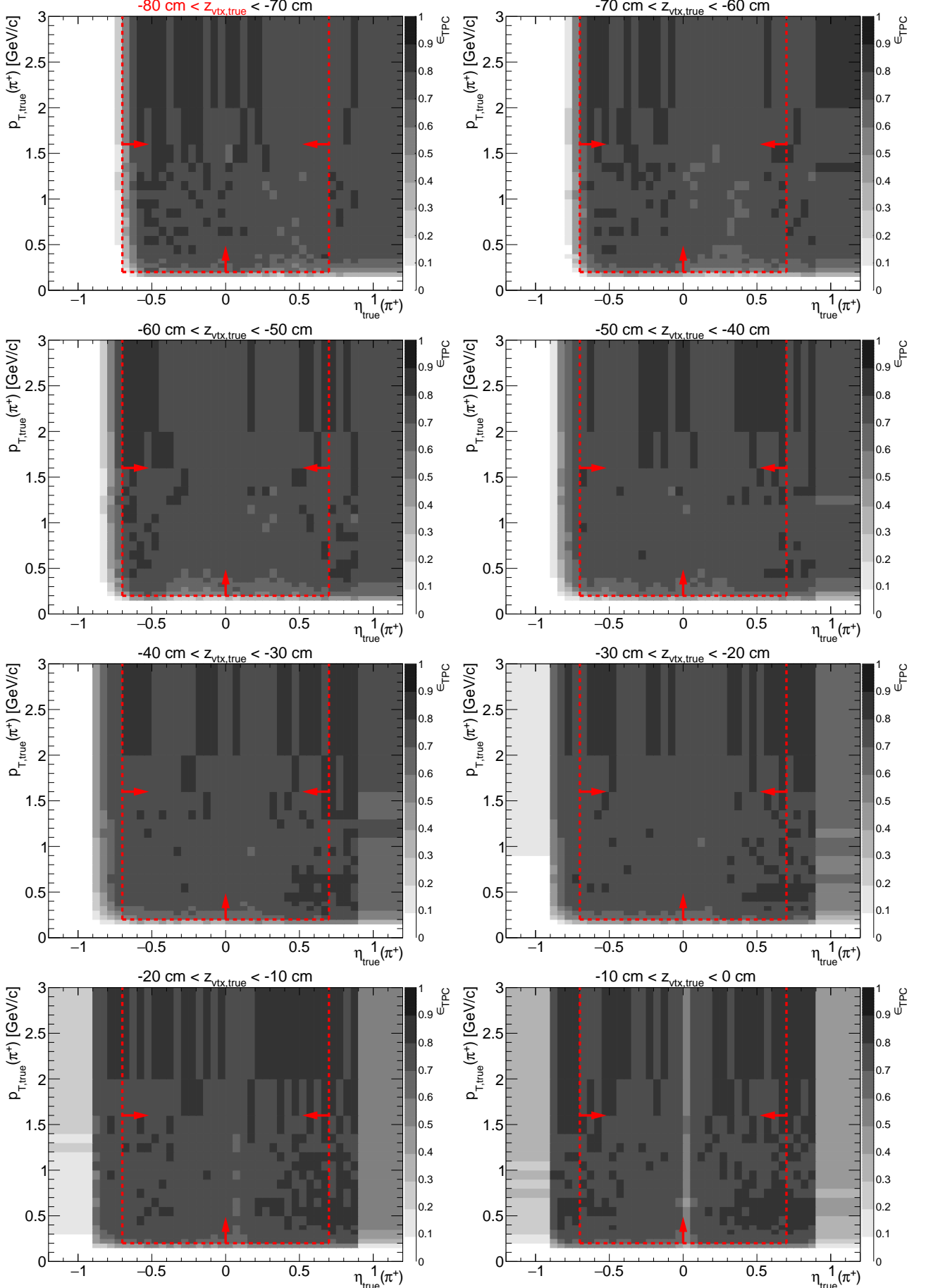


Figure 1.2: TPC acceptance and reconstruction efficiency of π^+ . Each plot represents the TPC efficiency ϵ_{TPC} (z -axis) as a function of true particle pseudorapidity η (x -axis) and transverse momentum p_T (y -axis) in single z -vertex bin whose range is given at the top. Red lines and arrows indicate region accepted in analyses.



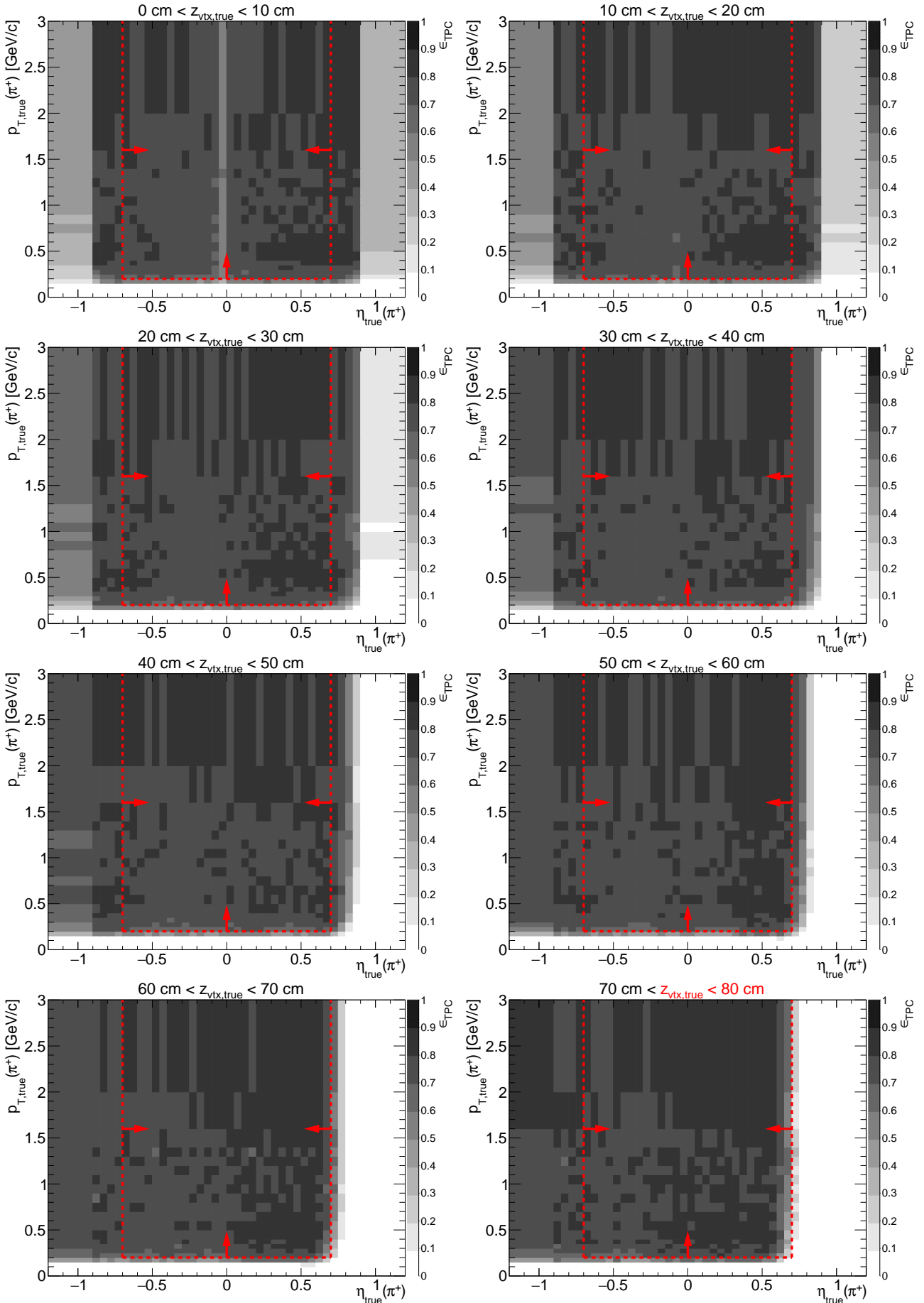
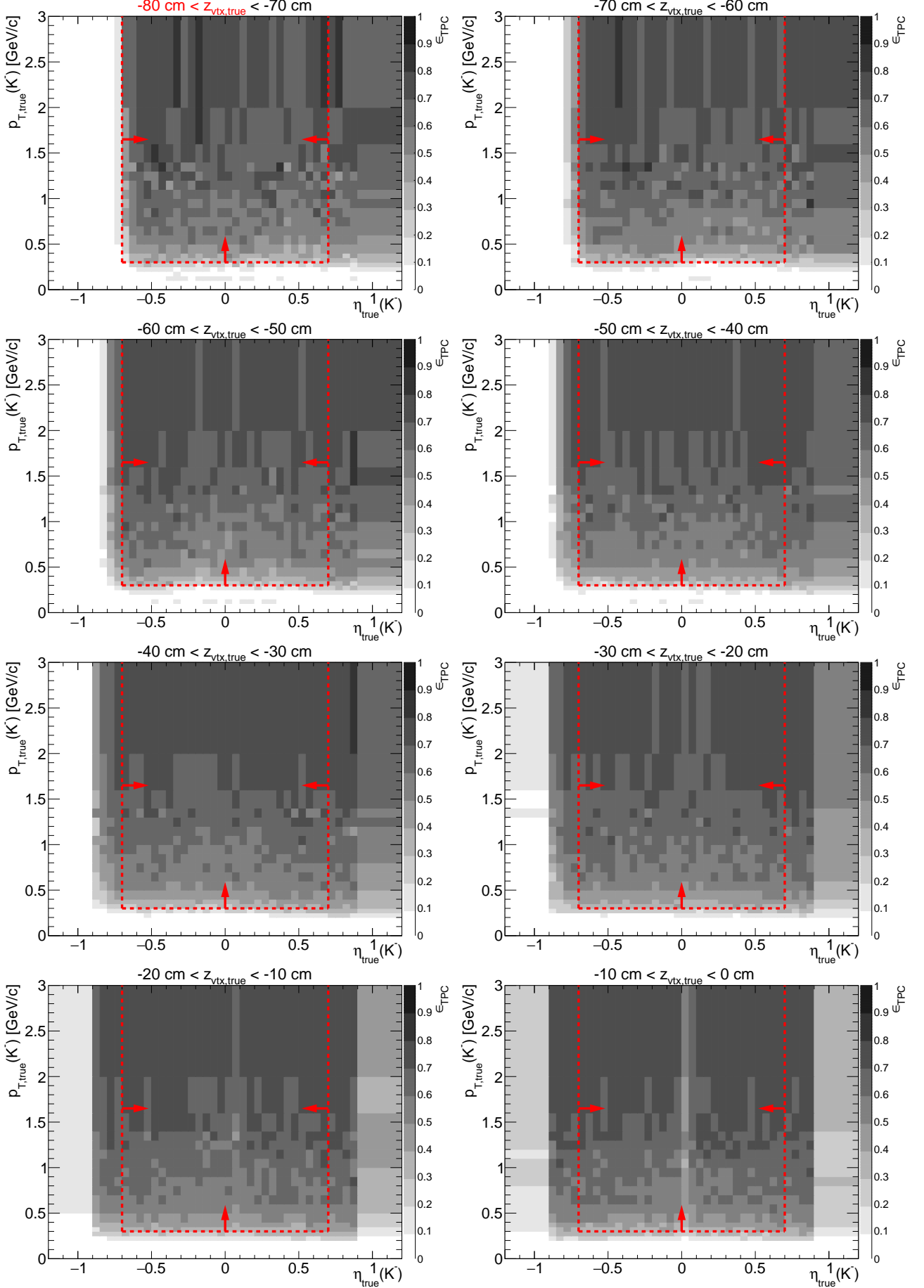


Figure 1.3: TPC acceptance and reconstruction efficiency of K^- . Each plot represents the TPC efficiency ϵ_{TPC} (z -axis) as a function of true particle pseudorapidity η (x -axis) and transverse momentum p_T (y -axis) in single z -vertex bin whose range is given at the top. Red lines and arrows indicate region accepted in analyses.



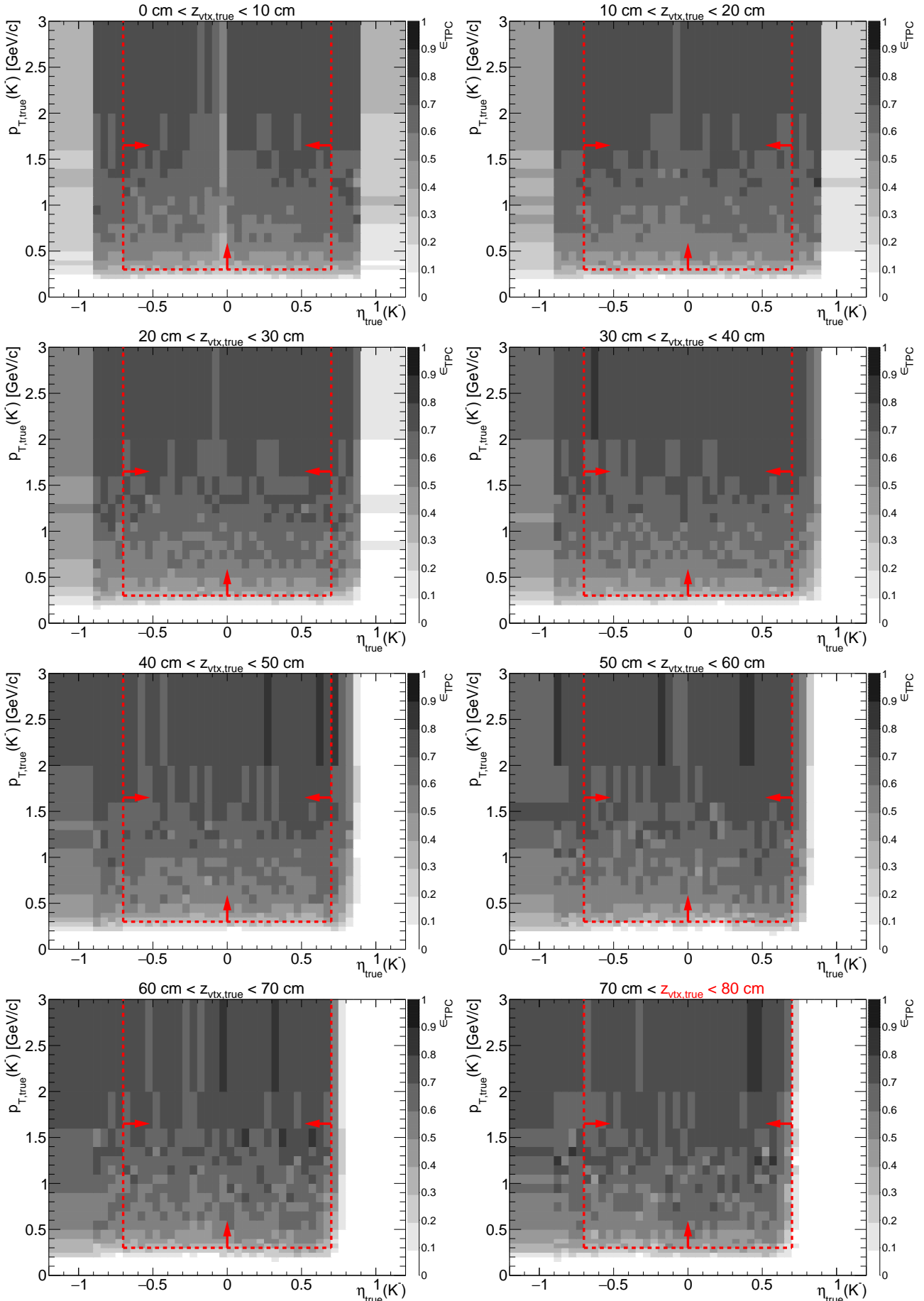
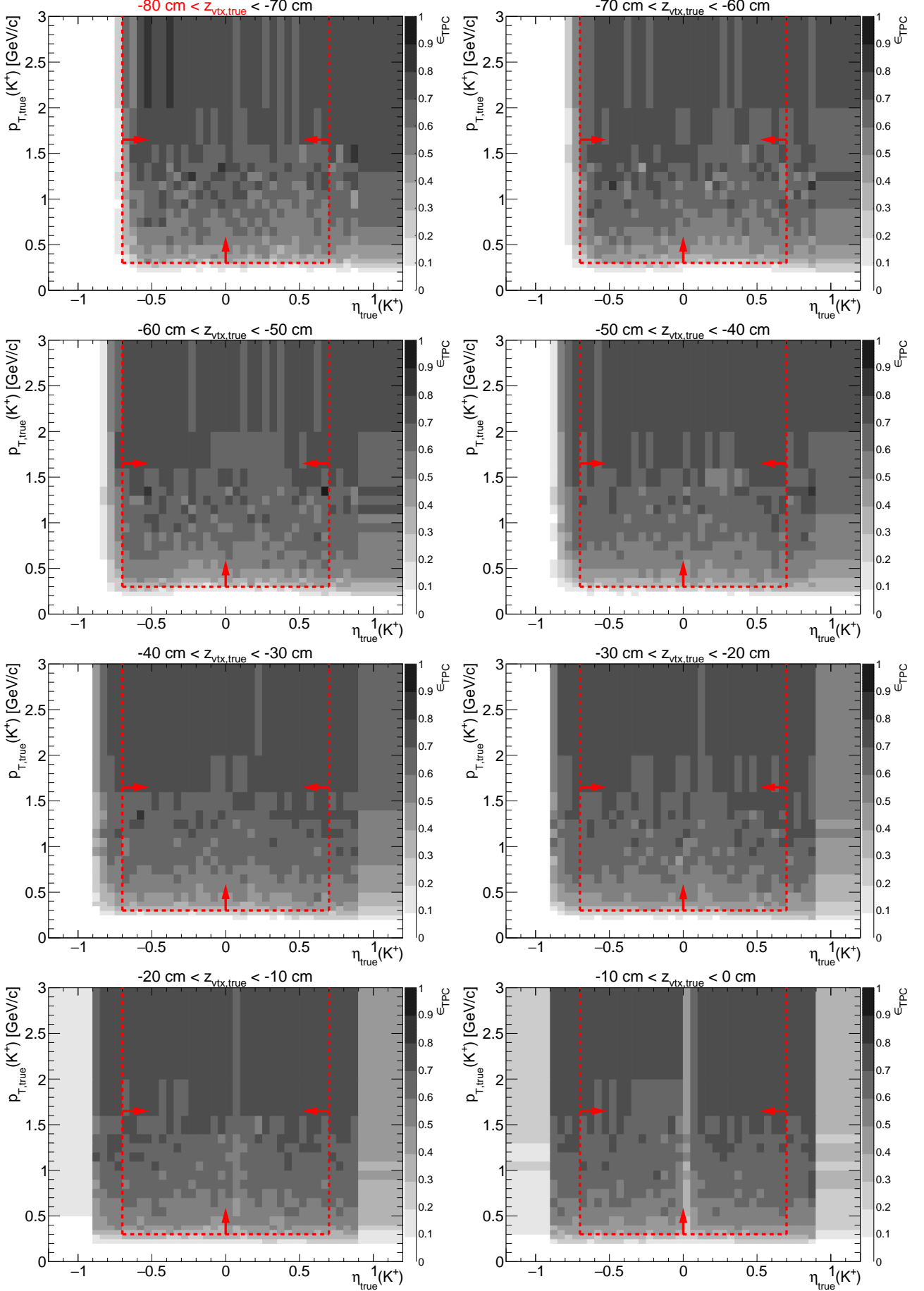


Figure 1.4: TPC acceptance and reconstruction efficiency of K^+ . Each plot represents the TPC efficiency ϵ_{TPC} (z -axis) as a function of true particle pseudorapidity η (x -axis) and transverse momentum p_T (y -axis) in single z -vertex bin whose range is given at the top. Red lines and arrows indicate region accepted in analyses.



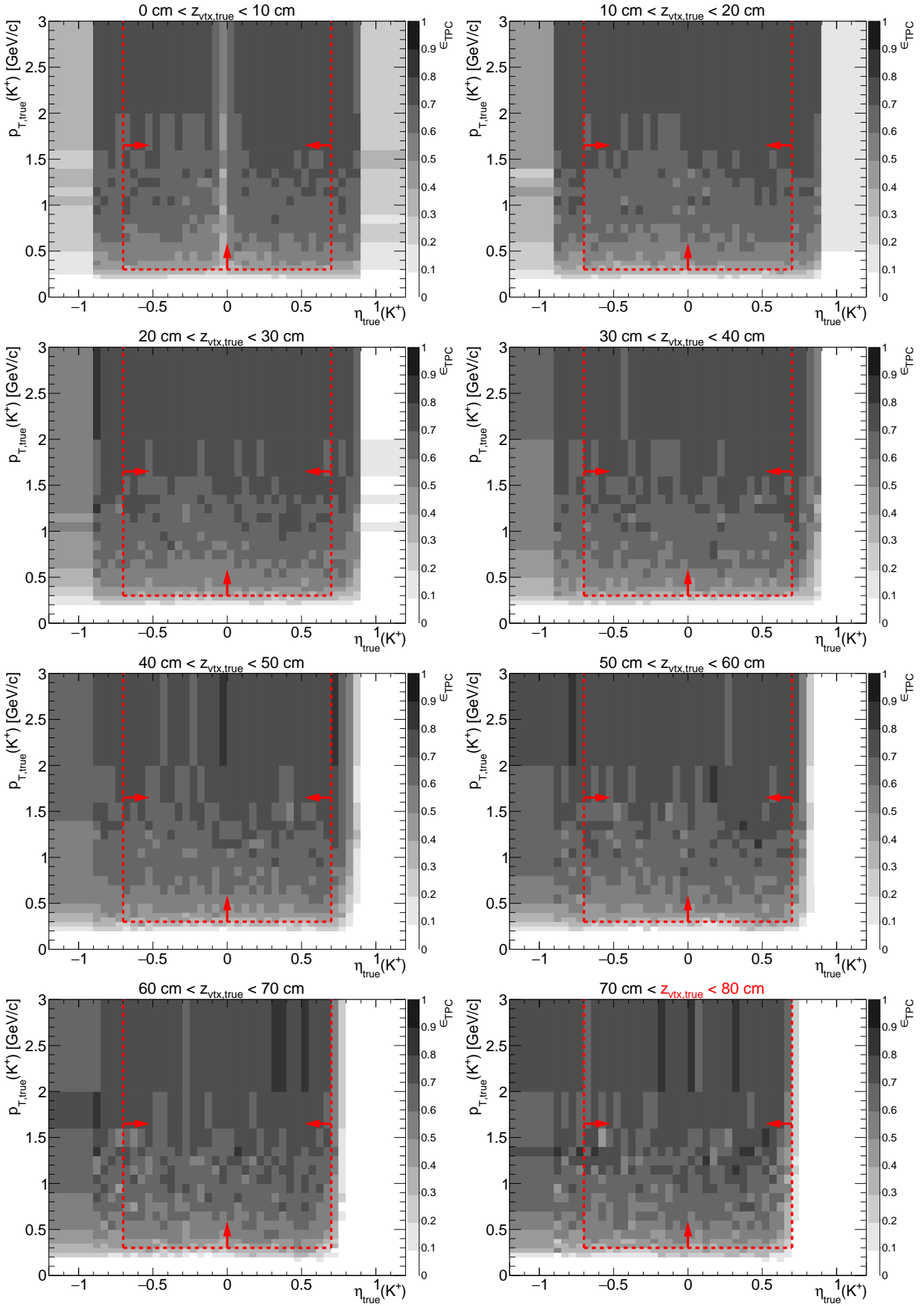
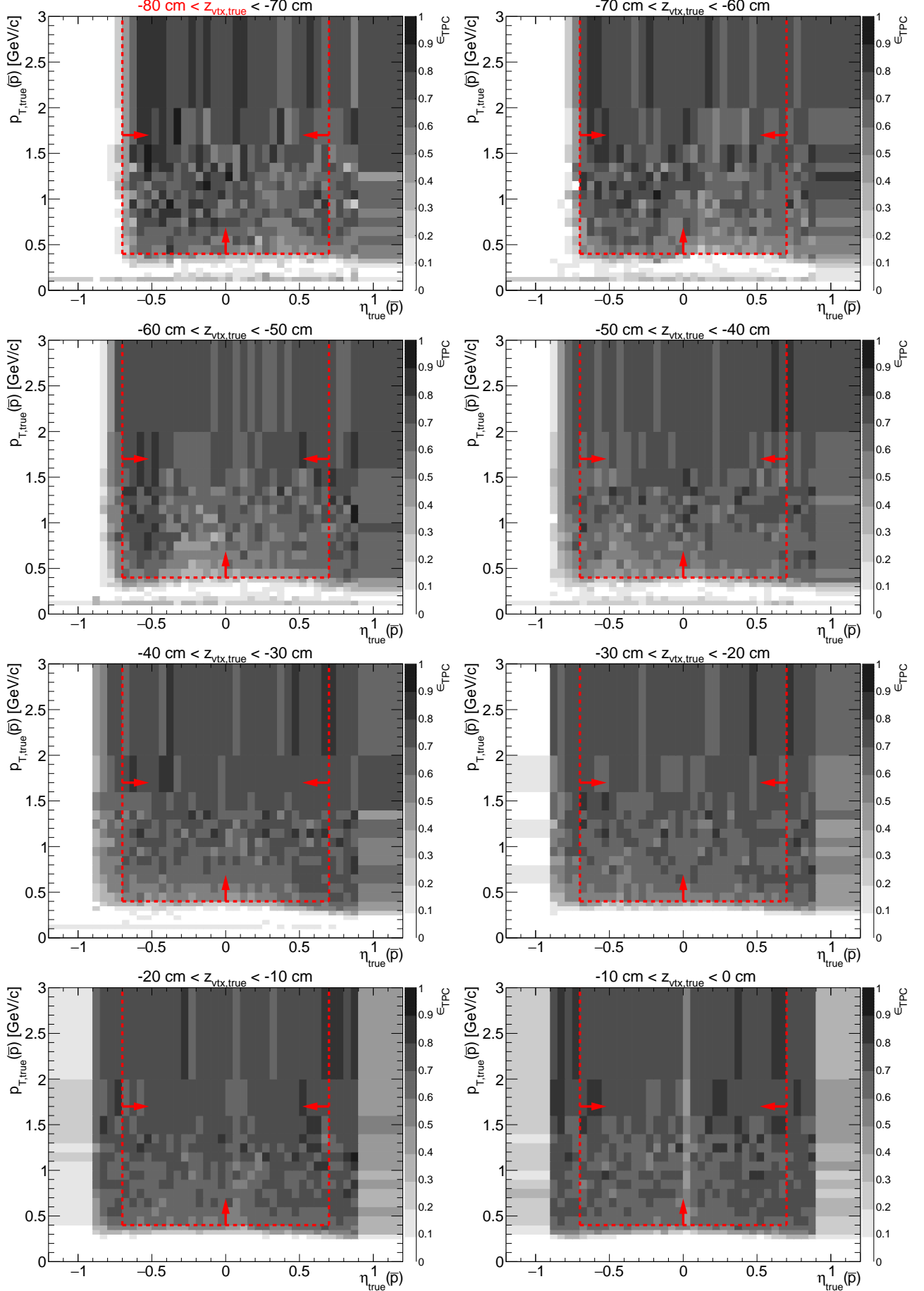


Figure 1.5: TPC acceptance and reconstruction efficiency of \bar{p} . Each plot represents the TPC efficiency ϵ_{TPC} (z -axis) as a function of true particle pseudorapidity η (x -axis) and transverse momentum p_T (y -axis) in single z -vertex bin whose range is given at the top. Red lines and arrows indicate region accepted in analyses.



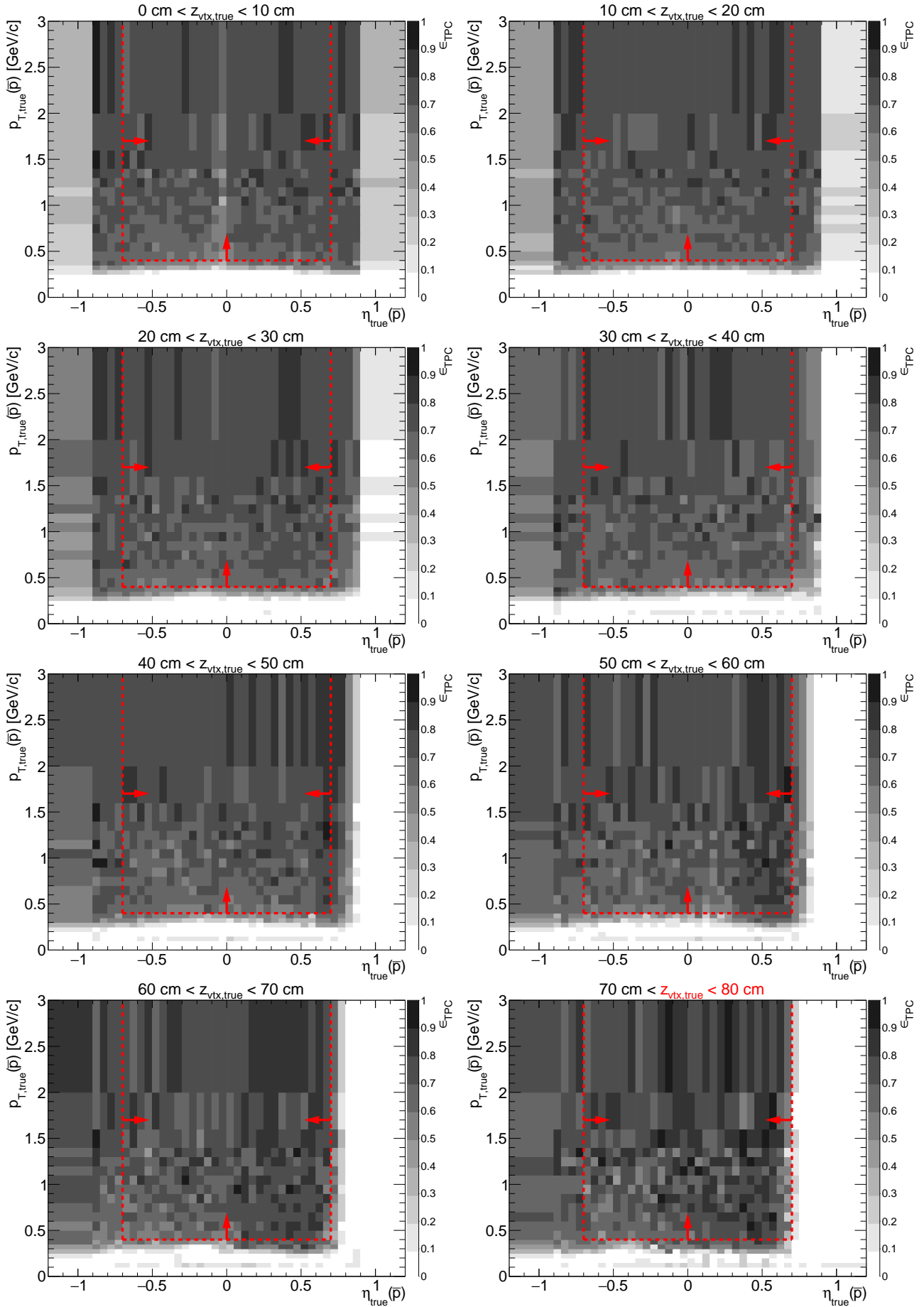
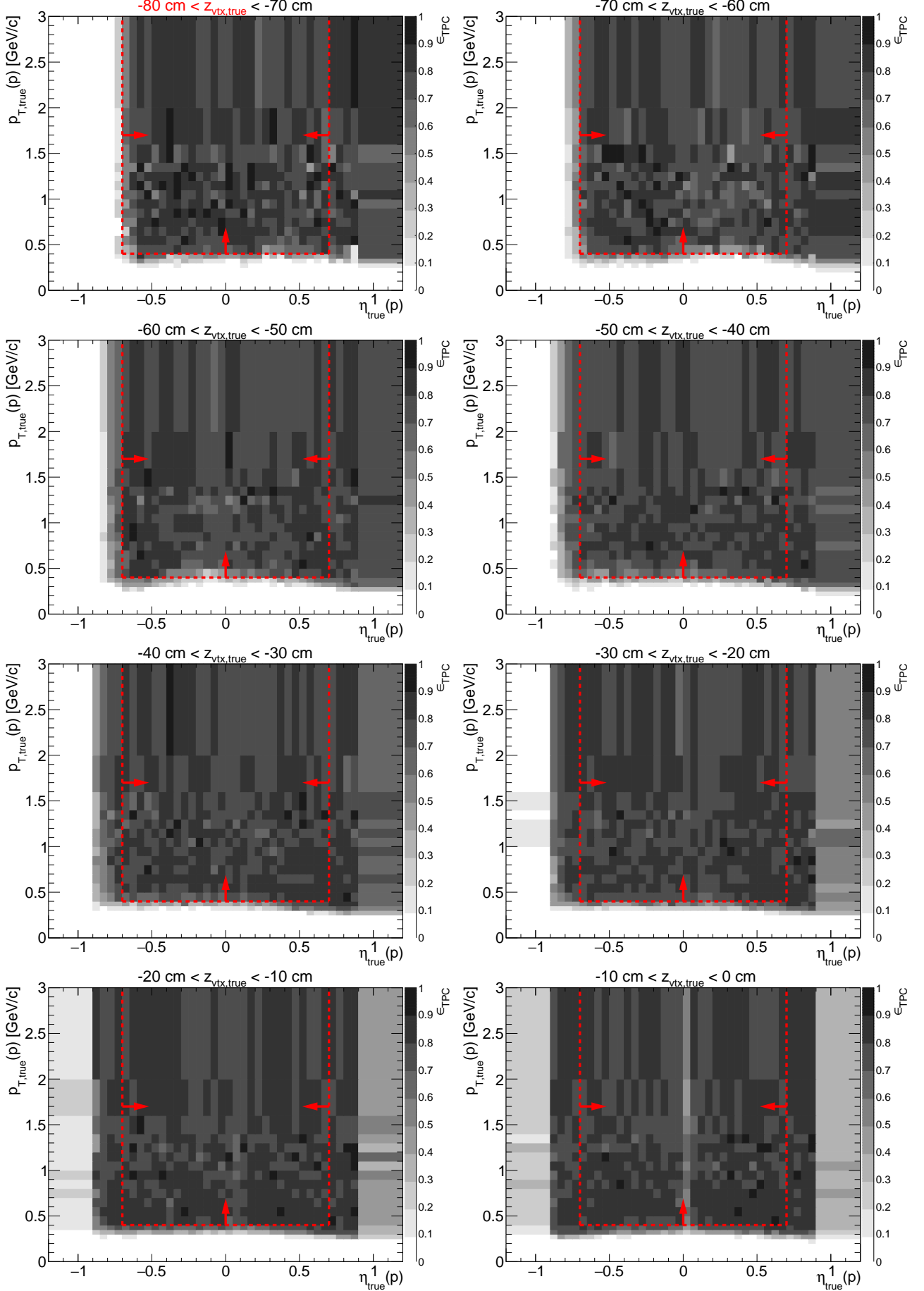
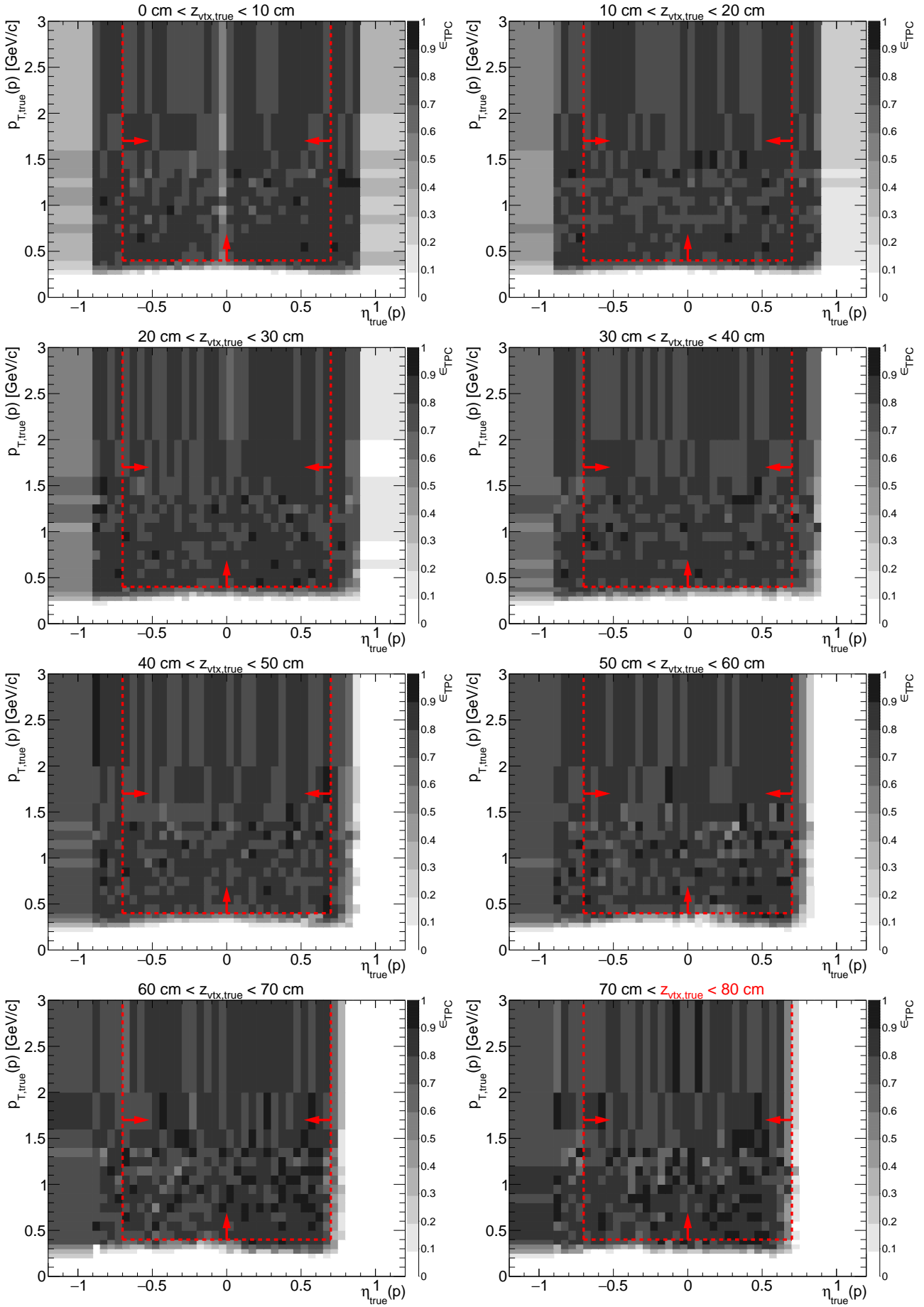


Figure 1.6: TPC acceptance and reconstruction efficiency of p . Each plot represents the TPC efficiency ϵ_{TPC} (z -axis) as a function of true particle pseudorapidity η (x -axis) and transverse momentum p_T (y -axis) in single z -vertex bin whose range is given at the top. Red lines and arrows indicate region accepted in analyses.





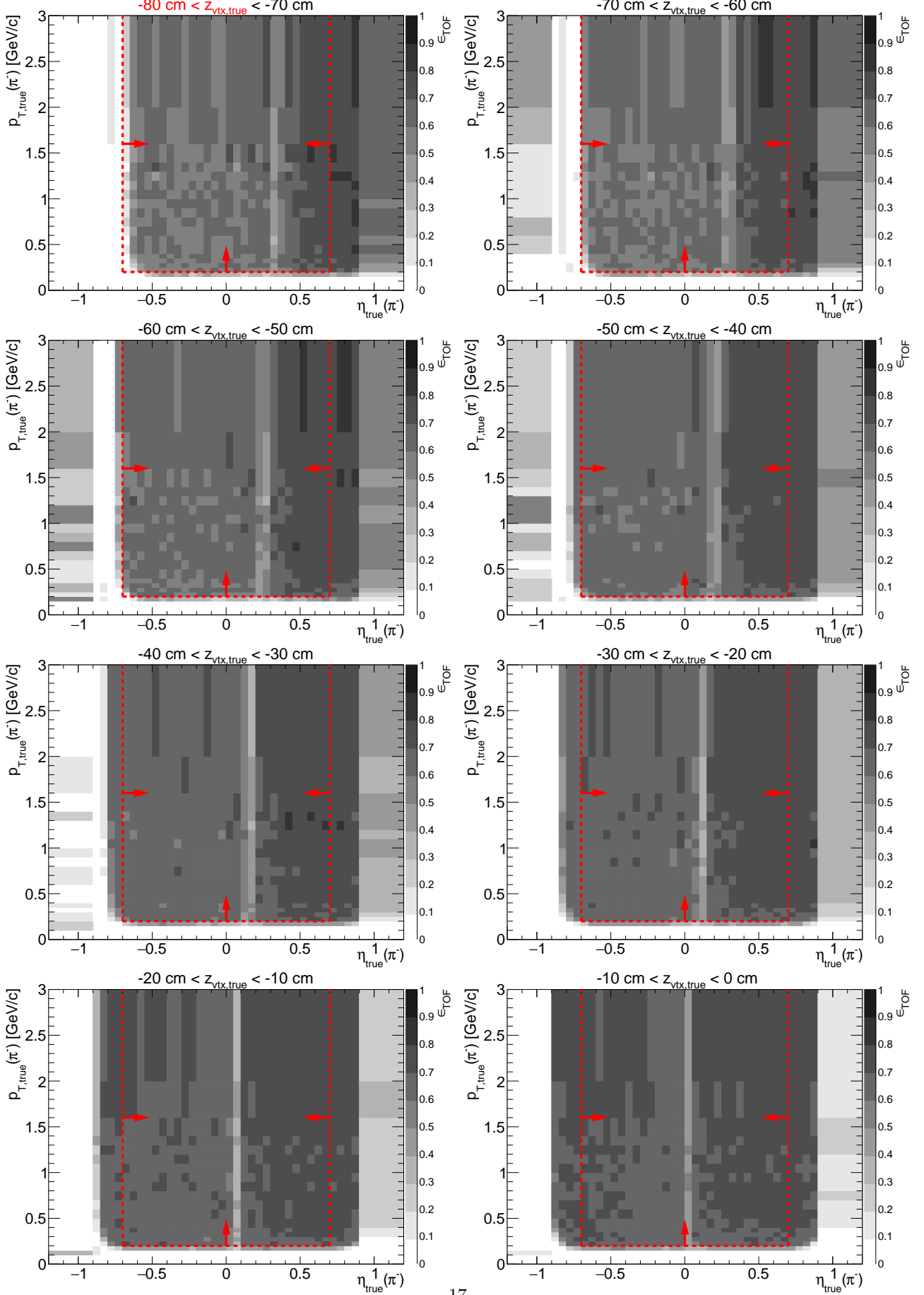
1.2 TOF acceptance, hit reconstruction and track-matching efficiency

Combined TOF acceptance, hit reconstruction efficiency and matching efficiency with TPC tracks, ϵ_{TOF} , is defined as the probability that the global TPC track that satisfy kinematic and quality criteria (cuts ?? and ??) is matched with hit in TOF (matching flag of the track is different from 0). This quantity is generally referred as “TOF efficiency”.

It is calculated in two ways. In the first approach the STARsim MC embedded into zero-bias triggers is used. Tracks belonging to *set B* from Sec. ?? are utilized. From these tracks a sub-sample of tracks with non-zero TOF matching flag is extracted (*set C*). The TOF efficiency is calculated as

$$\epsilon_{\text{TOF}}(p_T, \eta, z_{vx}; \text{sign, PID}) = \frac{(p_T, \eta, z_{vx}) \text{ histogram for particles of given sign and ID from set } C}{(p_T, \eta, z_{vx}) \text{ histogram for particles of given sign and ID from set } B}. \quad (1.2)$$

Figure 1.7: TOF acceptance, reconstruction and matching efficiency of π^- . Each plot represents the TOF efficiency ϵ_{TOF} (z -axis) as a function of true particle pseudorapidity η (x -axis) and transverse momentum p_T (y -axis) in single z -vertex bin whose range is given at the top. Red lines and arrows indicate region accepted in analyses.



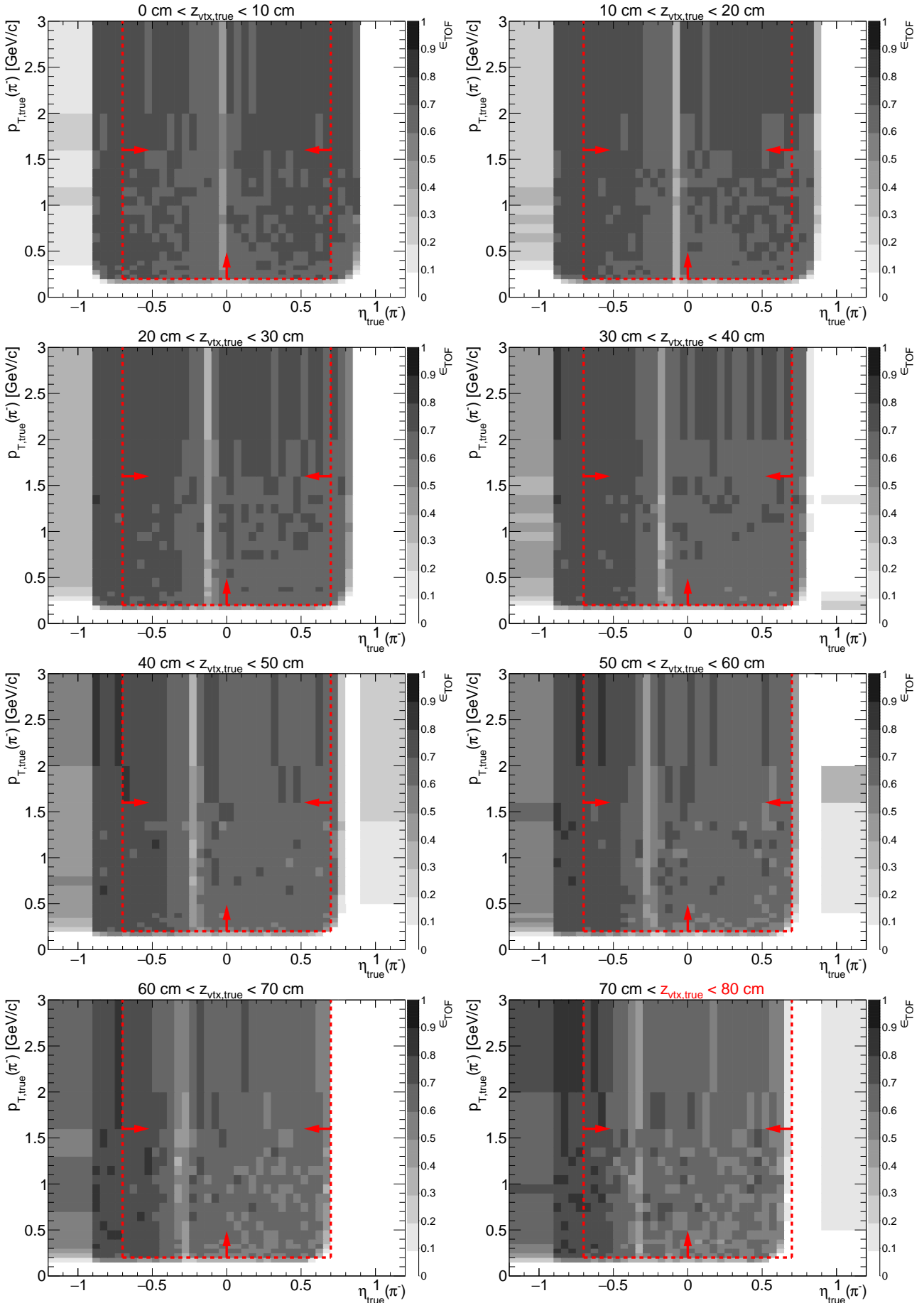
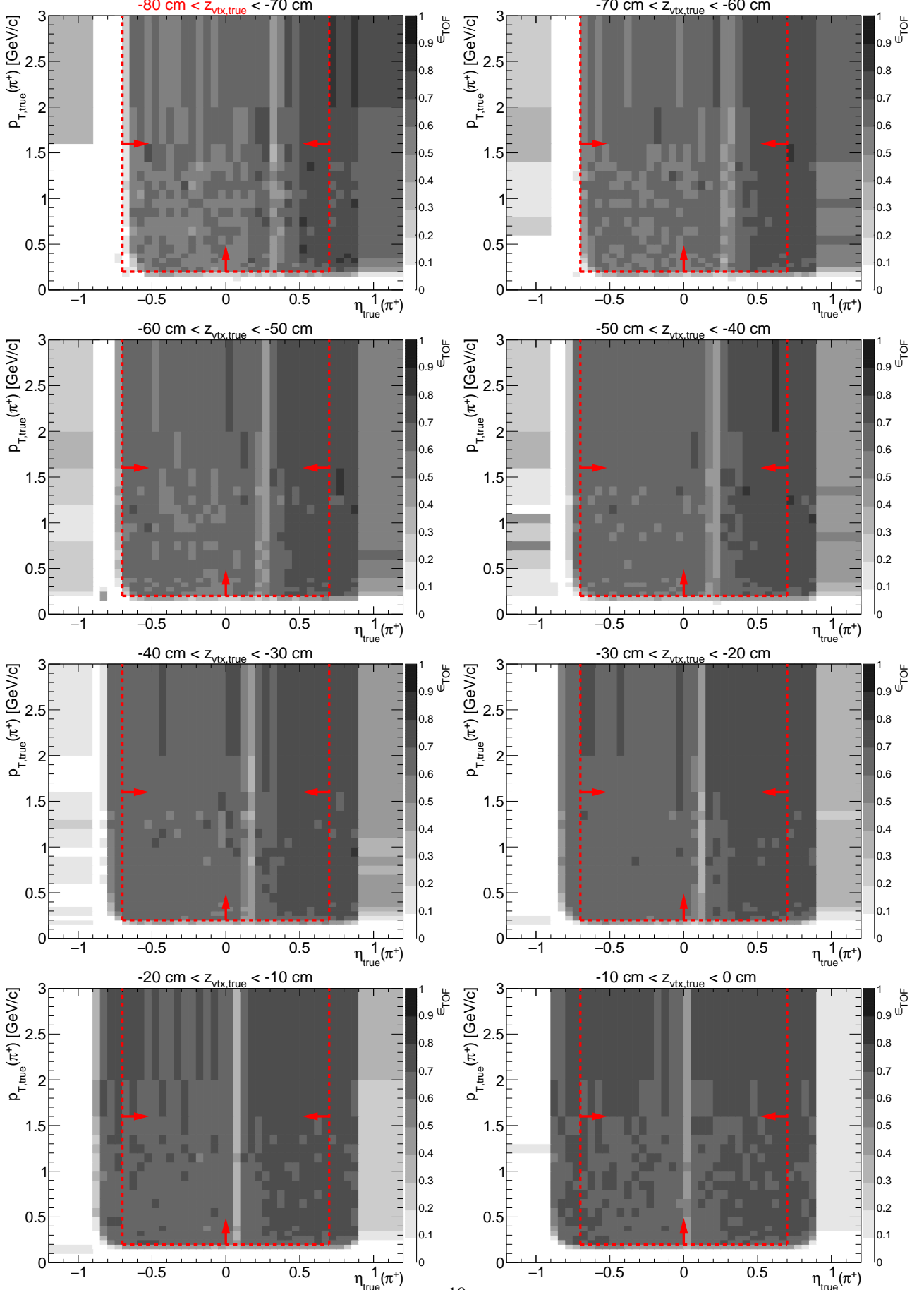


Figure 1.8: TOF acceptance, reconstruction and matching efficiency of π^+ . Each plot represents the TOF efficiency ϵ_{TOF} (z -axis) as a function of true particle pseudorapidity η (x -axis) and transverse momentum p_T (y -axis) in single z -vertex bin whose range is given at the top. Red lines and arrows indicate region accepted in analyses.



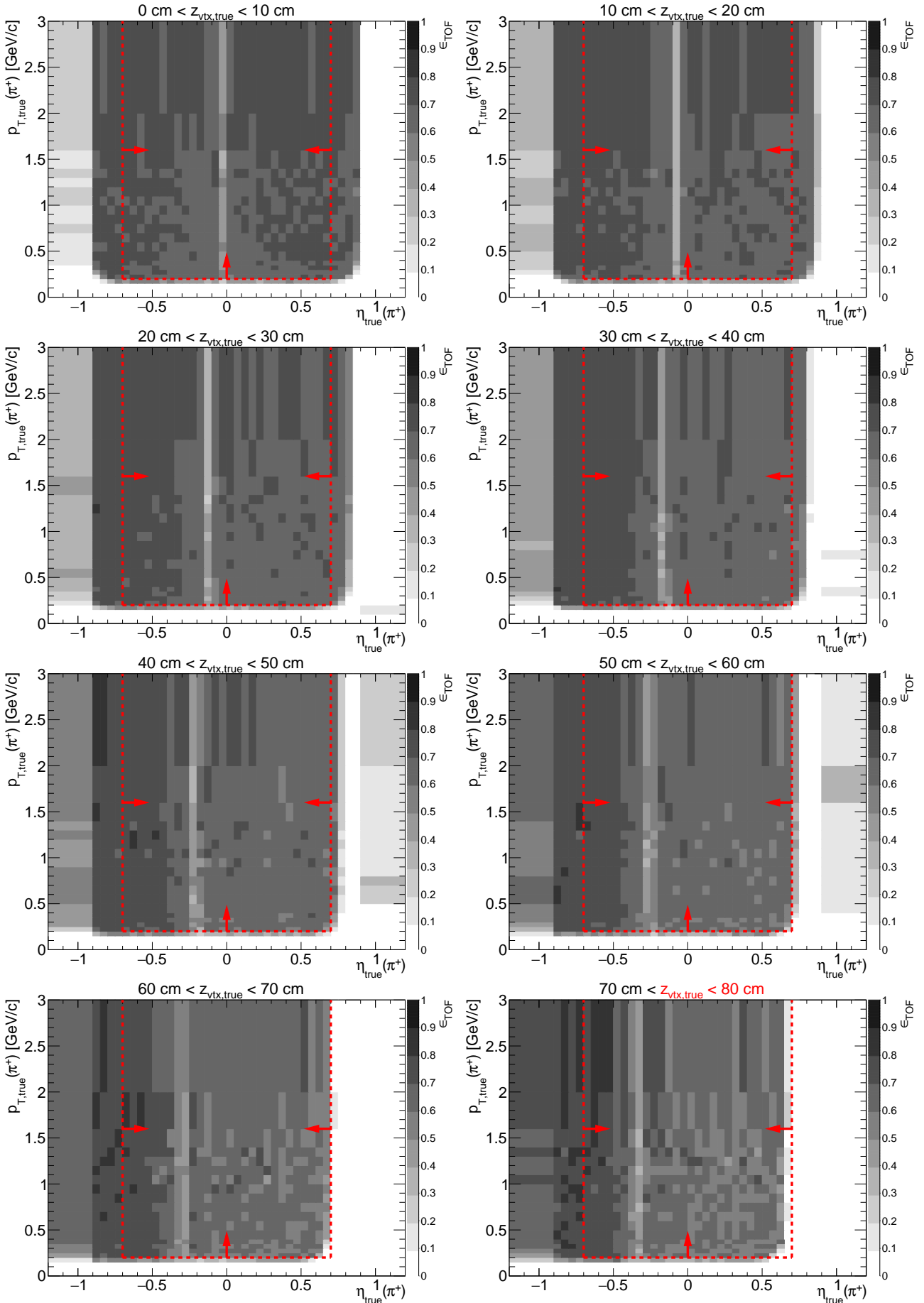
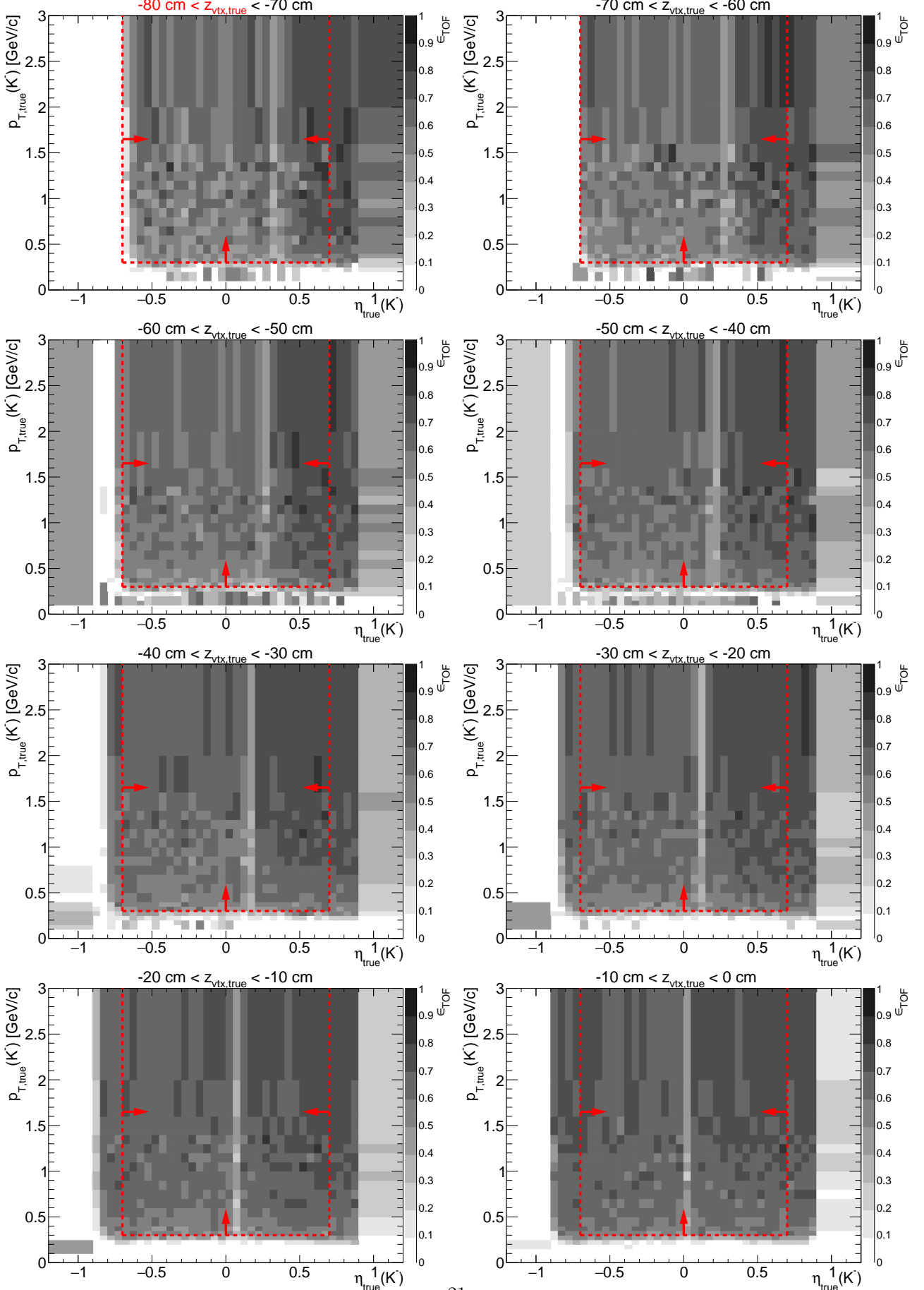


Figure 1.9: TOF acceptance, reconstruction and matching efficiency of K^- . Each plot represents the TOF efficiency ϵ_{TOF} (z -axis) as a function of true particle pseudorapidity η (x -axis) and transverse momentum p_T (y -axis) in single z -vertex bin whose range is given at the top. Red lines and arrows indicate region accepted in analyses.



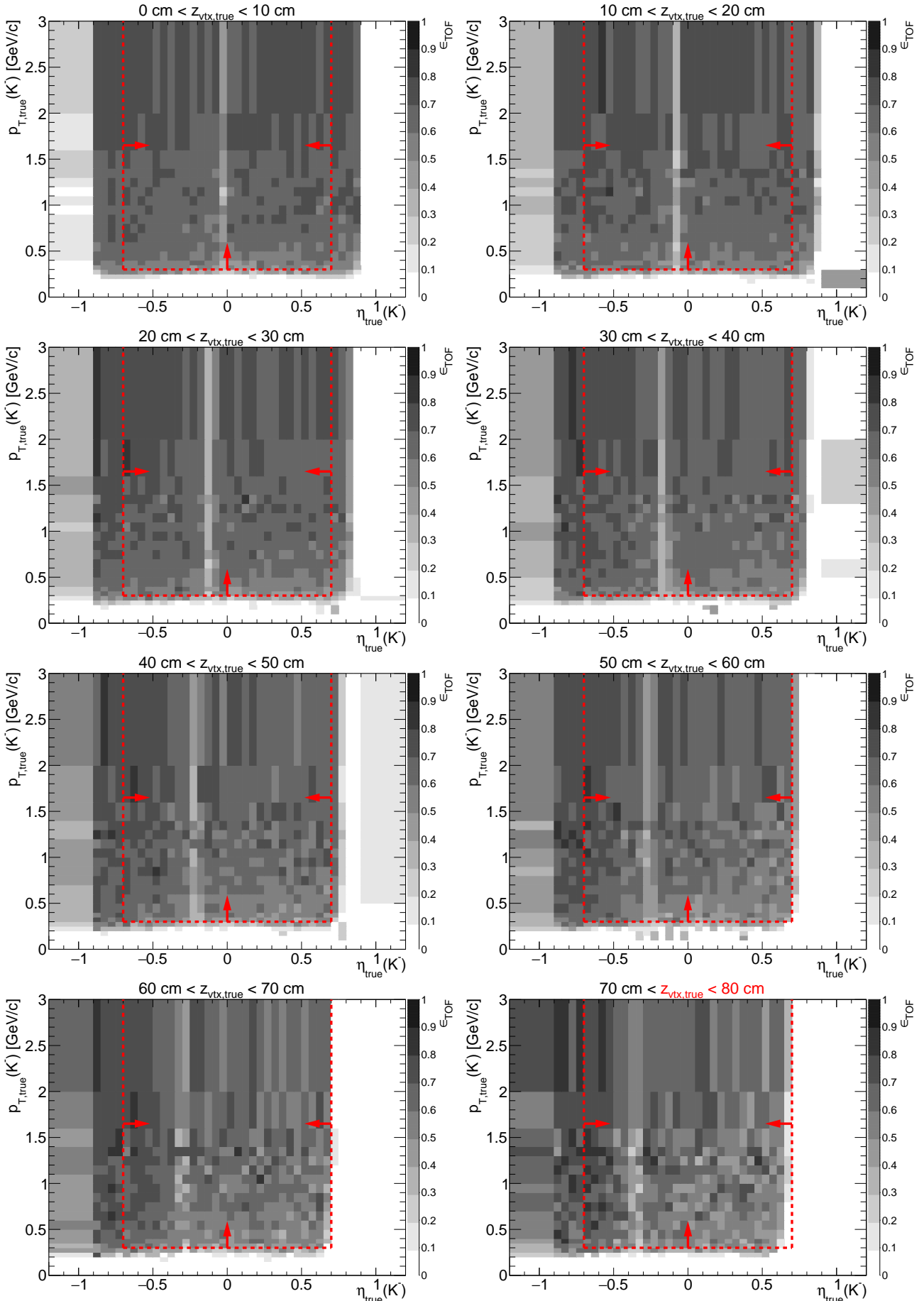
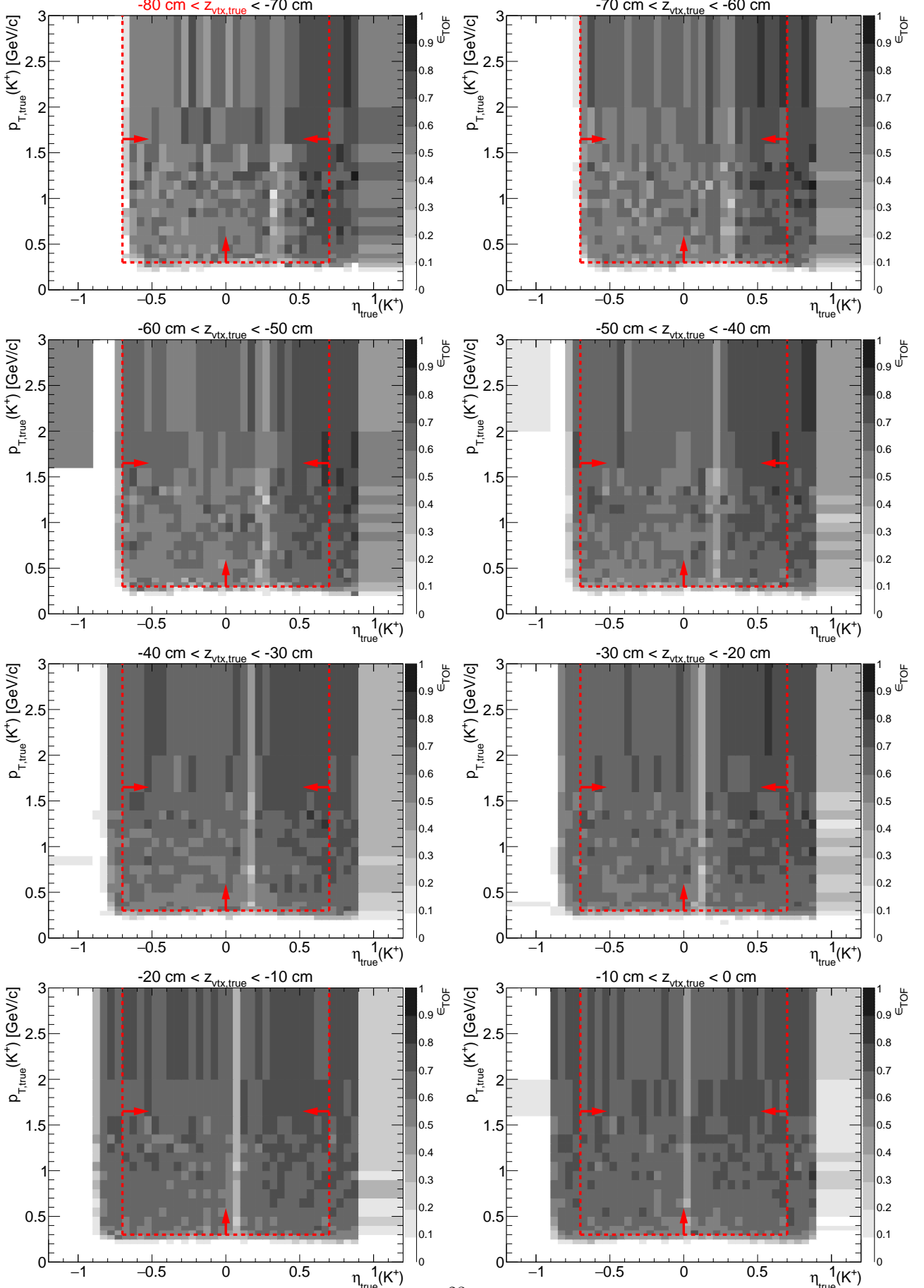


Figure 1.10: TOF acceptance, reconstruction and matching efficiency of K^+ . Each plot represents the TOF efficiency ϵ_{TOF} (z -axis) as a function of true particle pseudorapidity η (x -axis) and transverse momentum p_T (y -axis) in single z -vertex bin whose range is given at the top. Red lines and arrows indicate region accepted in analyses.



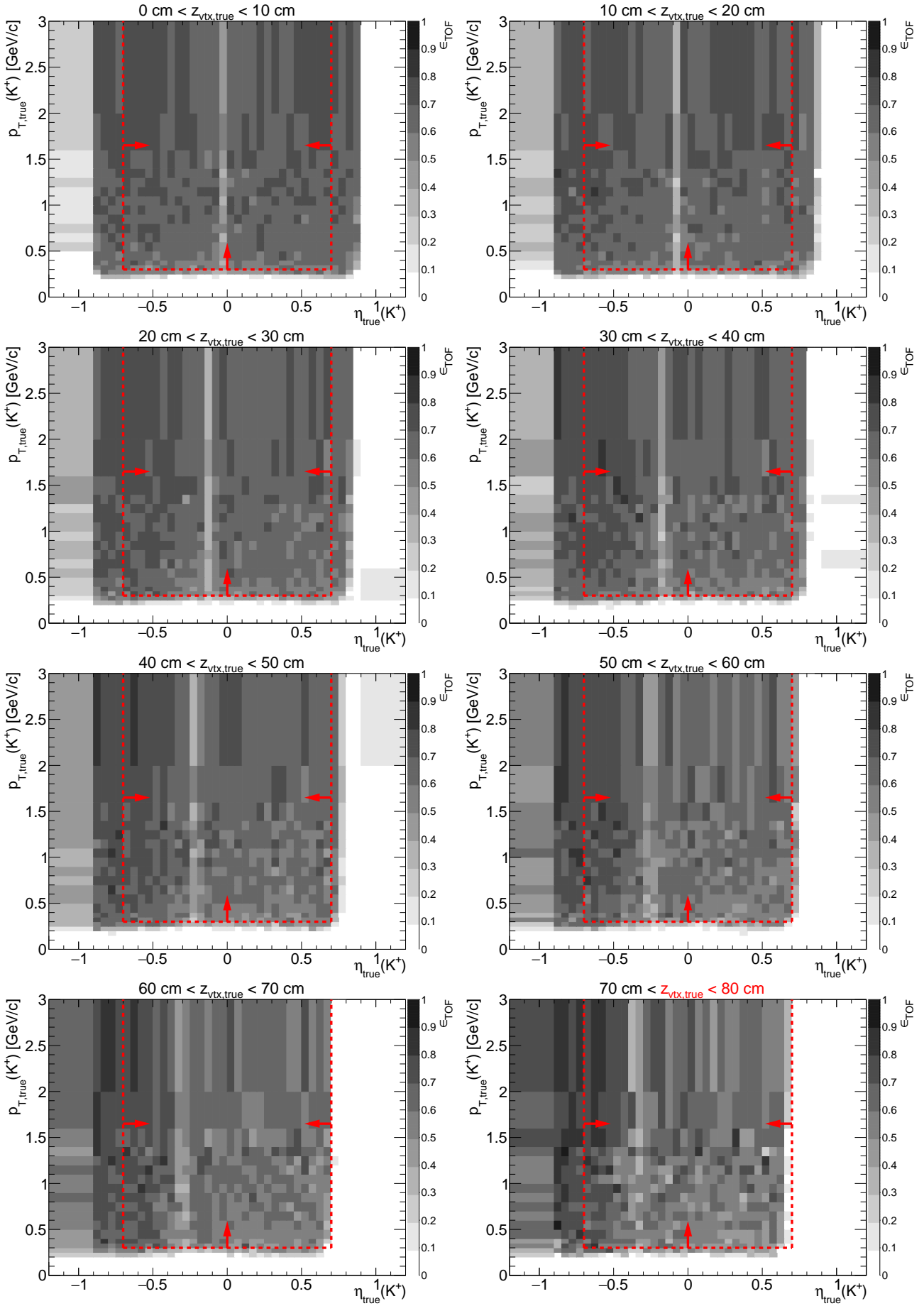
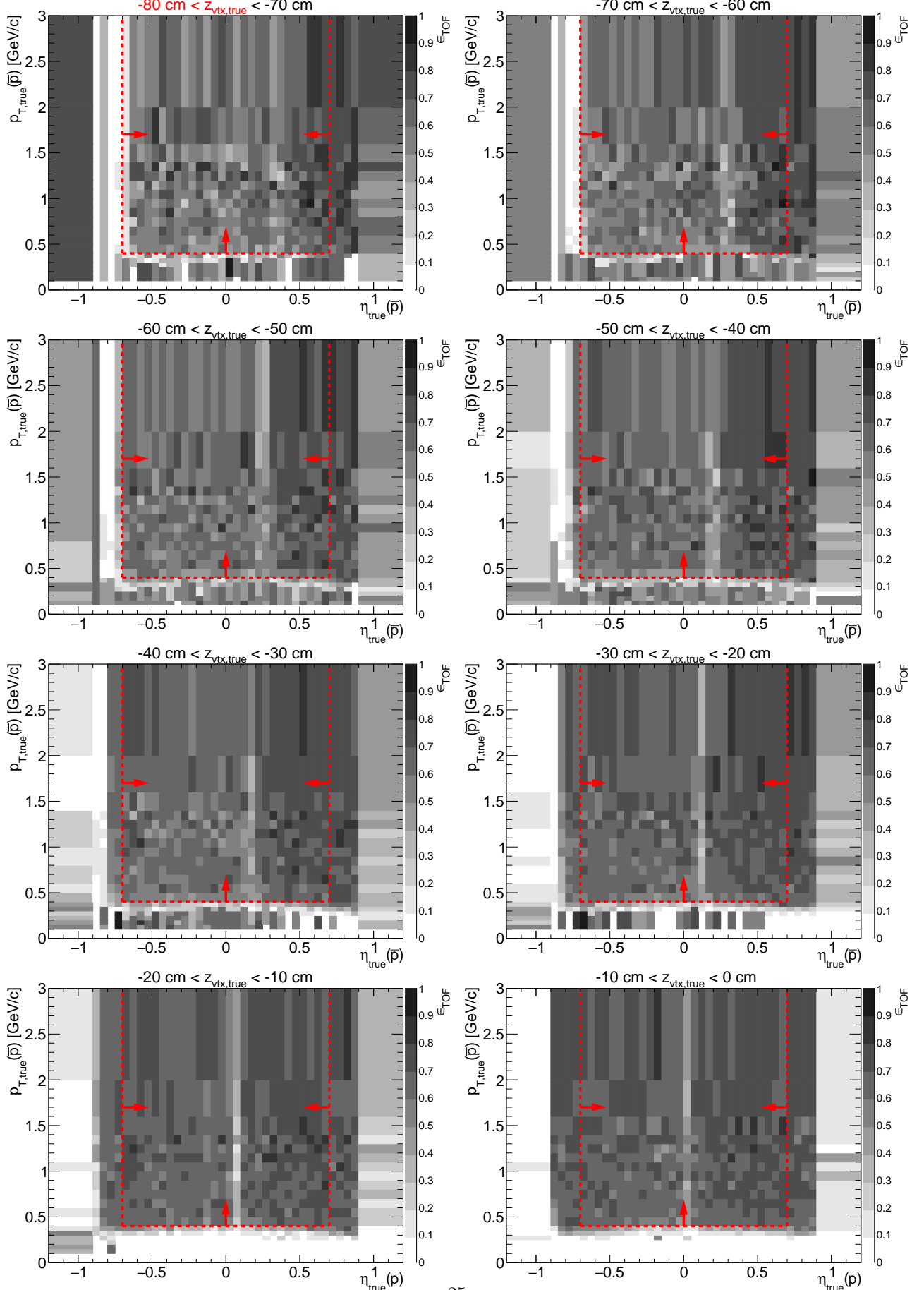


Figure 1.11: TOF acceptance, reconstruction and matching efficiency of \bar{p} . Each plot represents the TOF efficiency ϵ_{TOF} (z -axis) as a function of true particle pseudorapidity η (x -axis) and transverse momentum p_T (y -axis) in single z -vertex bin whose range is given at the top. Red lines and arrows indicate region accepted in analyses.



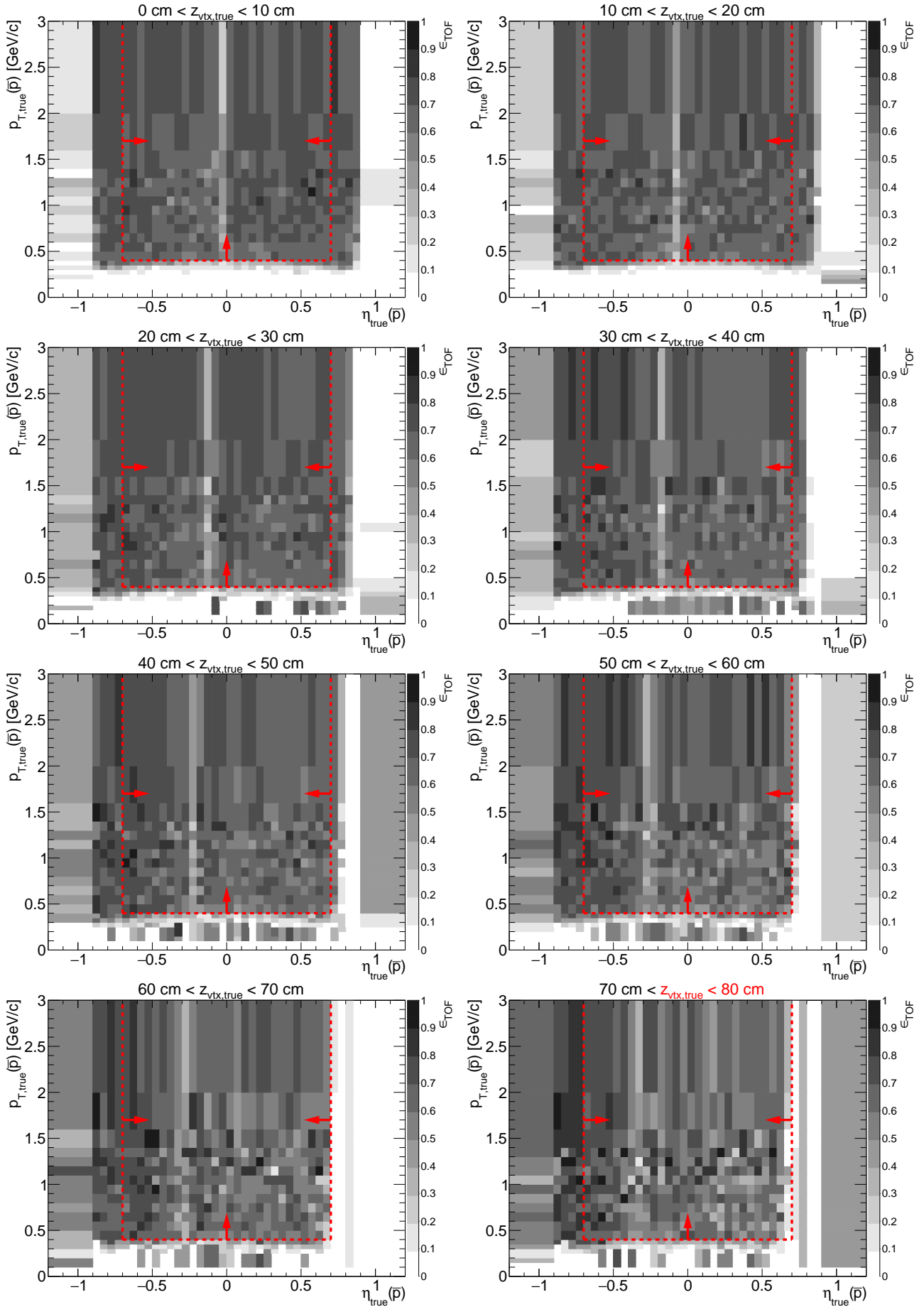
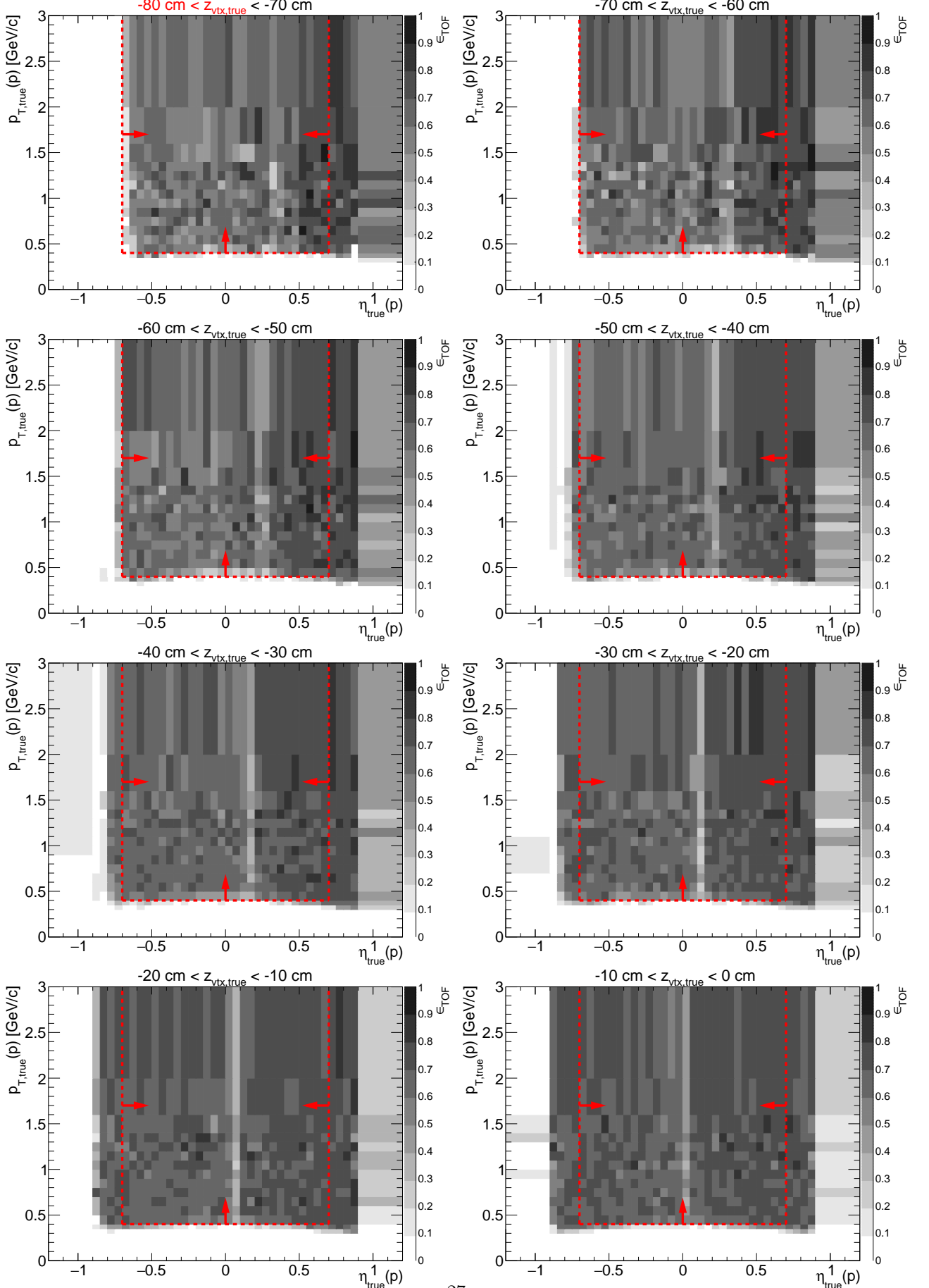
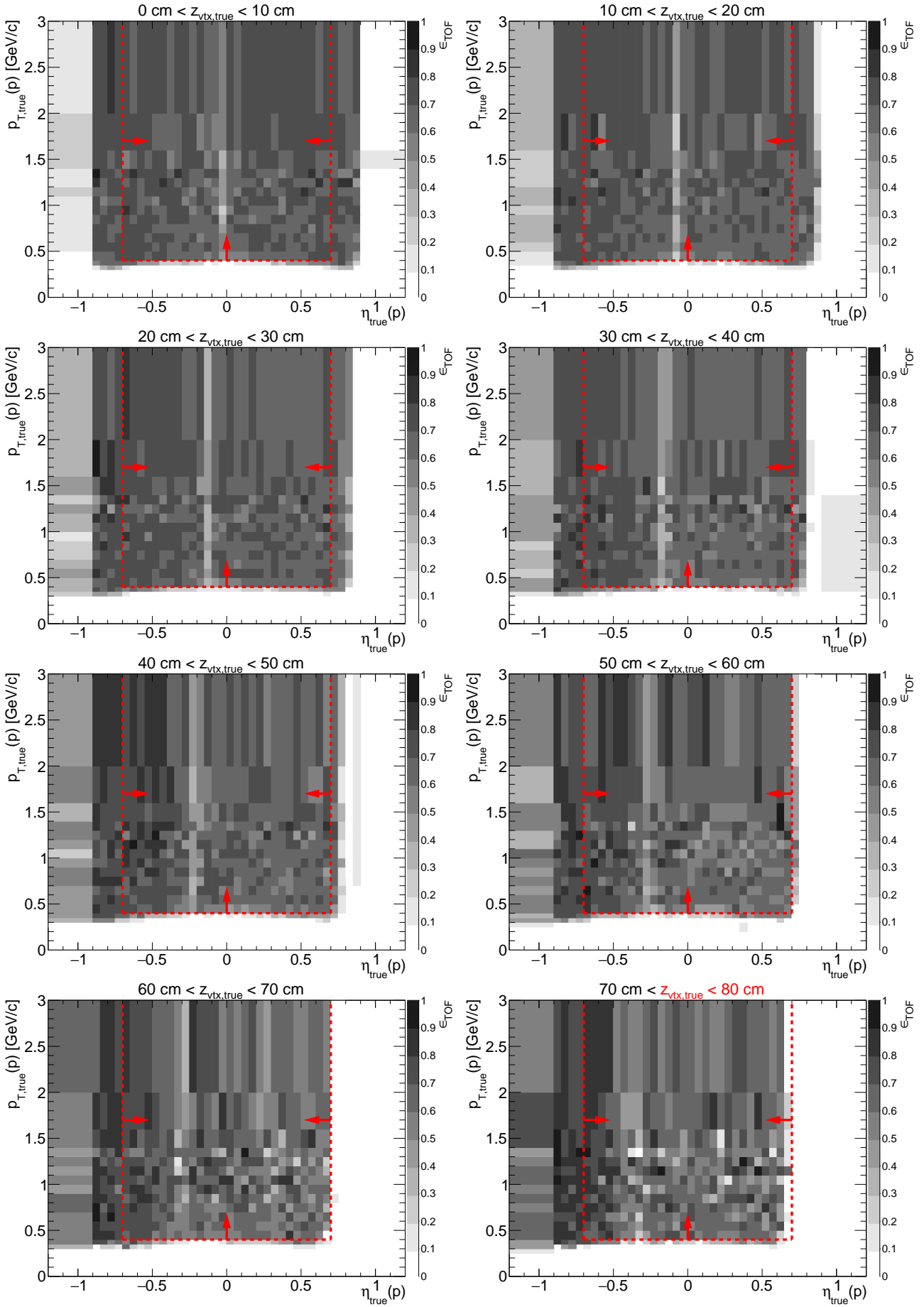


Figure 1.12: TOF acceptance, reconstruction and matching efficiency of p . Each plot represents the TOF efficiency ϵ_{TOF} (z -axis) as a function of true particle pseudorapidity η (x -axis) and transverse momentum p_T (y -axis) in single z -vertex bin whose range is given at the top. Red lines and arrows indicate region accepted in analyses.





1.3 TPC vertex reconstruction efficiency

The definition of vertex reconstruction efficiency established in this analysis is the probability that two global tracks, both associated with true-level primary particles from the kinematic region of the measurement, both satisfying kinematic and quality criteria (cuts ?? and ??) and both matched with hits in TOF, form a vertex listed in the collection of reconstructed primary vertices and DCA(R) and DCA(z) of both global tracks calculated w.r.t. this vertex is contained within the limits of cut ??.

2. Energy Loss Correction

Particles passing through the detector material loose energy as they travel. The track momentum is reconstructed by fitting a helical path to the track points left in the detector. For this procedure all particles are assumed to be pions and the reconstructed momentum is corrected by the amount of energy loss for a pion. Fitting the track points to an ideal helical track tends to underestimate the momentum due to these energy loss effects. For kaons and protons (or anything that is not a pion) the amount of energy loss can be determined from simulated tracks run through GEANT.

3. Roman Pot simulation

4. dE/dx correction

It is possible to transform dE/dx in MC to make it follow the shape of dE/dx in the data. We know that $nSigmaX$ (where X=Pion, Kaon, Proton, ...) variable follows a gaussian distribution (for particle X)

$$nSigmaX = \left(\ln \frac{dE/dx}{\langle dE/dx \rangle_X} \right) / \sigma_{dE/dx}, \quad f(nSigmaX) = \mathcal{N}(nSigmaX; \mu = 0, \sigma = 1)$$

therefore dE/dx itself follows log-normal distribution:

$$f(dE/dx) = \mathcal{L}og\mathcal{N}(dE/dx; \mu = \langle dE/dx \rangle, \sigma = \sigma_{dE/dx}) = \frac{1}{\sqrt{2\pi} \cdot \sigma \cdot dE/dx} e^{-\frac{\ln^2 \frac{dE/dx}{\langle dE/dx \rangle}}{2\sigma^2}}$$

The transformation we want to apply should preserve the shape of dE/dx (so that it is still described by $\mathcal{L}og\mathcal{N}$), however it should change μ and σ so that these values are equal to those seen in the data. The transformation that satisfies above postulate is

$$dE/dx' = c \cdot (dE/dx)^a$$

Parameters of the distribution $\mathcal{L}og\mathcal{N}(dE/dx')$ would be then

$$\mu' = c \cdot \mu^a, \quad \sigma' = a \cdot \sigma$$

From above we get formulae for parameters of the transformation:

$$a = \sigma'/\sigma, \quad c = \frac{\mu'}{\mu^a}$$

AlternativeToCrystallBall [3] Eq. (4.1)

$$f(dE/dx) = \begin{cases} \frac{A}{\sqrt{2\pi} \cdot \sigma \cdot dE/dx} \exp \left(-\frac{1}{2} \left(\frac{\ln \frac{dE/dx}{\langle dE/dx \rangle}}{\sigma} \right)^2 \right) & \text{for } \frac{\ln \frac{dE/dx}{\langle dE/dx \rangle}}{\sigma} \leq k \\ \frac{A}{\sqrt{2\pi} \cdot \sigma \cdot dE/dx} \exp \left(-k \cdot \frac{\ln \frac{dE/dx}{\langle dE/dx \rangle}}{\sigma} + \frac{1}{2} k^2 - k^{-1} \left(\frac{\ln \frac{dE/dx}{\langle dE/dx \rangle}}{\sigma/k} - 1 \right)^k \right) & \text{for } \frac{\ln \frac{dE/dx}{\langle dE/dx \rangle}}{\sigma} > k \end{cases} \quad (4.1)$$

$$g(p) = P_1 + P_2 \cdot \exp(-P_3 \cdot p) + P_4 \cdot \arctan(P_5 \cdot (p - P_6)) \quad (4.2)$$

PID	$\langle dE/dx \rangle_{\text{Bichsel}} - \langle dE/dx \rangle_{\text{MC}}$						$\sigma(dE/dx)_{\text{MC}}$					
	P_1	P_2	P_3	P_4	P_5	P_6	P_1	P_2	P_3	P_4	P_5	P_6
π^\pm	3.618e-8	5.838e-9	5.481				0.0809	-0.023	0.450	-7.84e-3	1.8489	1.04
K^\pm	-1.01e-10	-9.983e-6	7.581				0.0628	0.022	5.381	3.06e-3	7.3070	0.547
p, \bar{p}	-4.041e-8	-1.179e-5	4.277				0.0660	0.082	12.042	1.07e-3	7.2872	0.889
e^\pm	-1.542e-7	3.393e-7	5.025				0.0572	0.982	37.984	2.61e-3	-27.995	0.693
d, \bar{d}	-2.469e-6	0.3706	21.654	5.131e-7	30.050	0.781	0.1311	-0.971	4.691			

(a)

PID	$\langle dE/dx \rangle_{\text{Bichsel}} - \langle dE/dx \rangle_{\text{Data}}$						$\sigma(dE/dx)_{\text{Data}}$					
	P_1	P_2	P_3	P_4	P_5	P_6	P_1	P_2	P_3	P_4	P_5	P_6
π^\pm	-1.236e-8	1.777e-7	9.938				0.0738	16.86	39.44	-1.704e-3	6.482	0.628
K^\pm	5.49e-10	-2.732e-6	7.712				0.0743	2.67e-5	7.17089			
p, \bar{p}	-2.140e-7	0.0421	48.305	7.512e-8	15.544	0.575	0.0779	1.822	22.4277			
e^\pm	6.701e-8	3.304e-7	7.845				0.0678	468.9	59.4001			
d, \bar{d}	-1.631e-7	0.0818	18.91				0.1259	-0.288	3.28733			

(b)

Table 4.1: Parameters of functions from Fig. 4.2 describing track dE/dx as a function of reconstructed momentum for a few particle species. Units of parameters P_i are such that if one provides momentum in Eq. (4.2) in GeV/c the resultant offset of dE/dx MPV with respect to Bichsel parametrization is in GeV/cm , and the resultant σ parameter is unitless.

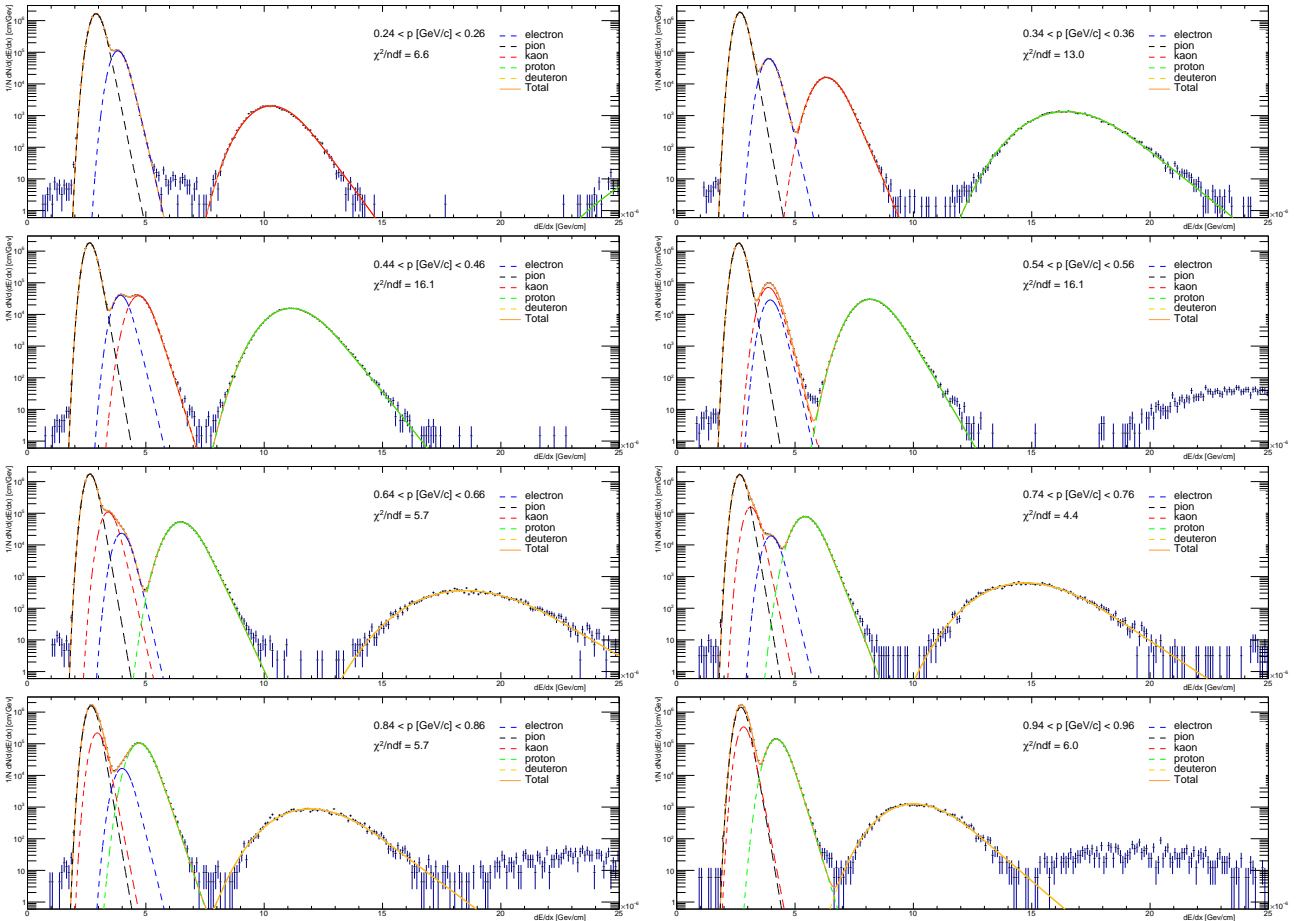


Figure 4.1: Fits of sum of functions from Eq. (4.1) corresponding to different particle species to dE/dx spectra from the data in a few momentum bins.

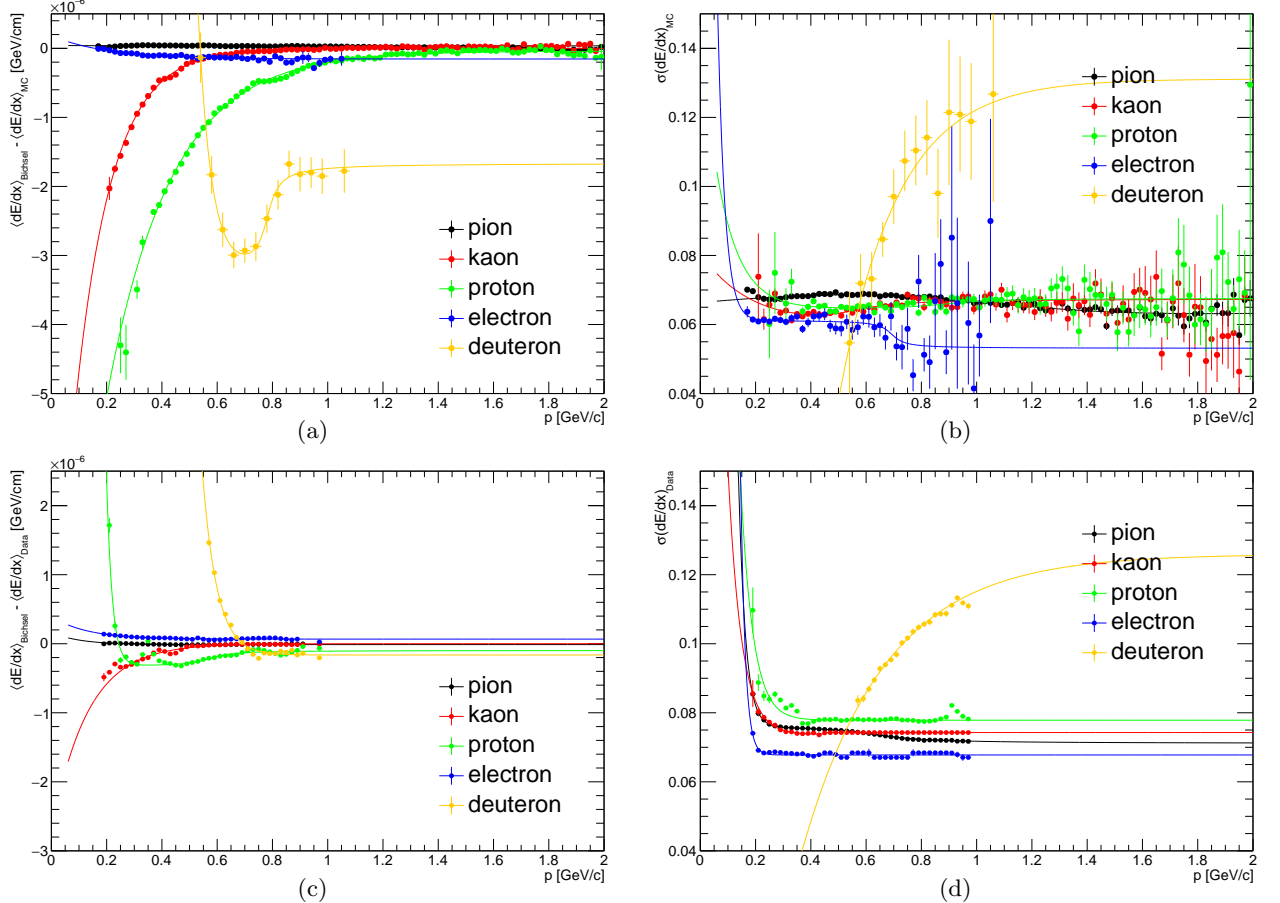


Figure 4.2: Difference between MPV of dE/dx predicted by Bichsel parametrization and obtained from the fit to Eq. (4.1) to dE/dx distribution in the data (4.2c) and MC sample (4.2a) and dE/dx width parameter in data (4.2d) and MC (4.2b) as a function of reconstructed particle momentum for a few particle species. Solid lines represent fits to points of corresponding color.

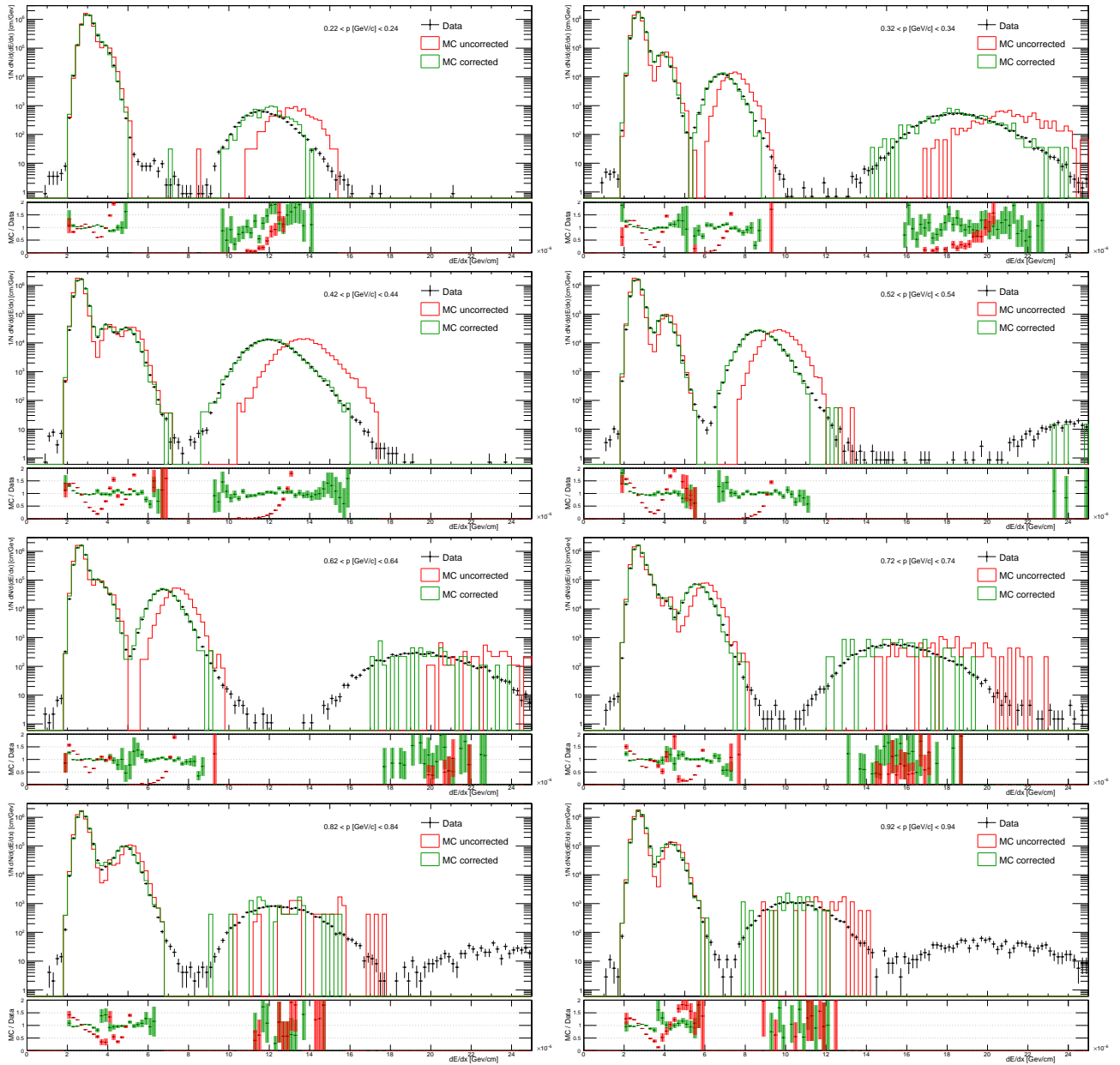


Figure 4.3: Comparison of the dE/dx spectra between the data and MC (before and after correction) in a few momentum bins.

5. TPC track pointing resolution adjustment

It was found during the analysis that distributions of quantities which describe the pointing resolution of the TPC tracks do not agree well between the data and embedded MC. Namely, the resolutions of the global helices associated with the tracks were found to be significantly higher in the STAR simulation than in the data, what manifests as narrower DCA and d_0 distribution in the embedded MC, comparing to corresponding distribution in the data (Fig. 5.5). This issue was discussed under ticket #3332 (Ref. [4]).

This problem could affect the momentum resolution and thus all other resolutions and response matrices used in data unfolding. Therefore the resolution adjustment procedure was performed to find appropriate parameters of the “artificial” helix deterioration and finally obtain agreement between DCA and d_0 distributions (and all related resolutions) in the data and embedded MC.

In order to reduce pointing resolution in the MC an additional smearing of the helix radius $\sigma(R)$ was introduced. Based on d_0 comparison in Fig. 5.5a it was decided to account also for the systematic bias of the helix radius $\Delta\mu(R)$ ¹, which may be present e.g. due to differences in the material budget used the simulation and reconstruction. Both smearing and bias of the helix radius were introduced only for MC tracks which were matched with the true-level particles since only simulated tracks require adjustment (tracks from zero-bias event used in embedding already contain all detector effects).

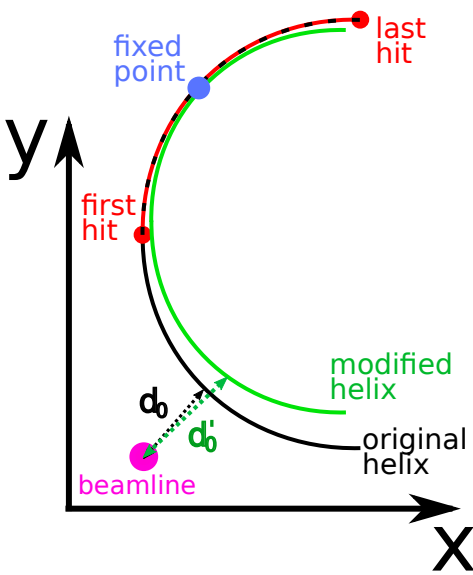


Figure 5.1: Sketch of helix modification procedure and d_0 calculation.

Extraction of $\Delta\mu(R)$ and $\sigma(R)$ parameter required to achieve agreement of pointing resolution between embedded MC and the data involved a few steps, as listed below:

1. Series of d_0 histograms in bins of p_T (100 MeV/c wide) was prepared, each for different size of distortion (different $\Delta\mu(R)$ and $\sigma(R)$) of global helix of the TPC tracks matched with true-level particles (example plot in single p_T bin is shown in Fig. 5.2):
 - (a) for each set of parameters $\Delta\mu(R)$ and $\sigma(R)$ the helix radius R was recalculated independently for each track following the Eq. (5.1):

$$R' = R \times \mathcal{N}(1 + \Delta\mu(R), \sigma(R)), \quad (5.1)$$
 - (b) new helix of a radius R' was assigned to a track and used to calculate d_0 . The modified helix was obtained by changing the radius of original helix from R to R' with a fixed middle point between the first and last TPC hit of a global track represented by the helix (Fig. 5.1). The momentum of the track was also recalculated:

$$p'_T = p_T \times \frac{R'}{R}, \quad \eta' = \eta \times \frac{R'}{R}. \quad (5.2)$$
2. In each p_T bin the χ^2/NDF was calculated between the data and MC d_0 histogram in a range $-1.5 \text{ cm} < d_0 < 1.5 \text{ cm}$ (corresponding to d_0 cut used in analyses), for every point in parameter space of radius distortion (for every set of $\Delta\mu(R)$ and $\sigma(R)$). An example (single p_T bin) of map of $-\chi^2/\text{NDF}$ in a parameter space is presented in Fig 5.3.
3. In each bin of recalculated p_T the 2-dim parabola $z(x, y; a, b, x_0, y_0, z_0)$ given in Eq. (5.3) ($z = \chi^2/\text{NDF}$, $x = \Delta\mu(R)$, $y = \sigma(R)$) was fitted to $-\chi^2/\text{NDF}$ in the global minimum region to obtain the best-fit distortion parameters.

$$z = z_0 - a(x - x_0)^2 - b(y - y_0)^2. \quad (5.3)$$
4. The best-fit smearing $\sigma(R)$ (equal to parabola parameter y_0) and best-fit bias $\Delta\mu(R)$ (x_0) from individual p_T bins was plotted as a function of global track p_T (Fig. 5.4). Each point was assigned with an error being a quadratic sum of two components: the error on x_0 (y_0) resulting from the parabola fit to $-\chi^2/\text{NDF}$, and length of corresponding semi-axis of ellipsis formed by the intersection of fitted parabola with the xy -plane at $z = z_0 - 1/\text{NDF}$ (from definition of the parameter uncertainty given by the change of overall χ^2 by 1 unit). Resultant formulae for the error of each individual point in Fig. 5.4 are

¹Transverse impact parameter d_0 takes positive value if the beamline is contained inside the helix (in the yz -plane projection), otherwise it is negative. Any asymmetry in the d_0 distribution in the MC with respect to the data indicates presence of systematic difference in reconstructed d_0 , hence also in reconstructed R .

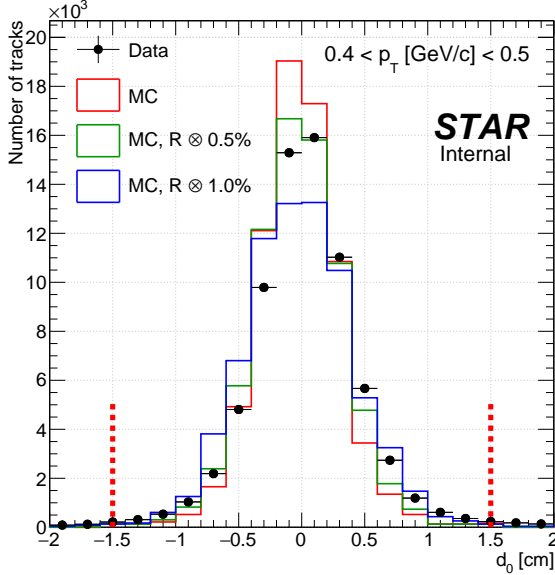


Figure 5.2: Example of comparison of d_0 histograms in single p_T bin in the data (black points) and embedded MC (colored lines) in the procedure of TPC pointing resolution adjustment. MC histograms only for $\Delta\mu(R) = 0$ and $\sigma(R) = 0, 5 \times 10^{-3}$ and 10^{-2} were shown for explanatory purposes.

$$\delta(\Delta\mu(R)) = \sqrt{\delta_{\text{fit}}^2(x_0) + \frac{1}{2a\text{NDF}}}, \quad (5.4)$$

From Fig. 5.2 one can read that $\text{NDF} = 14$. In calculation of uncertainties correlation of $\Delta\mu(R)$ and $\sigma(R)$ have not been accounted.

5. The empirically determined functions were fitted to points representing $\Delta\mu(R)$ and $\sigma(R)$ dependence on the global track p_T . Their form and values of parameters are given in Fig. 5.4.

Helices of global TPC tracks were deteriorated according to Eq. (5.1) and the parametrizations of global track p_T -dependence of $\Delta\mu(R)$ and $\sigma(R)$ from Fig. 5.4, to verify if better agreement between the data and embedded MC is found after the adjustment. Filled histograms in Fig. 5.5 show d_0 and DCA distributions after the described adjustment, and filled circles in the bottom pad show their ratio to the data points. Clearly, there is much better agreement between embedded MC and the data after the pointing resolution adjustment. Remaining differences may arise from incomplete theoretical model of the CEP process implemented in GenEx leading to different p_T spectra of the data and the model (e.g. model does not contain resonant $\pi^+\pi^-$ production).

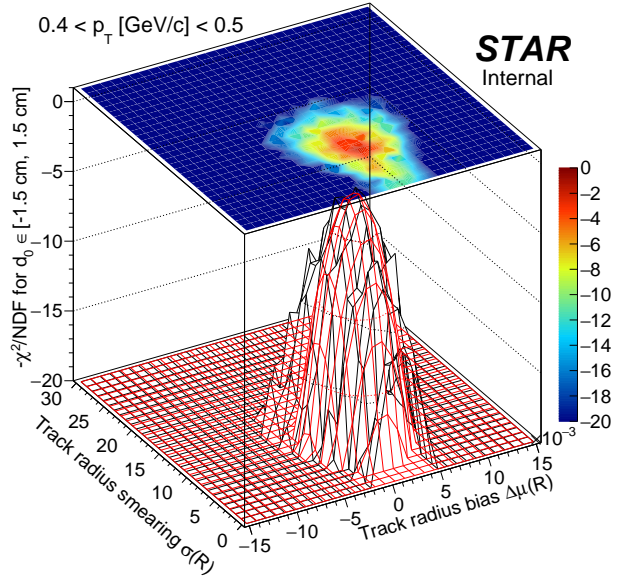


Figure 5.3: Example of $-\chi^2/\text{NDF}$ map in a parameter space in the procedure of TPC pointing resolution adjustment. The red surface represents parabola fitted in the vicinity of the global minimum.

$$\delta(\sigma(R)) = \sqrt{\delta_{\text{fit}}^2(y_0) + \frac{1}{2b\text{NDF}}}. \quad (5.5)$$

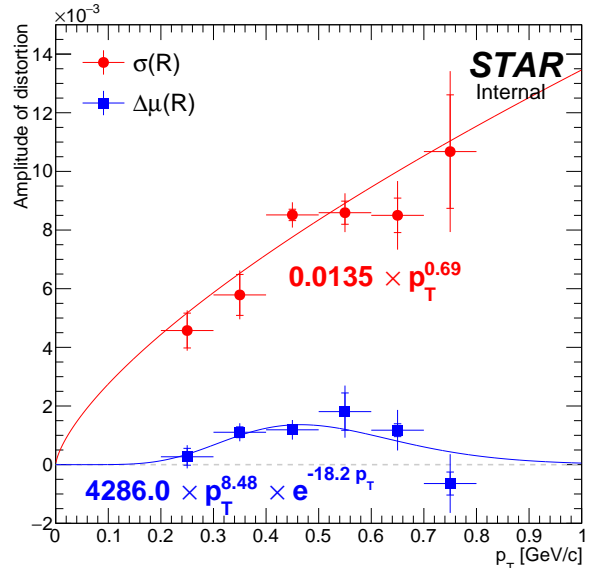
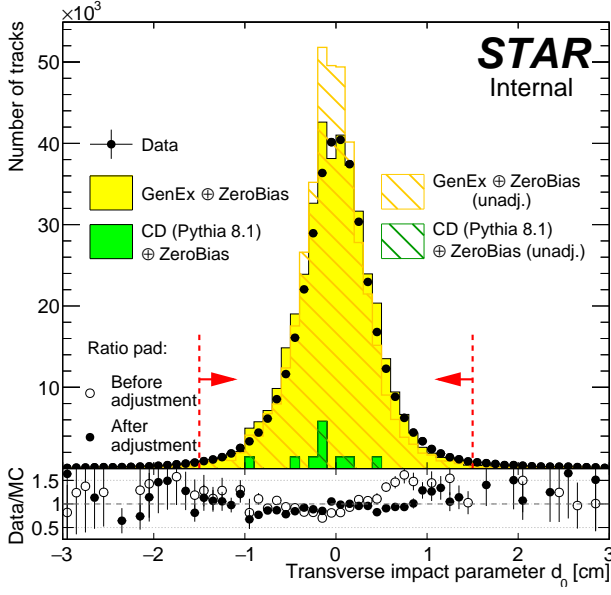
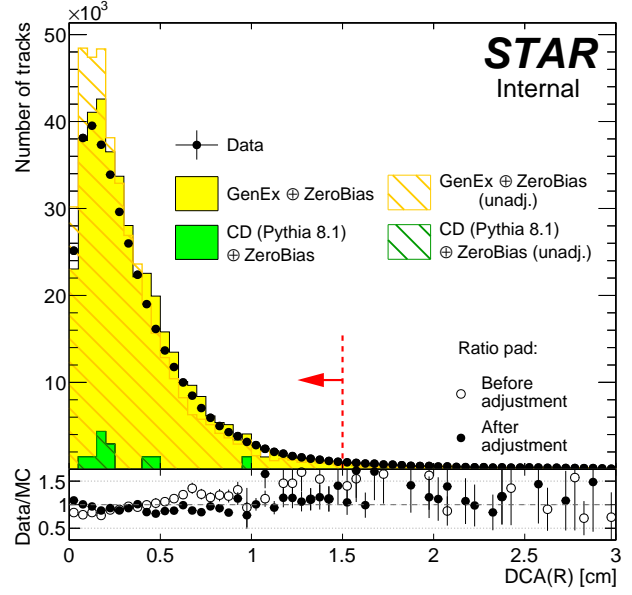


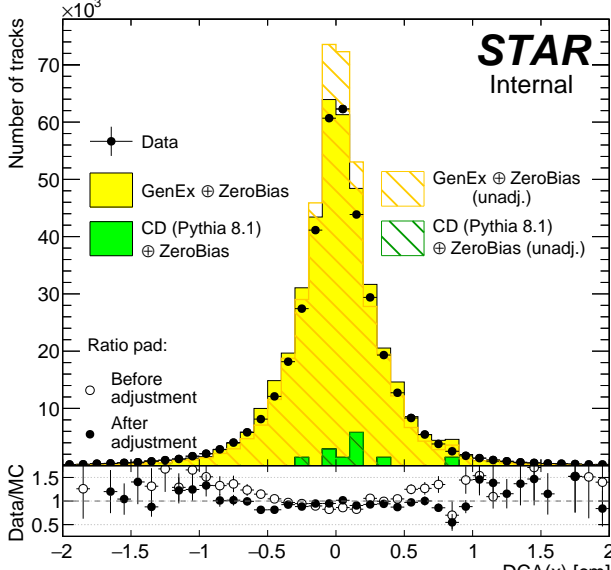
Figure 5.4: Best-fit parameters obtained in the procedure of the TPC track pointing resolution adjustment. Uncertainties on parameters resulting solely from the fit of Eq. (5.3) to $-\chi^2/\text{NDF}$ are represented by the lines with perpendicular endings. Total uncertainties (Eqs. (5.4), (5.5)) extend beyond. The empirical functions fitted to points are drawn with corresponding colors, and formula of each is written aside.



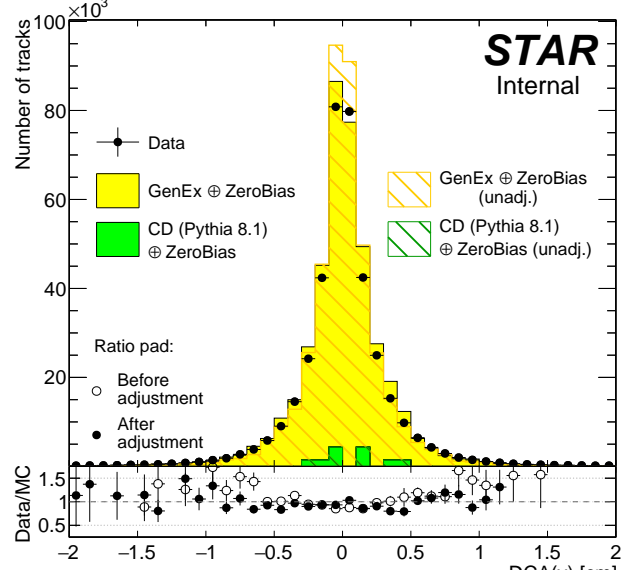
(a)



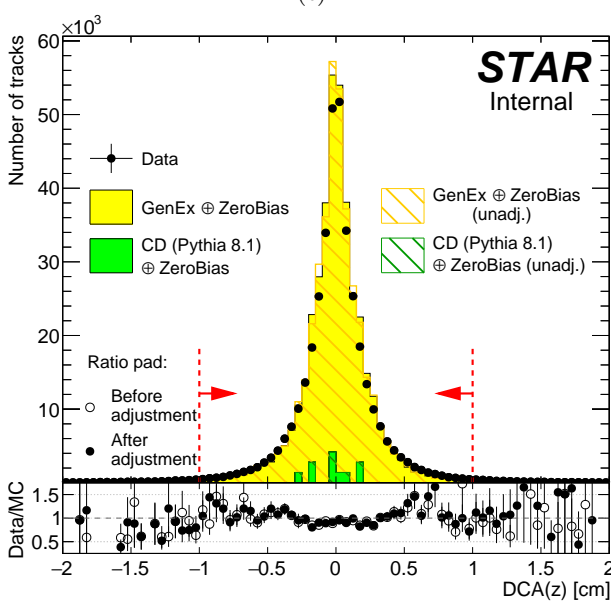
(b)



(c)



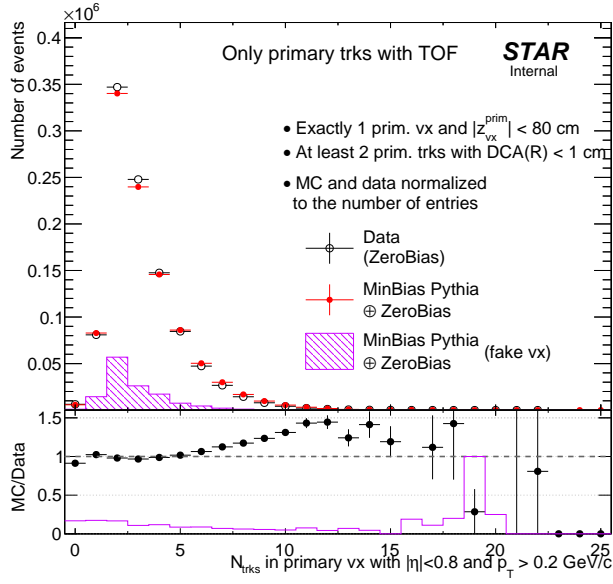
(d)



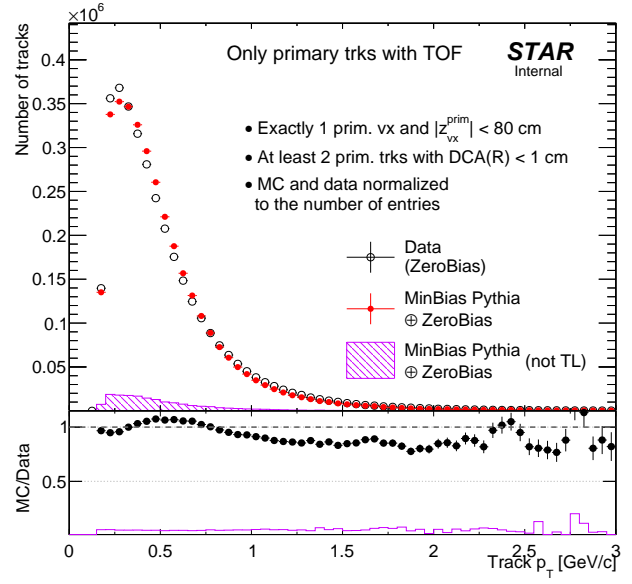
(e)

Figure 5.5: Comparison of distribution of pion transverse impact parameter d_0 (5.5a) and transverse (5.5b), x - (5.5c), y - (5.5d) and z -component (5.5e) of the DCA vector between the global helix and primary vertex in the data (CEP) and embedded MC (GenEx). Distributions for unadjusted helices are drawn as hashed histograms, while filled histograms are for adjusted helices. Normalizations of the signal and backgrounds were established from the comparison of p_T^{miss} and $\Delta\theta$ distributions after full selection (without cut on the presented quantity and without exclusivity cut), as described in Sec. XXX of Ref. [1]. Red dashed lines and red arrows indicate the range of each quantity which is accepted in analyses.

6. Dead material in front of TPC

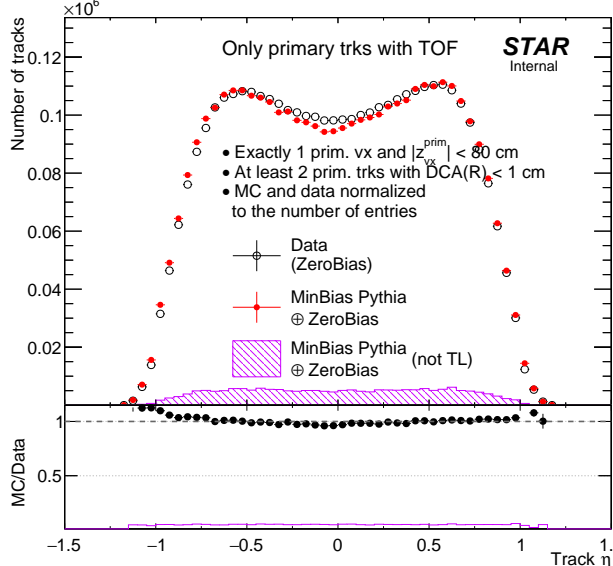


(a)



(b)

Figure 6.1: ...



(c)

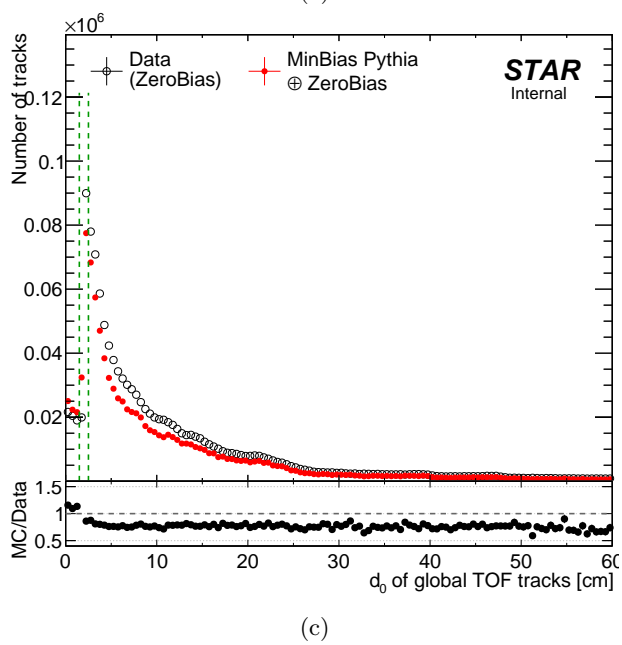
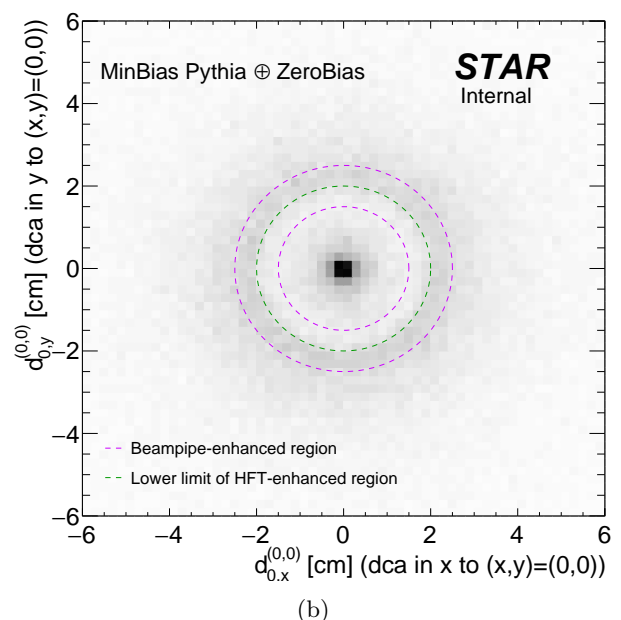
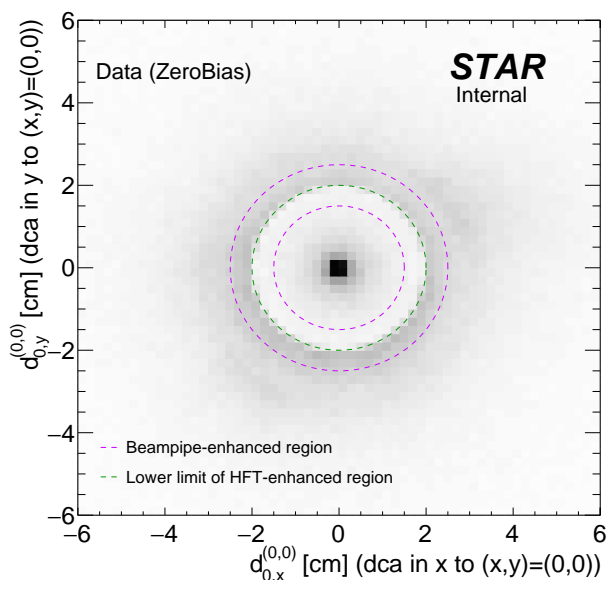


Figure 6.2: ...

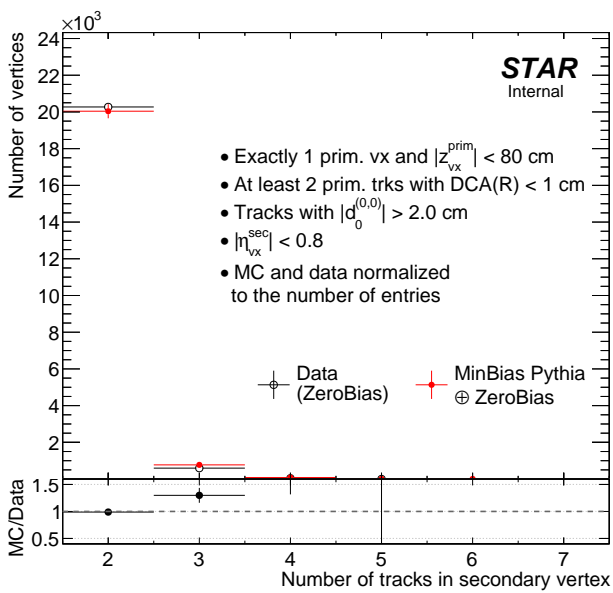


Figure 6.3: ...

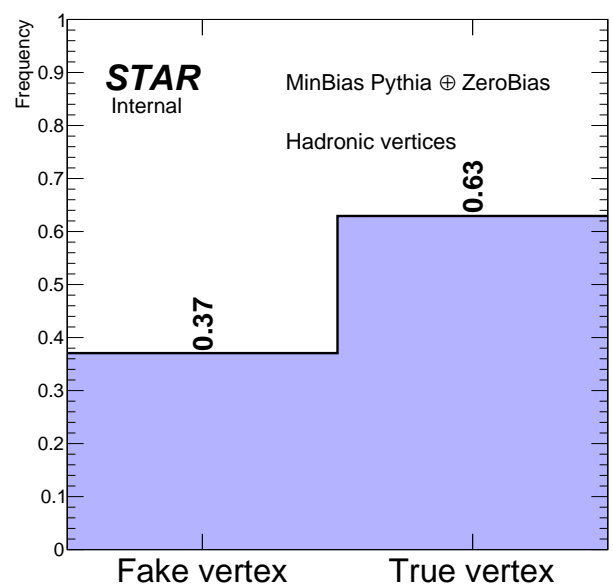


Figure 6.4: ...

7. Systematic errors

7.1 TPC track reconstruction efficiency systematics

One major difference between simulation and real data is the presence of pile-up events. The average number of pile-up tracks in a triggering event is proportional to the BBC coincidence rate. It is expected that the difference between simulation and real data drops at lower BBC rates, and the effects of pile-up tracks could be much reduced by fitting the tracking efficiency as a function of BBC rate and using the extrapolated value at zero luminosity to compare with simulation.

The embedded MC was divided into two samples due to mean BBC_AND rate: $\langle \text{BBC_AND} \rangle = 700 \text{ kHz}$ and $\langle \text{BBC_AND} \rangle = 1400 \text{ kHz}$. Next, the track reconstruction efficiency was calculated for those two samples and no-pile-up MC corresponding to them. The difference between TPC track reconstruction efficiencies for pile-up and no-pile-up MCs was calculated as:

$$\Delta\epsilon_{TPC}^{1400/700 \text{ kHz}} = \frac{N_{reco}^{\text{no-pile-up}} - N_{reco}^{\text{pile-up}}}{N_{gen}} \quad (7.1)$$

where:

N_{gen} -number of MC tracks,

$N_{reco}^{\text{no-pile-up}}$ - number of reconstructed tracks, matched with MC tracks in no-pile-up MC,

$N_{reco}^{\text{pile-up}}$ - number of reconstructed tracks, matched with MC tracks in pile-up MC.

The difference between high and low pile-up runs is given by:

$$\Delta\epsilon_{TPC} = \Delta\epsilon_{TPC}^{1400 \text{ kHz}} - 2 \cdot \Delta\epsilon_{TPC}^{700 \text{ kHz}} \quad (7.2)$$

Finally, above difference, shown in Figs. 7.2 and 7.3 for π^\pm , varies between 2 – 3% and was taken as systematic uncertainty related to TPC track reconstruction efficiency.

Figure 7.2: π^\pm TPC track reconstruction efficiency as a function of p_T ($|\eta| < 0.7$, $|V_z| < 80 \text{ cm}$) for embedded MC samples with $\langle \text{BBC_AND} \rangle = 700 \text{ kHz}$ and $\langle \text{BBC_AND} \rangle = 1400 \text{ kHz}$. The efficiencies from corresponding no-pile-up MC samples were also shown. Additionally, the differences from Eq. 7.2 were drawn in the bottom of each plot.

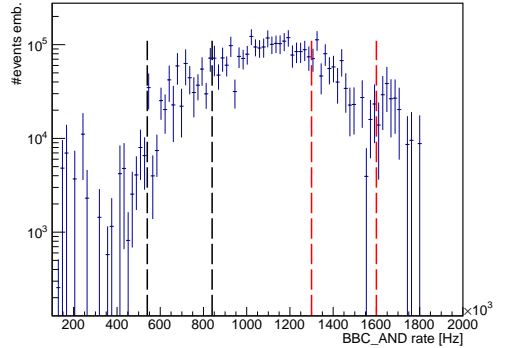
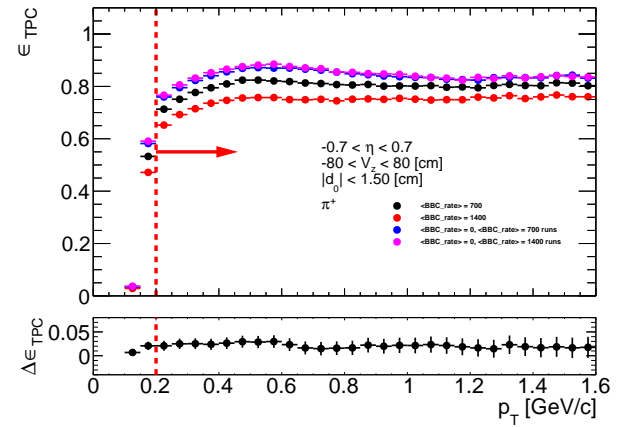
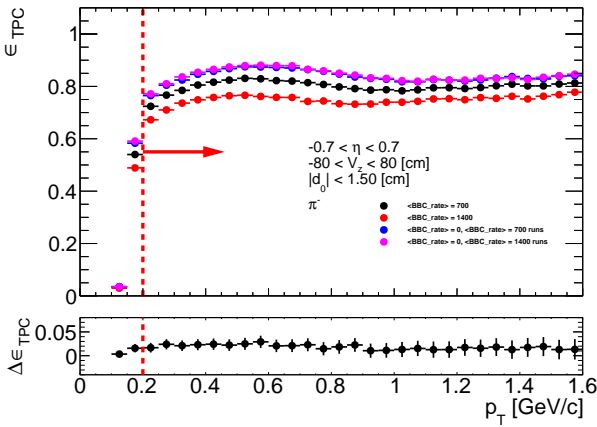
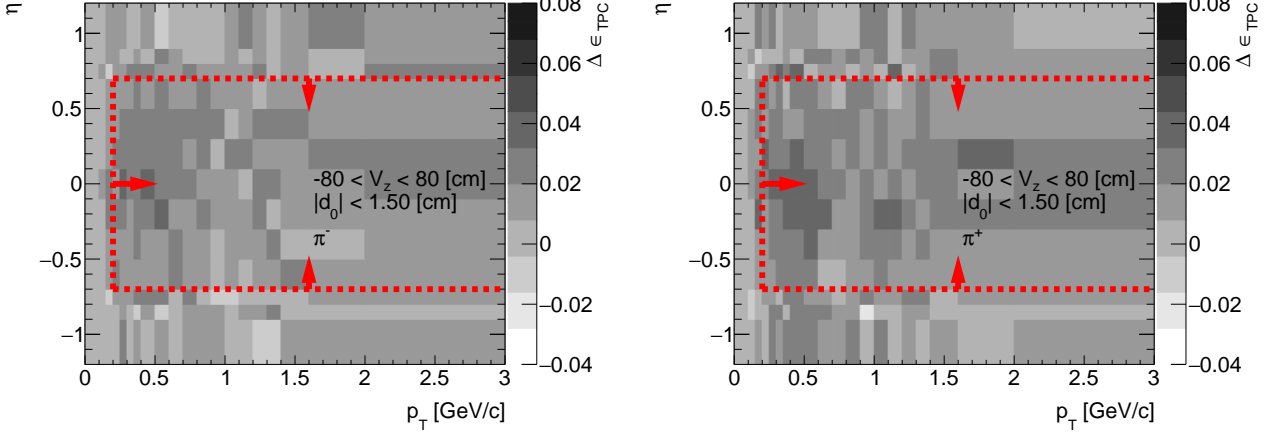


Figure 7.1: Number of events in embedded MC as a function of BBC_AND rate. The black and red lines represent the events with $\langle \text{BBC_AND} \rangle = 700 \text{ kHz}$ and $\langle \text{BBC_AND} \rangle = 1400 \text{ kHz}$, respectively.

Figure 7.3: The difference $\Delta\epsilon_{TPC} = \Delta\epsilon_{TPC}^{1400 \text{ kHz}} - 2 \cdot \Delta\epsilon_{TPC}^{700 \text{ kHz}}$ for π^\pm as a function of p_T and η ($|V_z| < 80 \text{ cm}$).



7.2 TOF matching efficiency systematics

The approach to calculate the systematic uncertainty related to TOF matching efficiency was quite similar to the one used for TPC track reconstruction efficiency. However, the TOF matching efficiency is conditional and depends on TPC track reconstruction efficiency. Since that, the difference between high and low pile-up runs is given by:

$$\Delta\epsilon_{TOF}^{1400/700 \text{ kHz}} = \frac{N_{TPC-TOF}^{no-pile-up}}{N_{TPC}^{no-pile-up}} - \frac{N_{TPC-TOF}^{pile-up}}{N_{TPC}^{pile-up}} \quad (7.3)$$

where:

$N_{TPC-TOF}^{pile-up}$ - number of reconstructed tracks, matched with MC tracks and TOF hit in pile-up MC,

$N_{TPC-TOF}^{no-pile-up}$ - number of reconstructed tracks, matched with MC tracks and TOF hit in no-pile-up MC,

$N_{TPC}^{pile-up}$ - number of reconstructed tracks, matched with MC tracks in pile-up MC,

$N_{TPC}^{no-pile-up}$ - number of reconstructed tracks, matched with MC tracks in no-pile-up MC.

Next the difference between high and low pile-up events was calculated with the formula similar to the one given by Eq. 7.2 and is shown in Figs. 7.4 and 7.5. The origin of $N_{TPC-TOF}$ increase is not known (it may be due to lack of pile-up in TPC or TOF). Since that, it is impossible to correctly calculate the statistical error for $\Delta\epsilon_{TOF}$. Nevertheless, $\Delta\epsilon_{TOF}$ is smaller than 0.5% and can be neglected in comparison with other systematic uncertainties.

Figure 7.4: π^\pm TOF matching efficiency as a function of p_T ($|\eta| < 0.7$, $|V_z| < 80 \text{ cm}$) for embedded MC samples with $\langle \text{BBC_AND} \rangle \geq 700 \text{ kHz}$ and $\langle \text{BBC_AND} \rangle \geq 1400 \text{ kHz}$. The efficiencies from corresponding no-pile-up MC samples were also shown. Additionally, the differences from Eq. 7.2 were drawn in the bottom of each plot.

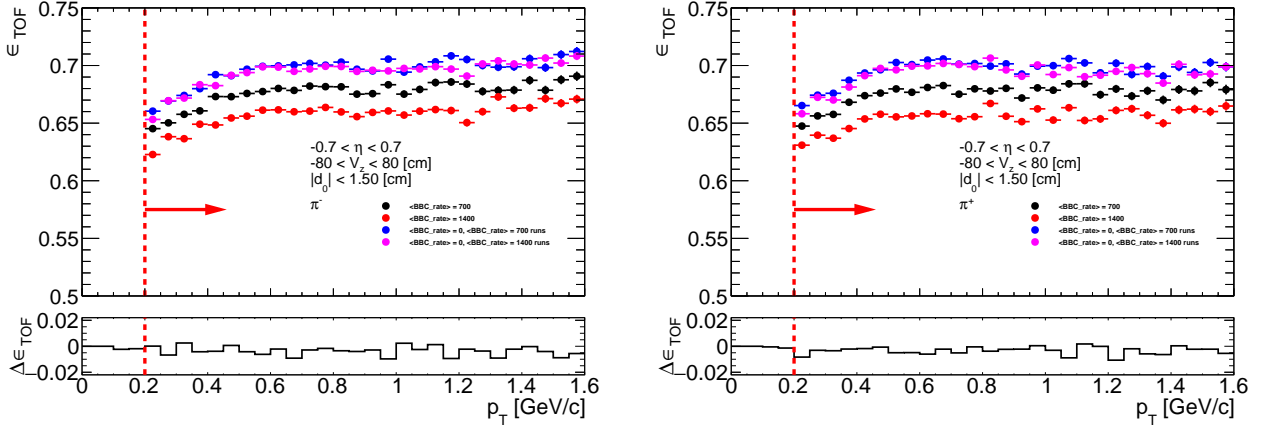
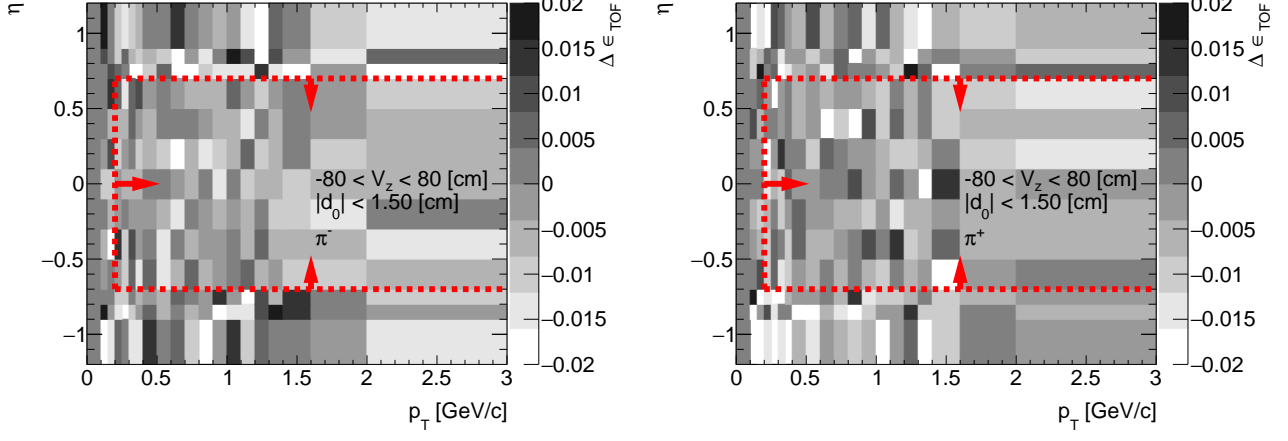


Figure 7.5: The difference $\Delta\epsilon_{TOF} = \Delta\epsilon_{TOF}^{1400 \text{ kHz}} - 2 \cdot \Delta\epsilon_{TOF}^{700 \text{ kHz}}$ for π^\pm as a function of p_T and η ($|V_z| < 80 \text{ cm}$).



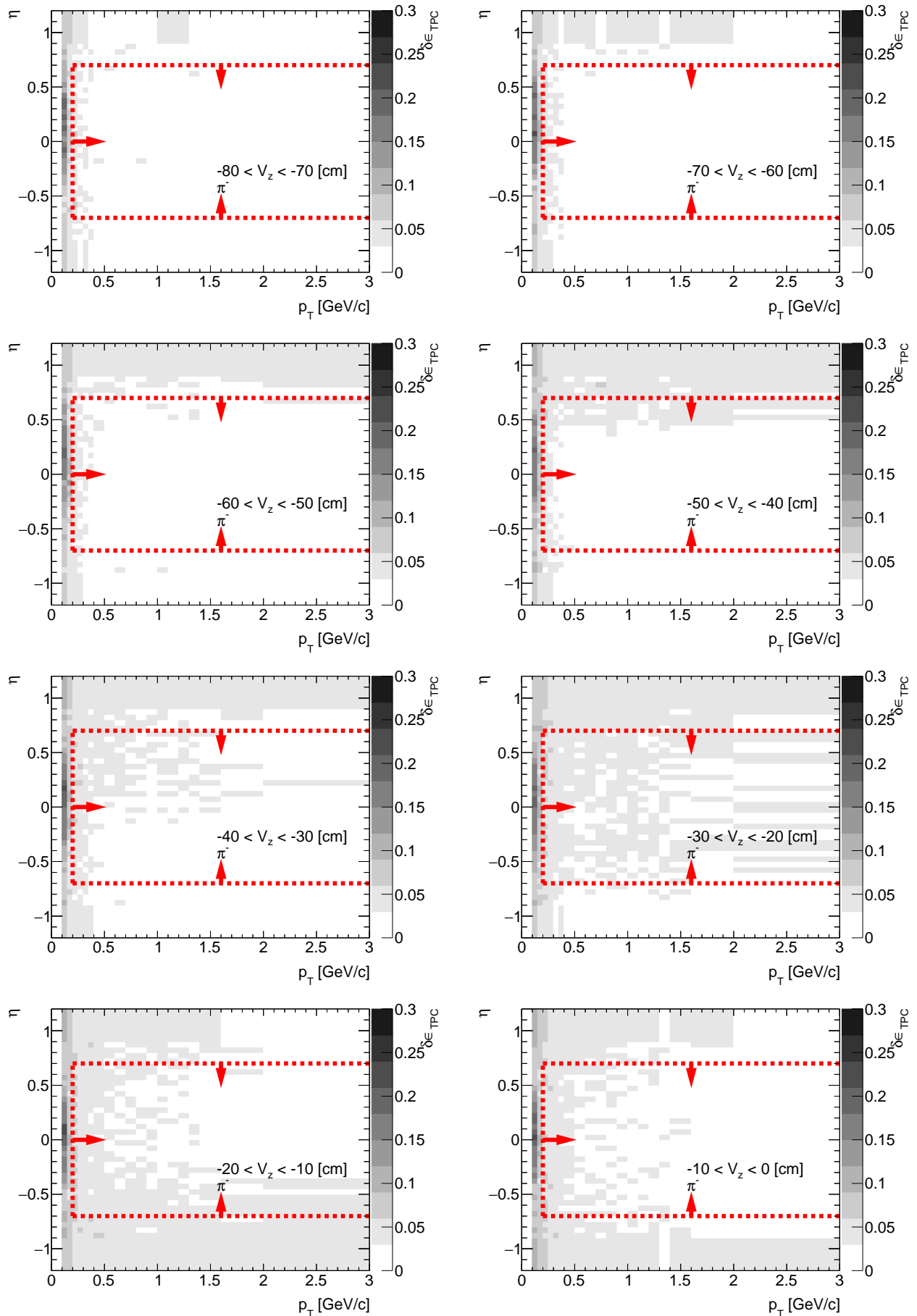
7.3 Dead material correction to TPC track reconstruction efficiency

The amount of dead material in front of TPC is underestimated of about 40% in the simulation. First, the amount of lost particles, $\delta\epsilon_{TPC}$, due to the interaction with dead material in front of TPC was estimated using no-pile-up MC samples. The results for π^- in CD are shown in Fig. 7.6. The correction to the TPC track reconstruction efficiency with the systematic uncertainty was introduced:

1. The correction due to the underestimation of the dead material was assumed to be $-0.2 \cdot \delta\epsilon_{TPC}$.
2. The systematic uncertainty was symmetrized and equal to $\pm 0.2 \cdot \delta\epsilon_{TPC}$.

In Fig. 7.7 the correction $|0.2 \cdot \delta\epsilon_{TPC}|$ with the corresponding systematic uncertainty is shown for each particle species in CD as a function of p_T ($|\eta| < 0.7$, $|V_z| < 80 \text{ cm}$). The results for other particles and SD are shown in Figs. in Appendix B.

Figure 7.6: The amount of lost π^- due to the interaction with dead material in front of TPC. Each plot represents the fraction of lost π^- , $\delta\epsilon_{TPC}$ (z-axis), as a function of true particle pseudorapidity η (y-axis) and transverse momentum p_T (x-axis) in single z -vertex bin.



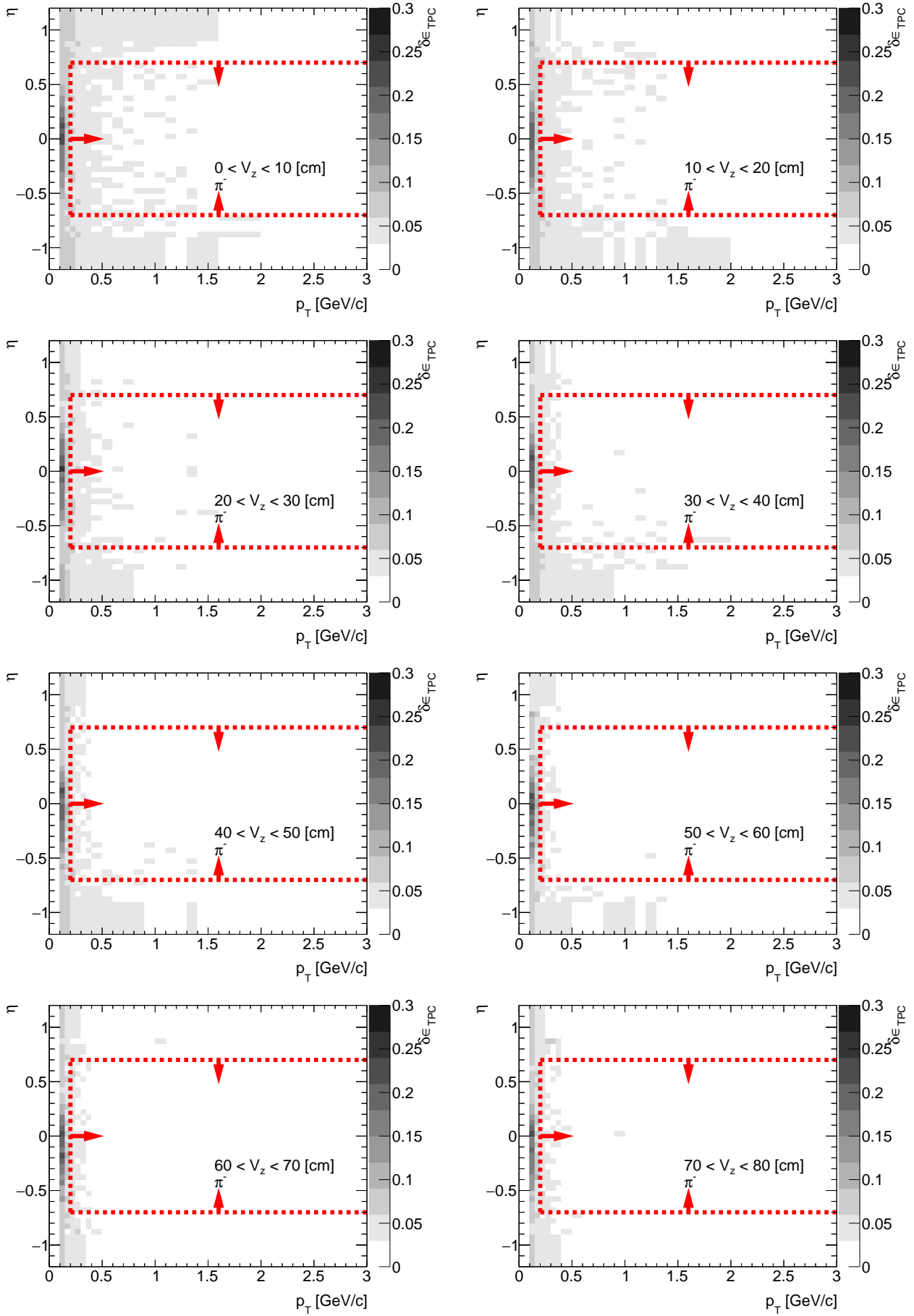
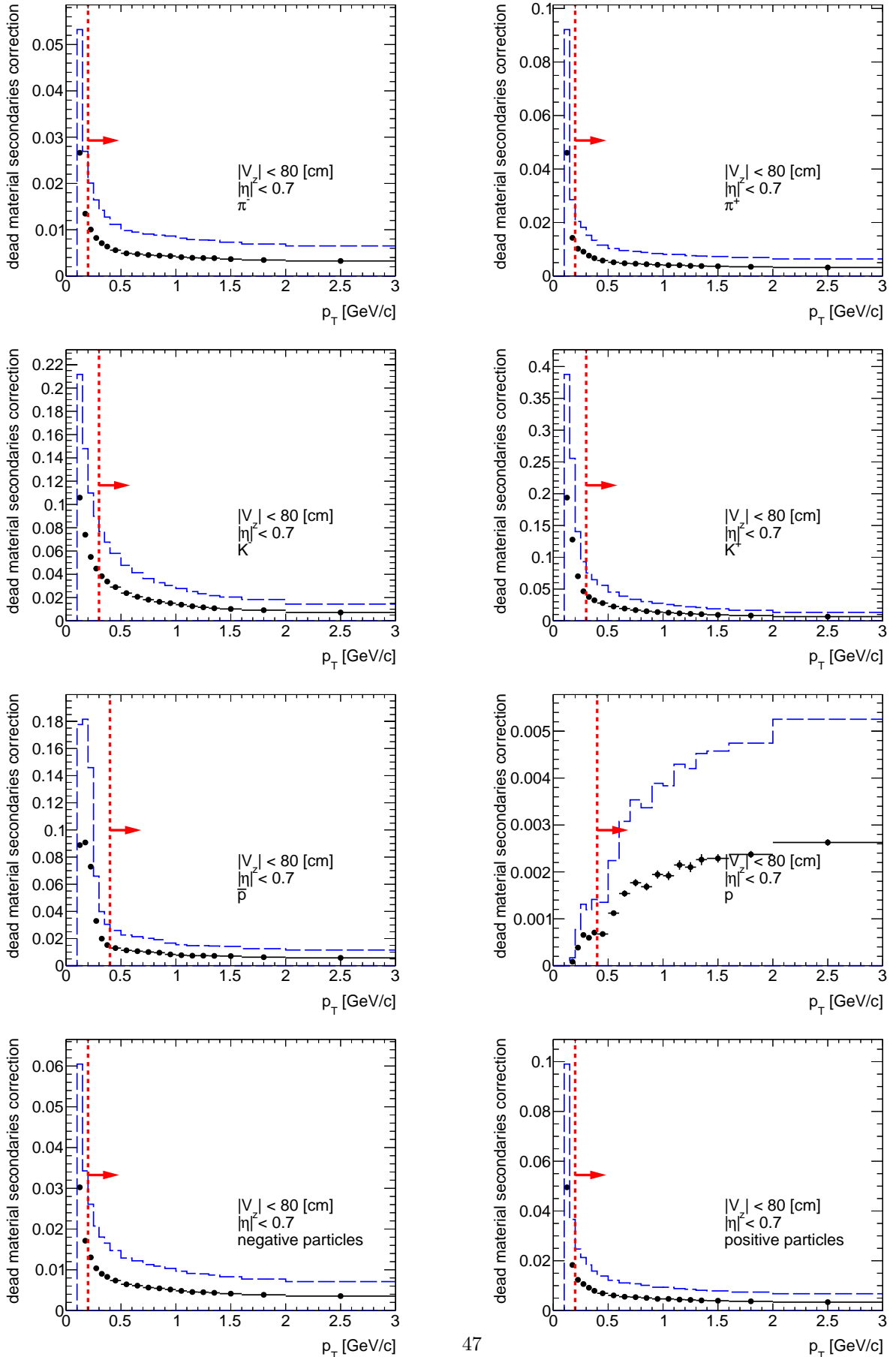


Figure 7.7: The correction to the TPC track reconstruction efficiency $|0.2 \cdot \delta\epsilon_{TPC}|$ due to underestimated amount of dead material in front of TPC using MC samples for CD. Each plot represents the correction as a function of true particle p_T ($|\eta| < 0.7, |V_z| < 80$ cm) for given particle species: $\pi^-, \pi^+, K^-, K^+, \bar{p}$ and p . It was also calculated for negative and positive particles without identification. The corresponding systematic uncertainties are shown with blue dotted lines.



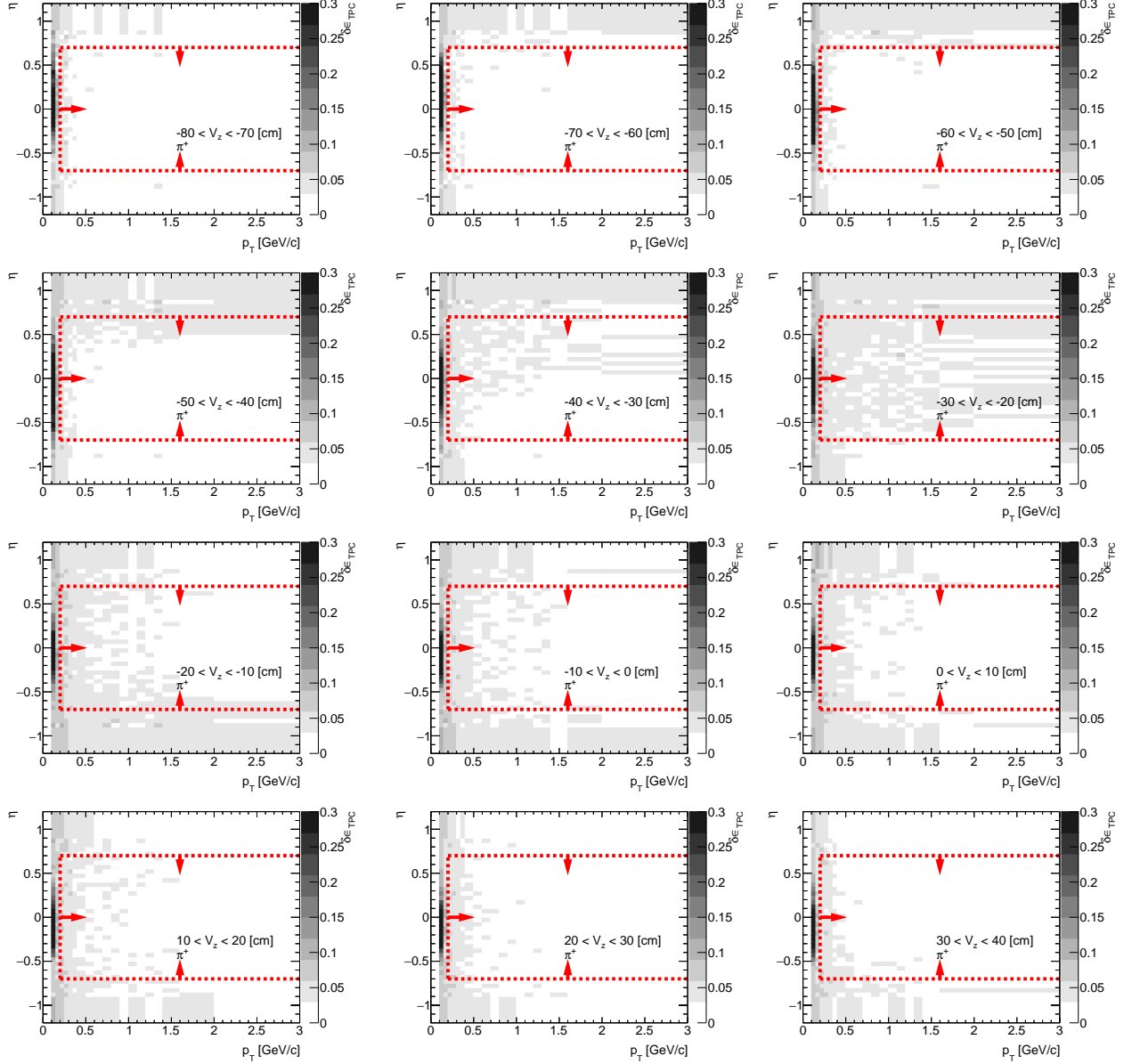
Appendix A

Energy Loss Correction

Appendix B

Dead material correction to TPC track reconstruction efficiency

Figure B.1: The amount of lost π^- due to the interaction with dead material in front of TPC in CD MC sample. Each plot represents the fraction of lost π^+ , $\delta\epsilon_{TPC}$ (z -axis), as a function of true particle pseudorapidity η (y -axis) and transverse momentum p_T (x -axis) in single z -vertex bin.



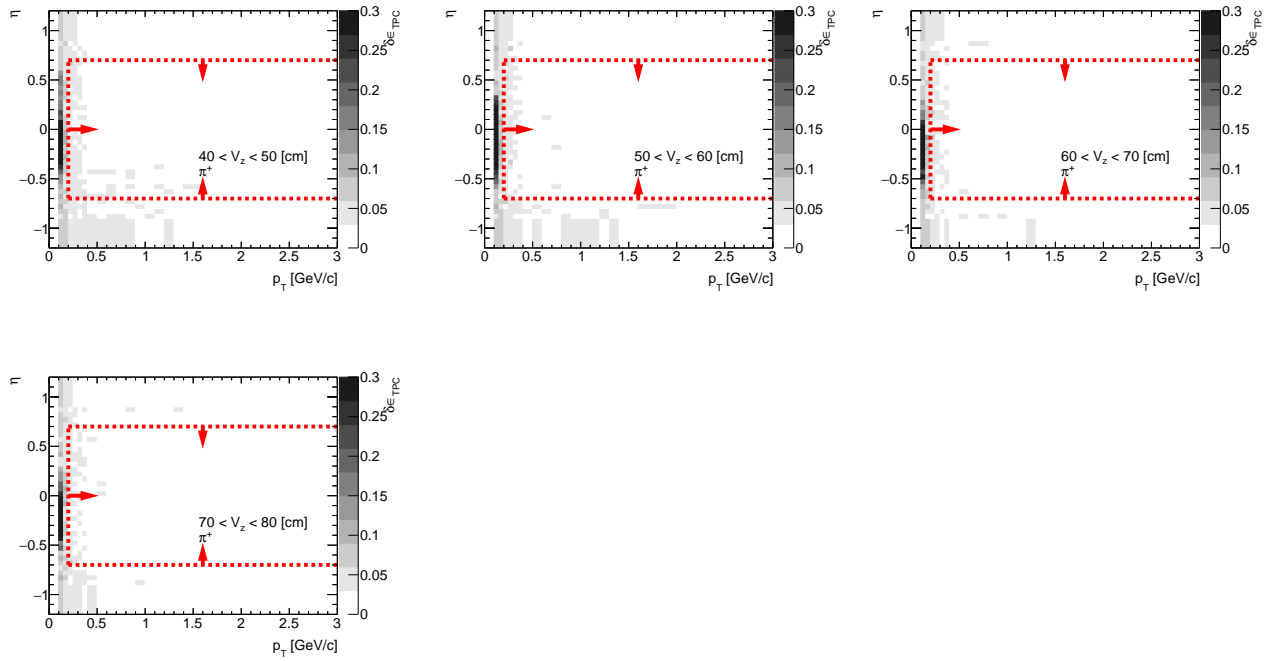


Figure B.2: The amount of lost K^- due to the interaction with dead material in front of TPC in CD MC sample. Each plot represents the fraction of lost K^- , $\delta\epsilon_{TPC}$ (z -axis), as a function of true particle pseudorapidity η (y -axis) and transverse momentum p_T (x -axis) in single z -vertex bin.

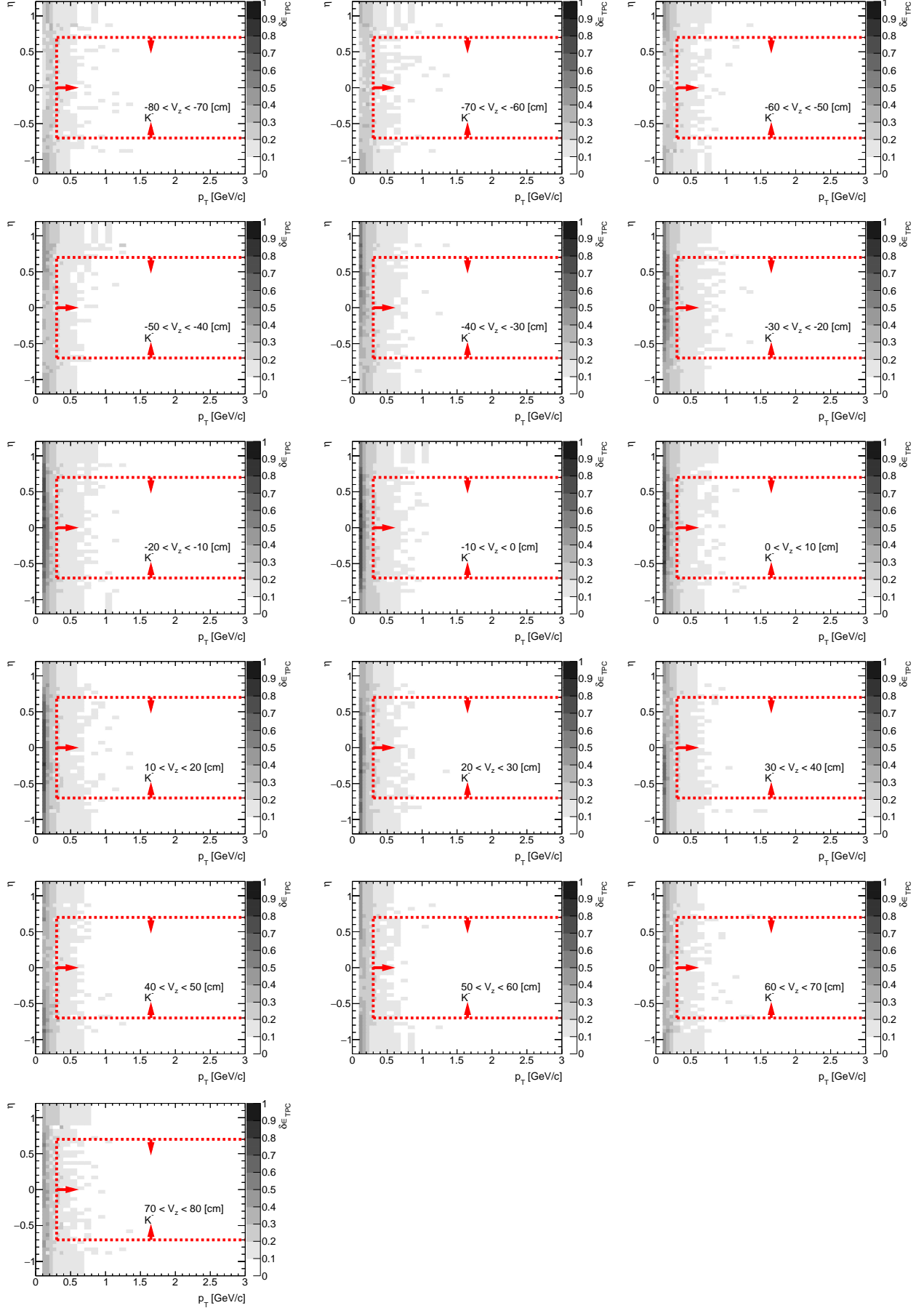


Figure B.3: The amount of lost K^+ due to the interaction with dead material in front of TPC in CD MC sample. Each plot represents the fraction of lost K^+ , $\delta\epsilon_{TPC}$ (z -axis), as a function of true particle pseudorapidity η (y -axis) and transverse momentum p_T (x -axis) in single z -vertex bin.

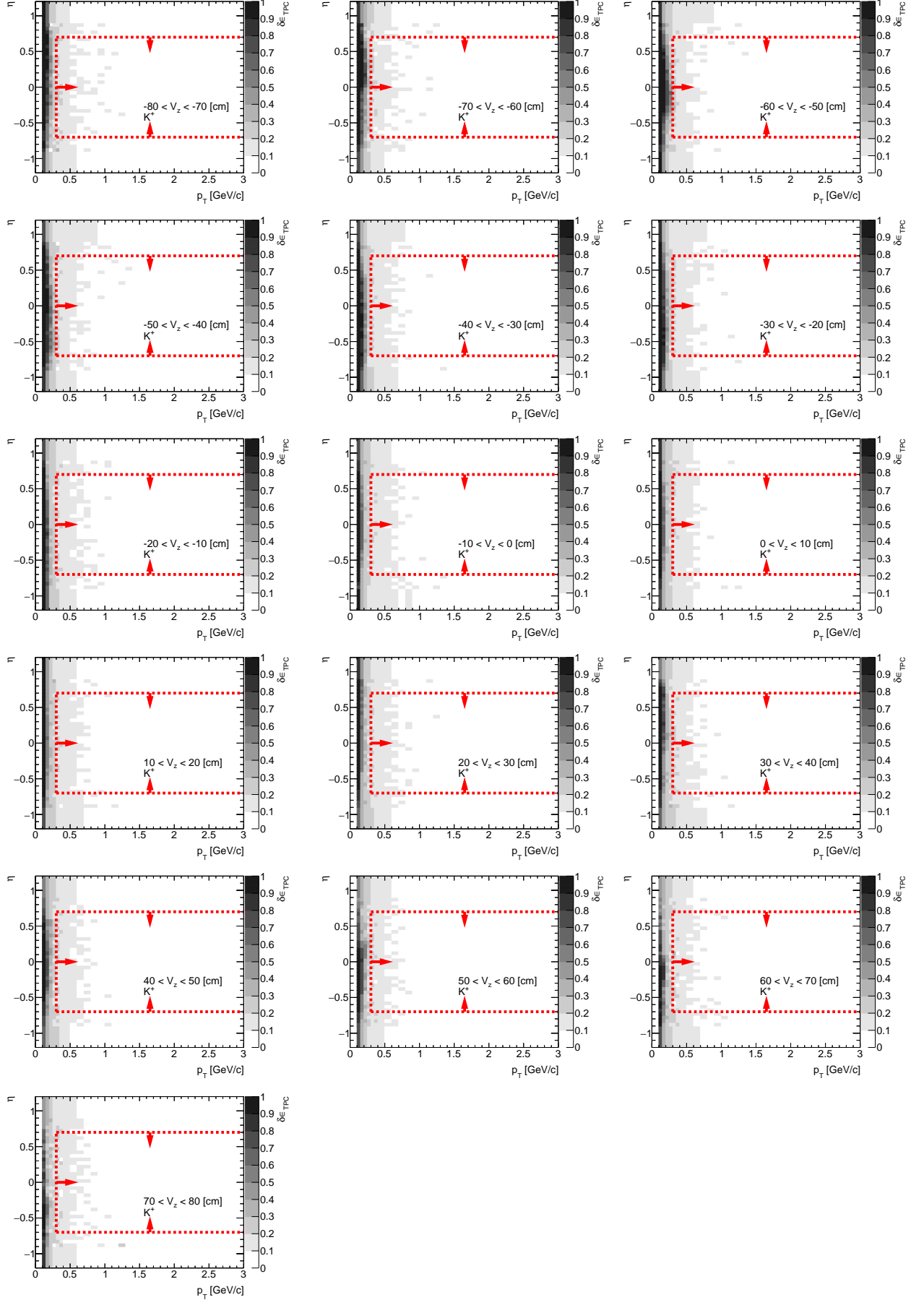


Figure B.4: The amount of lost \bar{p} due to the interaction with dead material in front of TPC in CD MC sample. Each plot represents the fraction of lost \bar{p} , $\delta\epsilon_{TPC}$ (z -axis), as a function of true particle pseudorapidity η (y -axis) and transverse momentum p_T (x -axis) in single z -vertex bin.

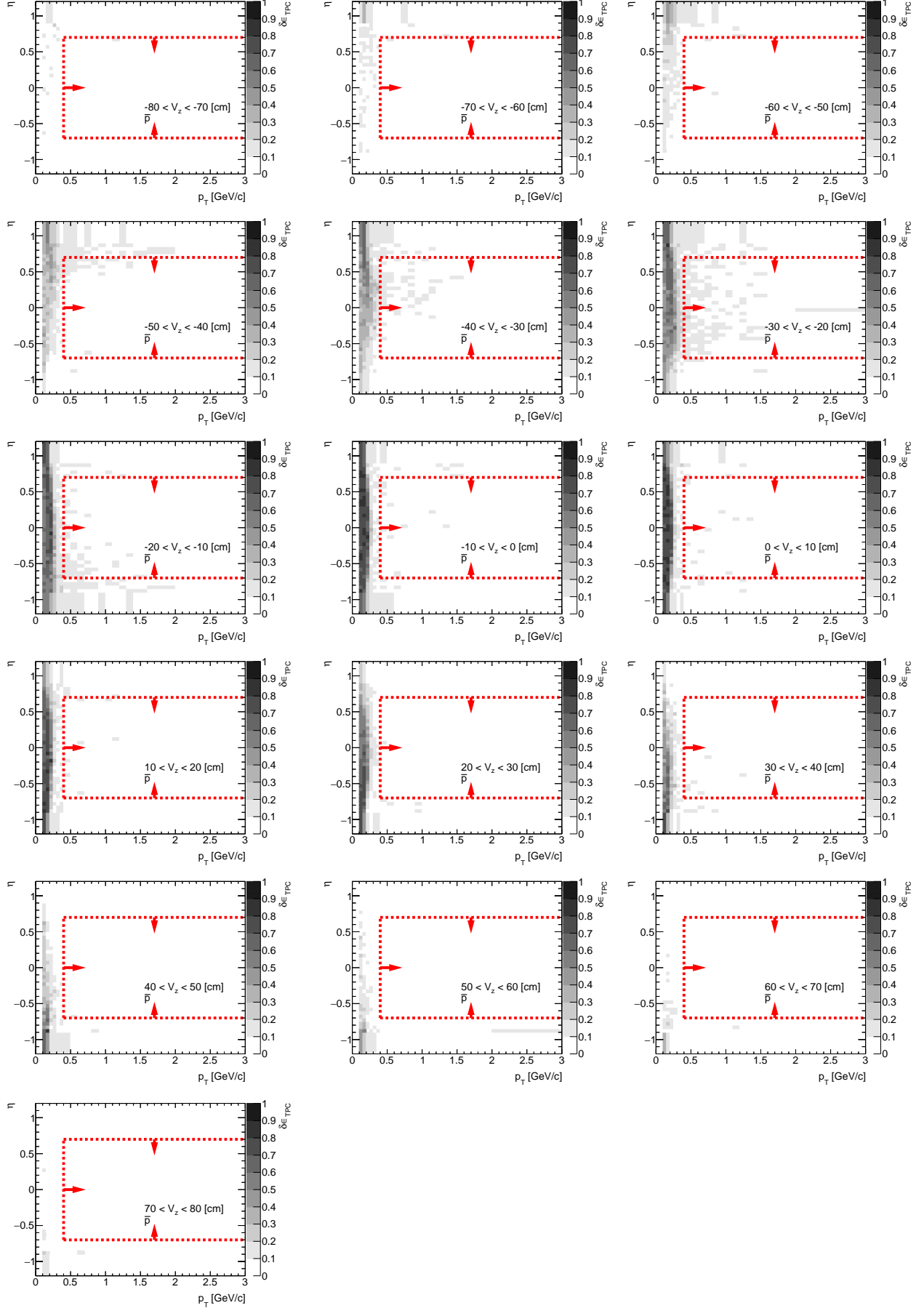


Figure B.5: The amount of lost p due to the interaction with dead material in front of TPC in CD MC sample. Each plot represents the fraction of lost p , $\delta\epsilon_{TPC}$ (z -axis), as a function of true particle pseudorapidity η (y -axis) and transverse momentum p_T (x -axis) in single z -vertex bin.

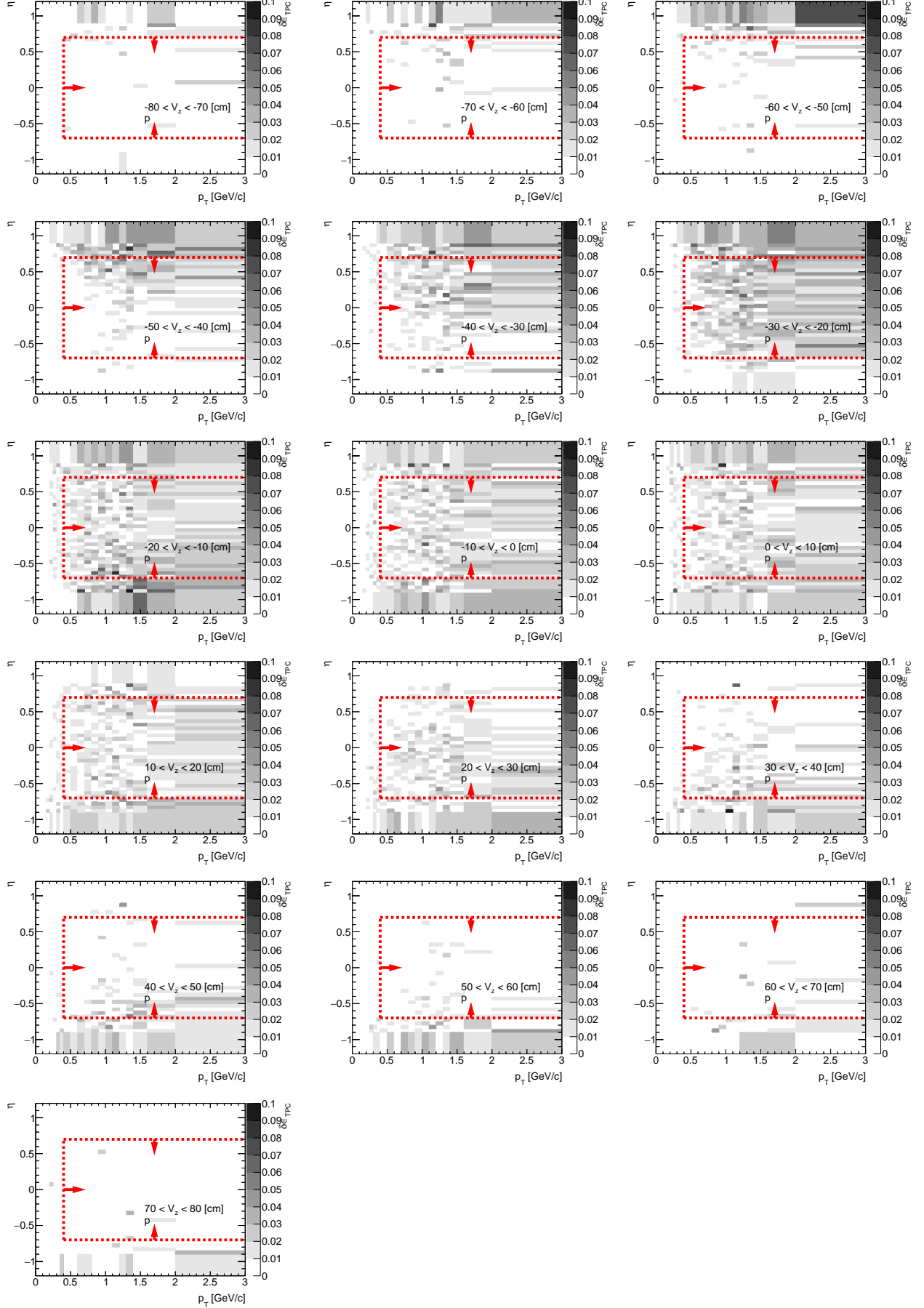


Figure B.6: The amount of lost negative particles due to the interaction with dead material in front of TPC in CD MC sample. Each plot represents the fraction of lost negative particles, $\delta\epsilon_{TPC}$ (z-axis), as a function of true particle pseudorapidity η (y-axis) and transverse momentum p_T (x-axis) in single z -vertex bin.

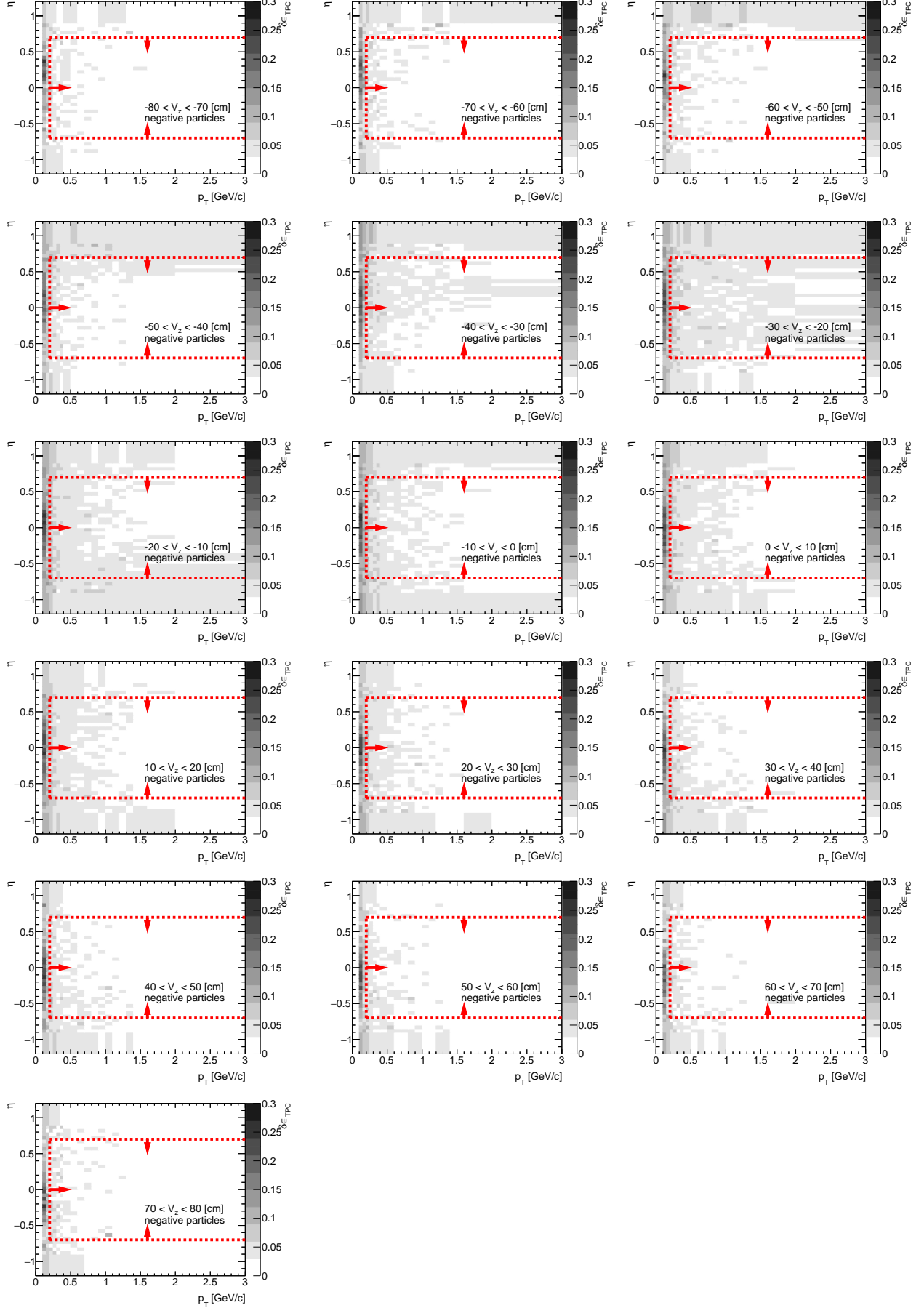


Figure B.7: The amount of lost positive particles due to the interaction with dead material in front of TPC in CD MC sample. Each plot represents the fraction of lost positive particles, $\delta\epsilon_{TPC}$ (z-axis), as a function of true particle pseudorapidity η (y-axis) and transverse momentum p_T (x-axis) in single z -vertex bin.

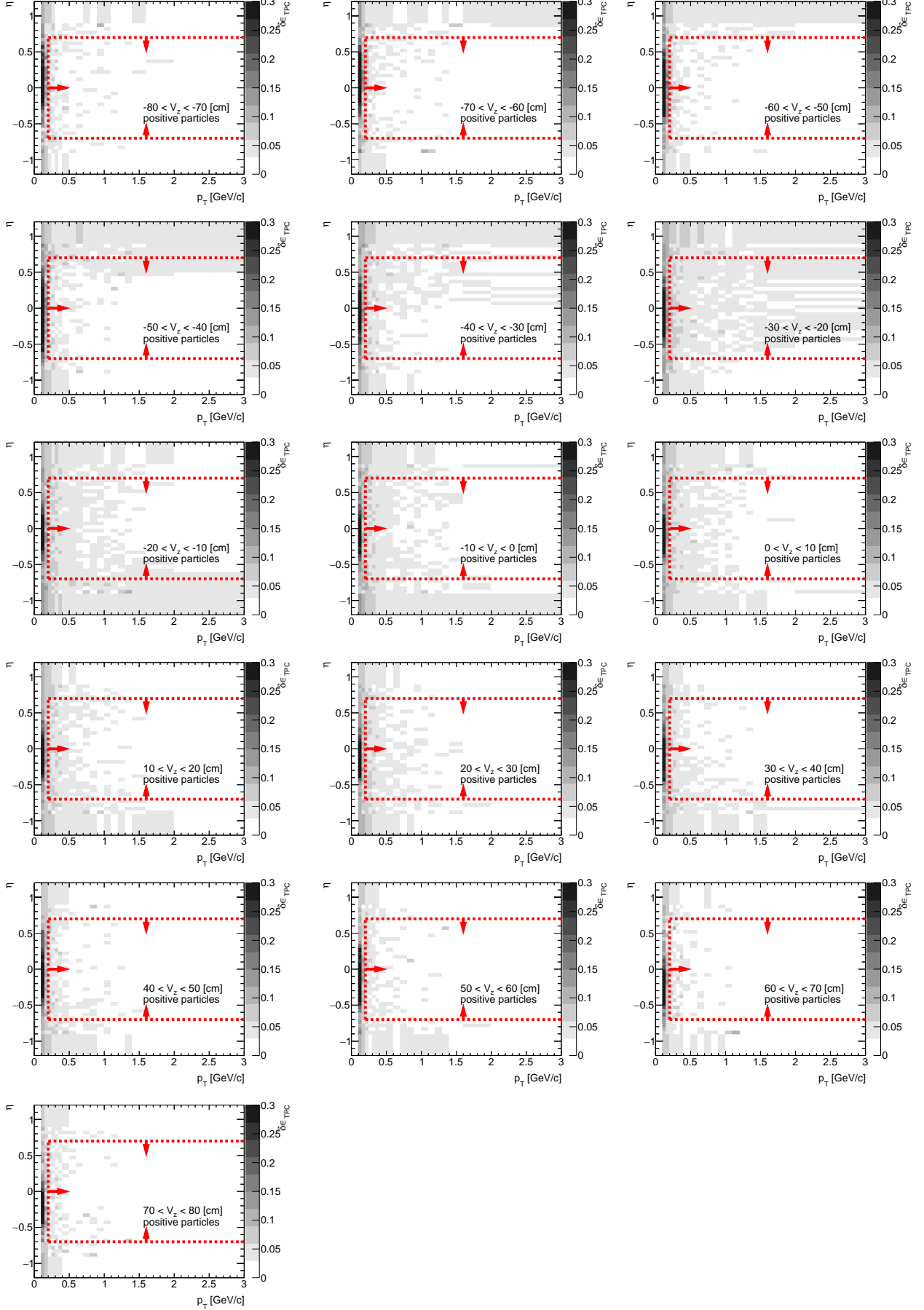


Figure B.8: The amount of lost π^- due to the interaction with dead material in front of TPC in SD MC sample. Each plot represents the fraction of lost π^- , $\delta\epsilon_{TPC}$ (z -axis), as a function of true particle pseudorapidity η (y -axis) and transverse momentum p_T (x -axis) in single z -vertex bin.

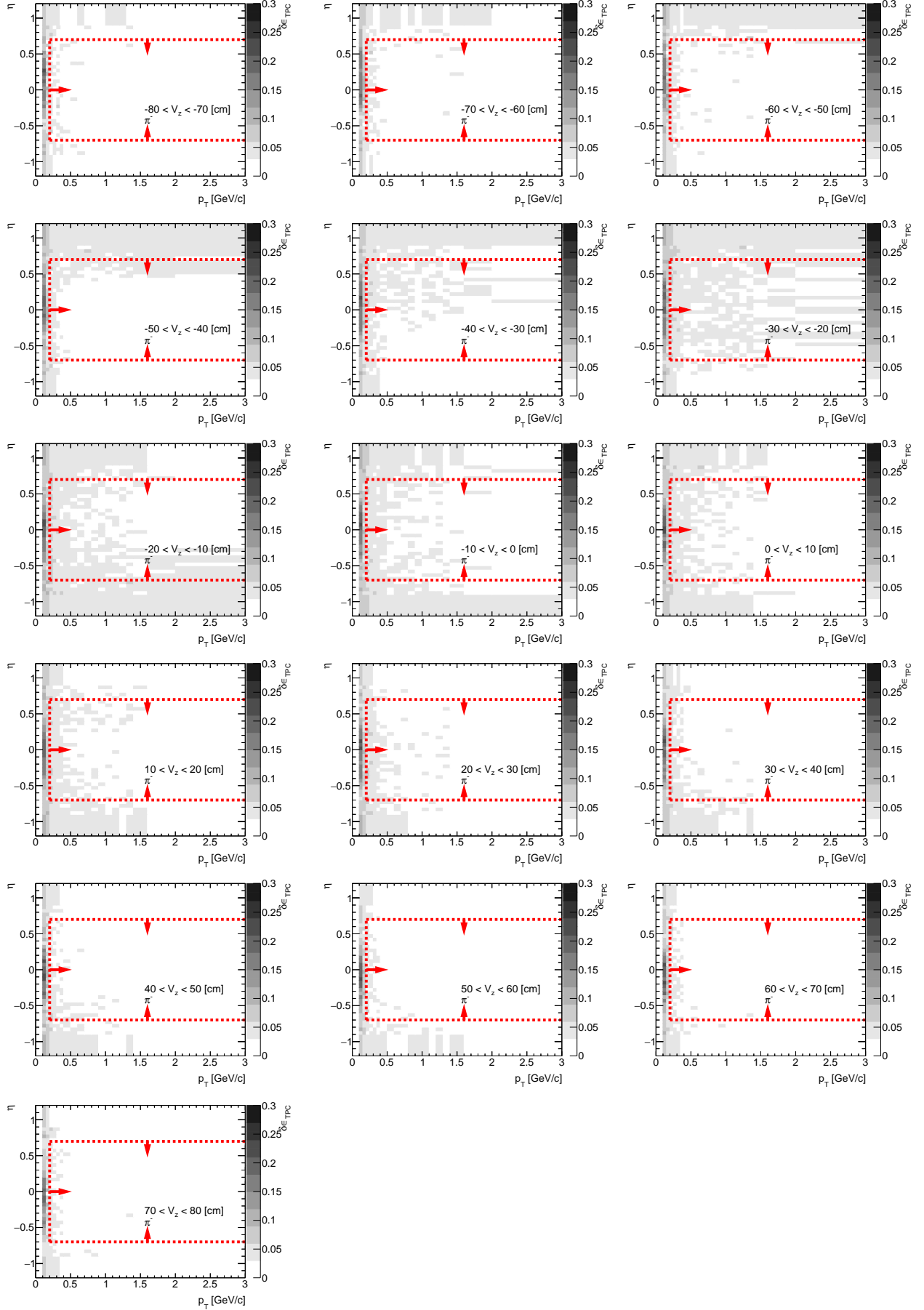


Figure B.9: The amount of lost π^+ due to the interaction with dead material in front of TPC in SD MC sample. Each plot represents the fraction of lost π^+ , $\delta\epsilon_{TPC}$ (z -axis), as a function of true particle pseudorapidity η (y -axis) and transverse momentum p_T (x -axis) in single z -vertex bin.

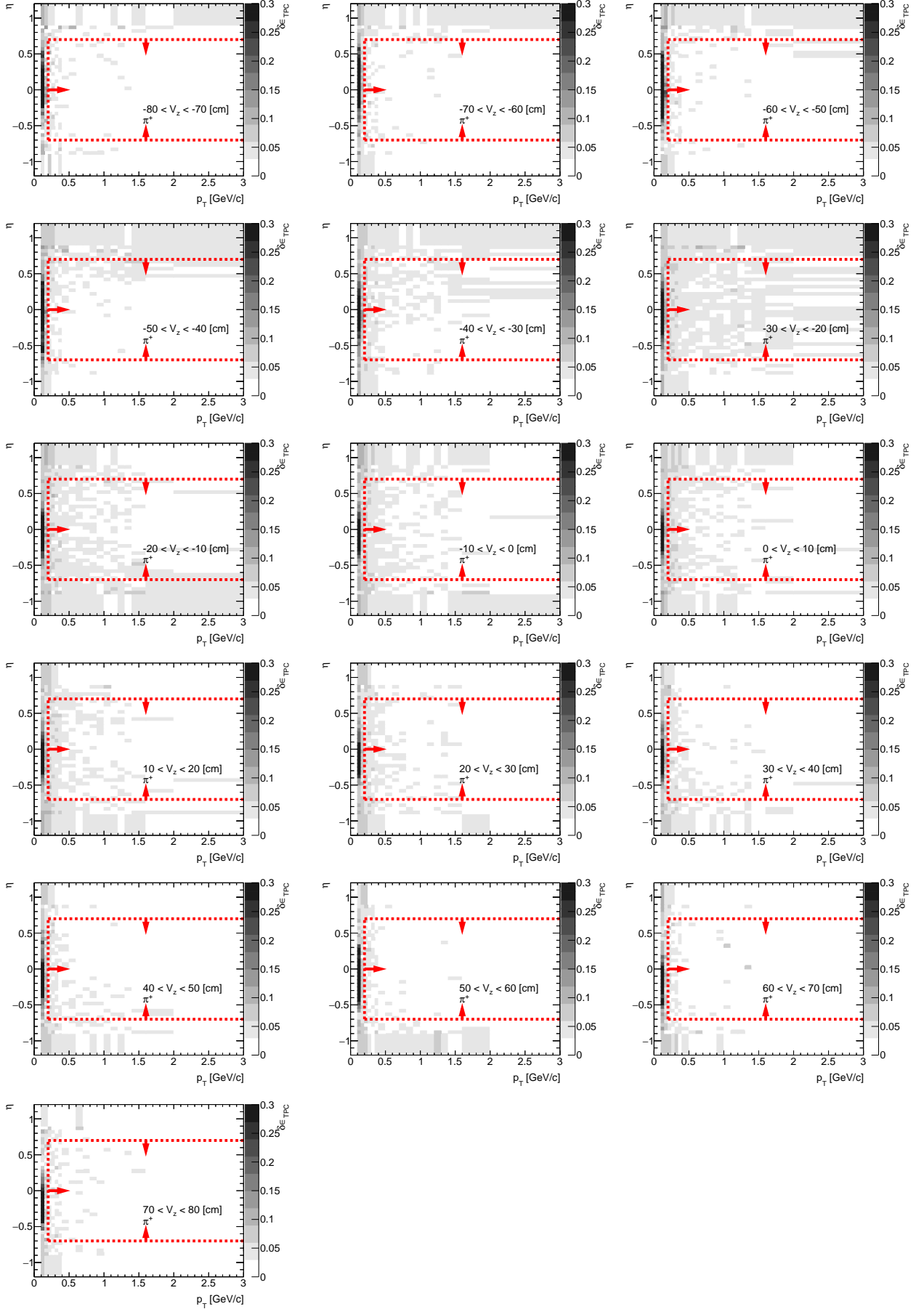


Figure B.10: The amount of lost K^- due to the interaction with dead material in front of TPC in SD MC sample. Each plot represents the fraction of lost K^- , $\delta\epsilon_{TPC}$ (z -axis), as a function of true particle pseudorapidity η (y -axis) and transverse momentum p_T (x -axis) in single z -vertex bin.

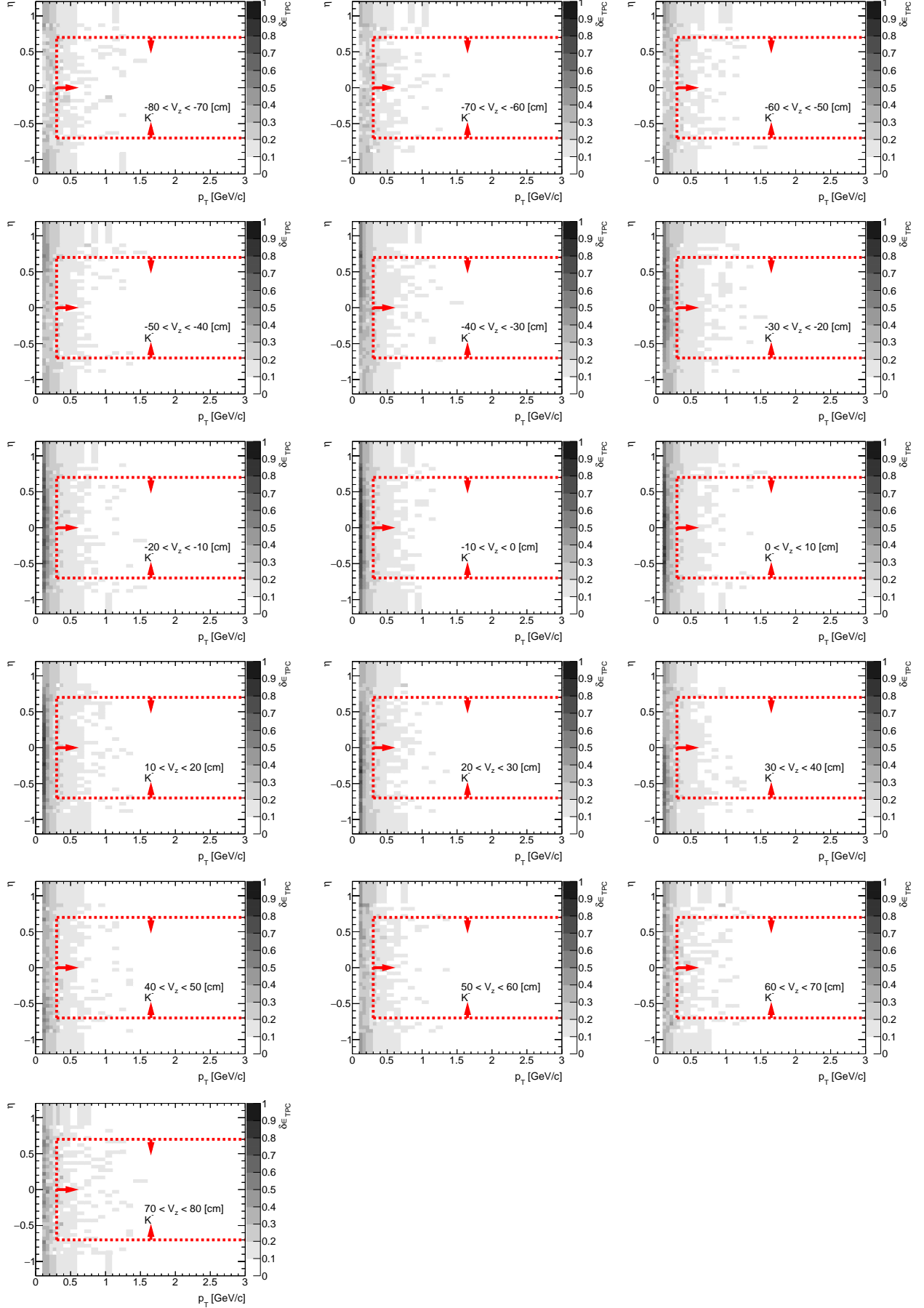


Figure B.11: The amount of lost K^+ due to the interaction with dead material in front of TPC in SD MC sample. Each plot represents the fraction of lost K^+ , $\delta\epsilon_{TPC}$ (z -axis), as a function of true particle pseudorapidity η (y -axis) and transverse momentum p_T (x -axis) in single z -vertex bin.

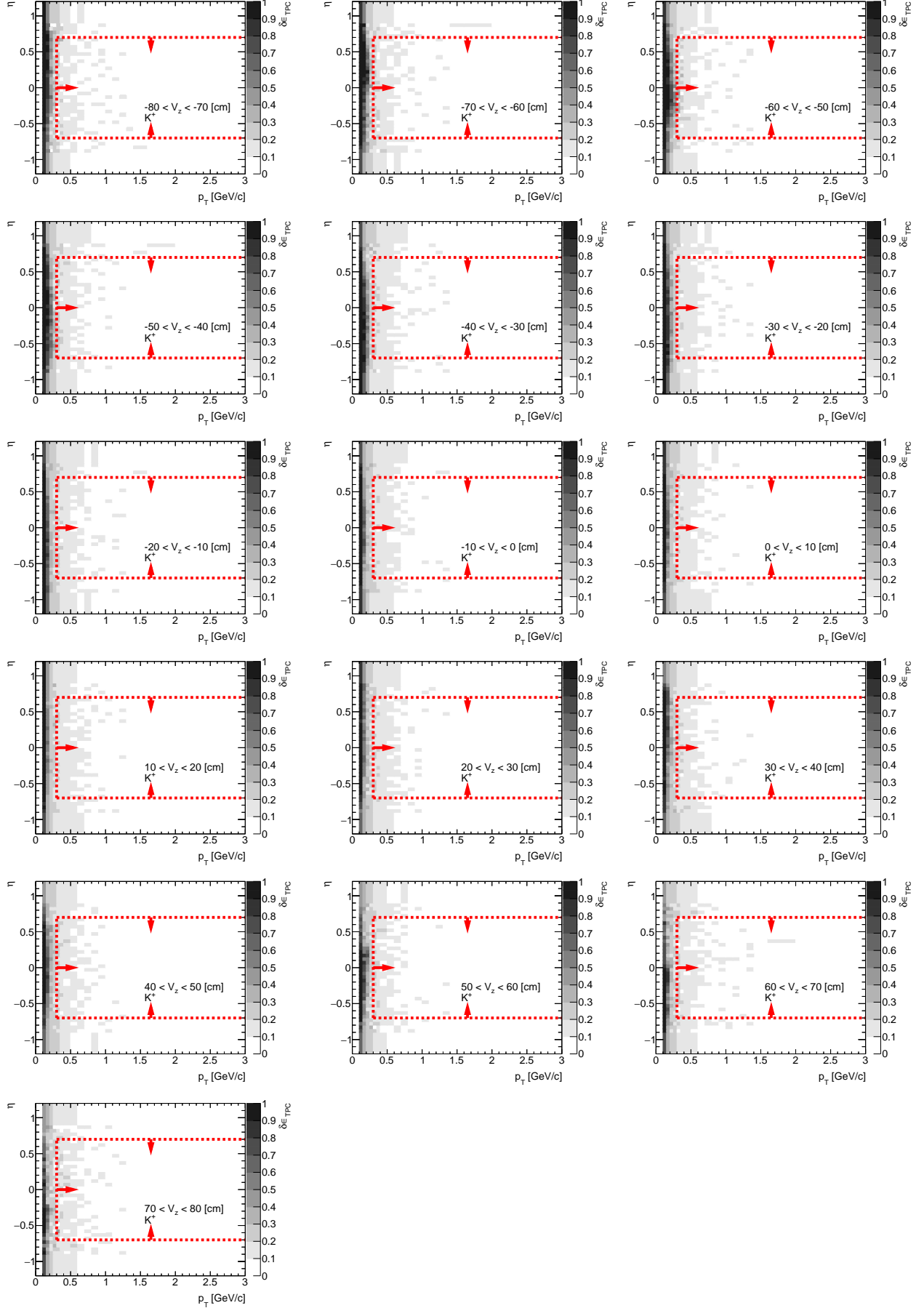


Figure B.12: The amount of lost \bar{p} due to the interaction with dead material in front of TPC in SD MC sample. Each plot represents the fraction of lost \bar{p} , $\delta\epsilon_{TPC}$ (z -axis), as a function of true particle pseudorapidity η (y -axis) and transverse momentum p_T (x -axis) in single z -vertex bin.

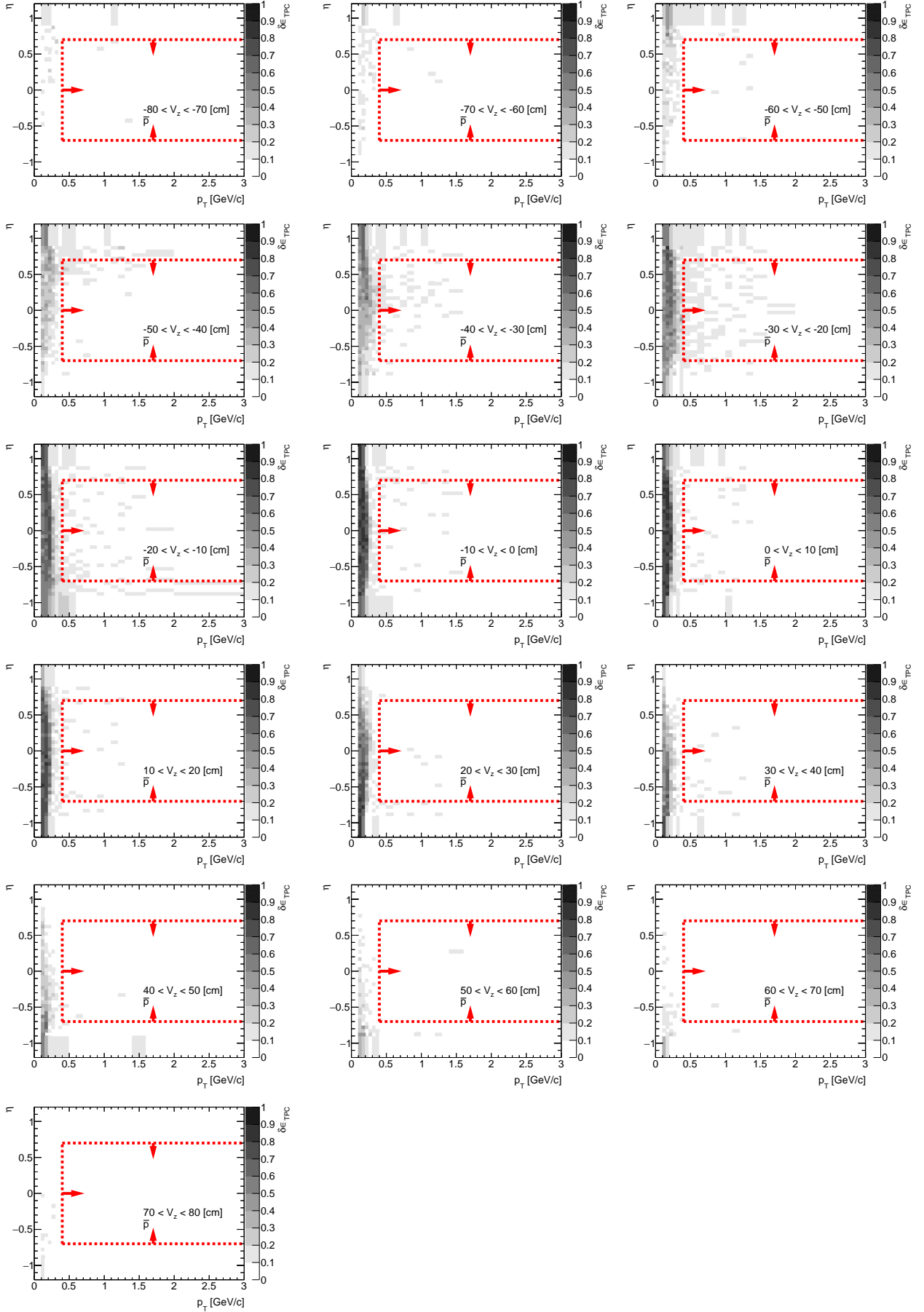


Figure B.13: The amount of lost p due to the interaction with dead material in front of TPC in SD MC sample. Each plot represents the fraction of lost p , $\delta\epsilon_{TPC}$ (z -axis), as a function of true particle pseudorapidity η (y -axis) and transverse momentum p_T (x -axis) in single z -vertex bin.

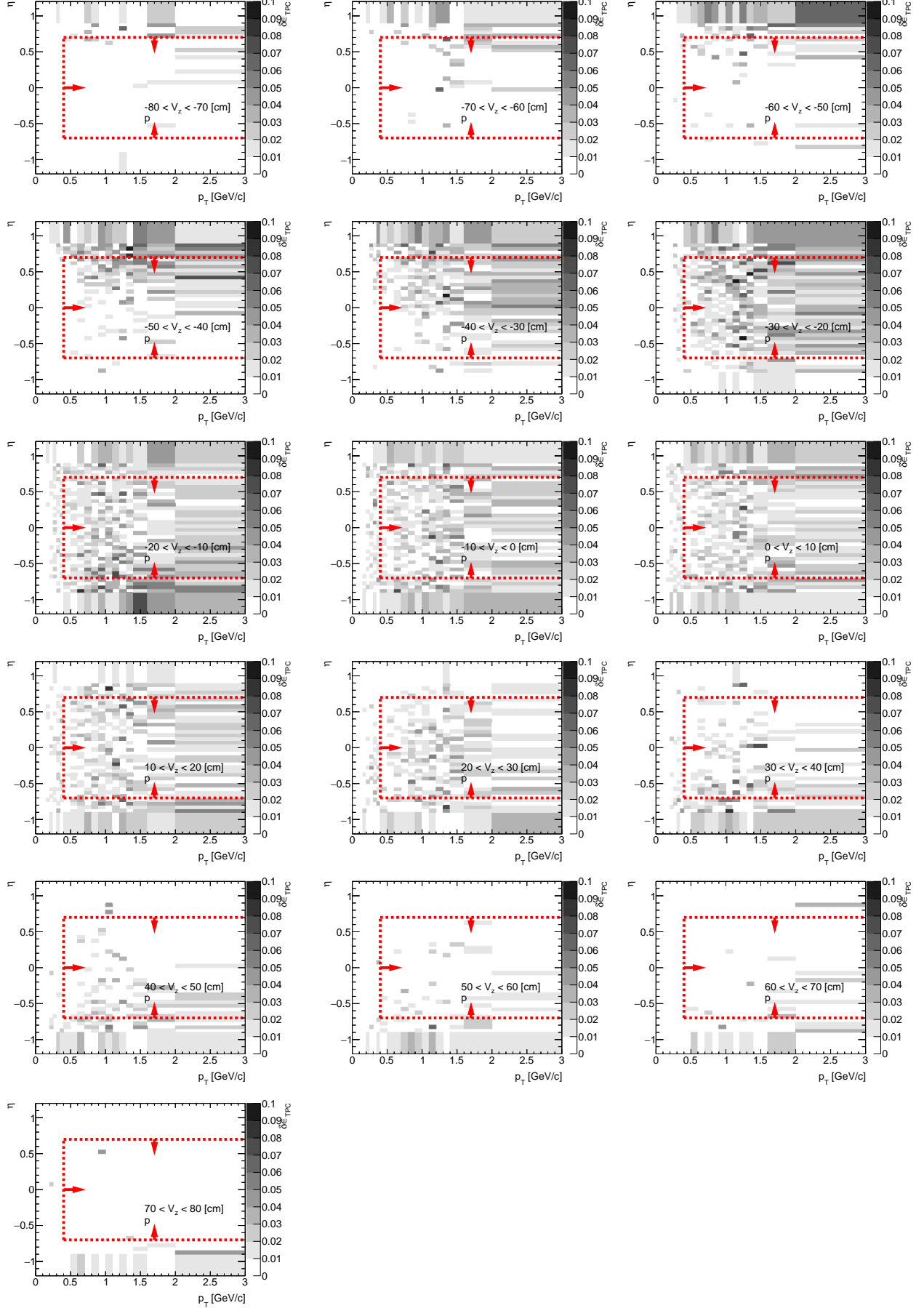


Figure B.14: The amount of lost negative particles due to the interaction with dead material in front of TPC in SD MC sample. Each plot represents the fraction of lost negative particles, $\delta\epsilon_{TPC}$ (z-axis), as a function of true particle pseudorapidity η (y-axis) and transverse momentum p_T (x-axis) in single z -vertex bin.

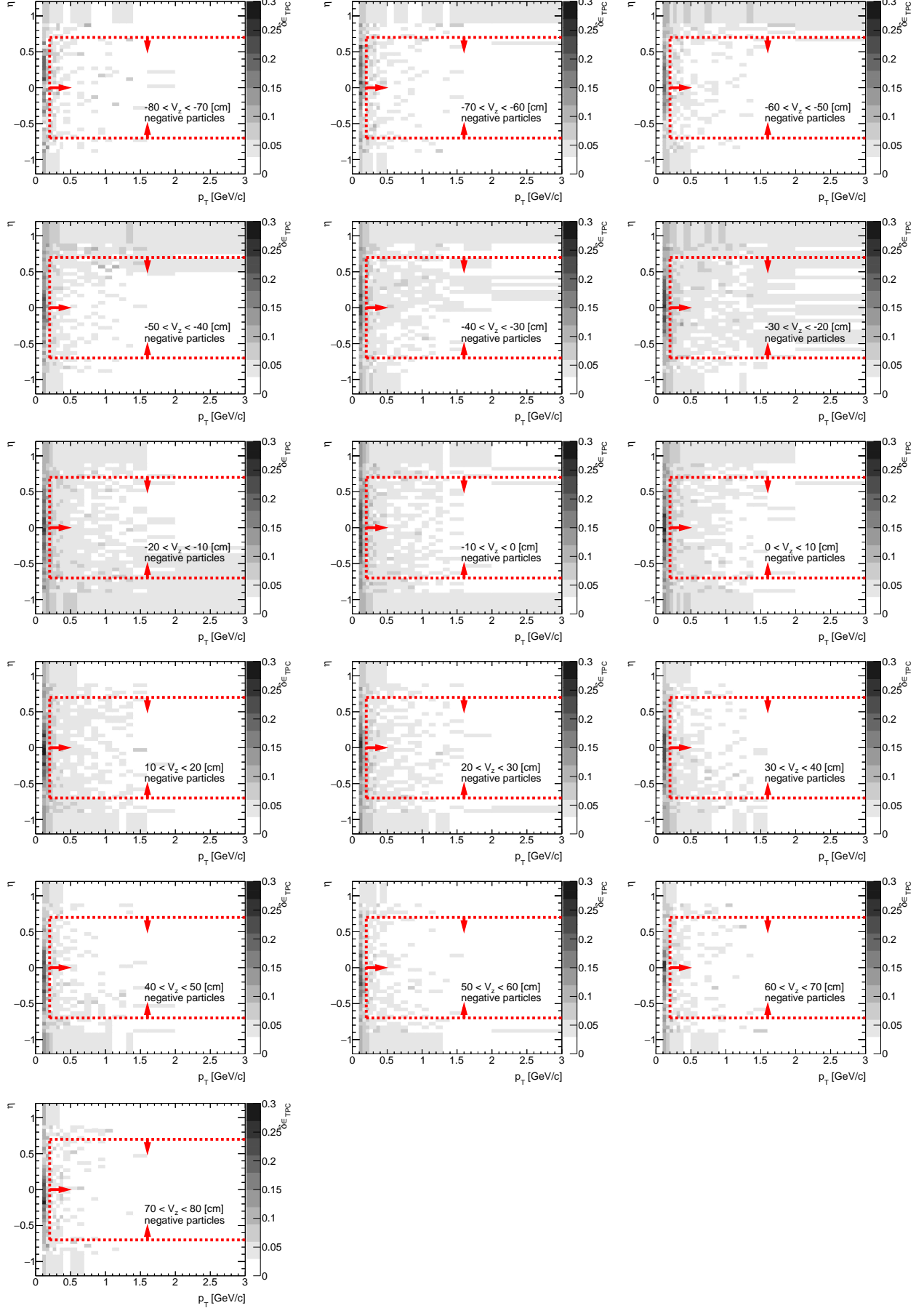


Figure B.15: The amount of lost positive particles due to the interaction with dead material in front of TPC in SD MC sample. Each plot represents the fraction of lost positive particles, $\delta\epsilon_{TPC}$ (z-axis), as a function of true particle pseudorapidity η (y-axis) and transverse momentum p_T (x-axis) in single z -vertex bin.

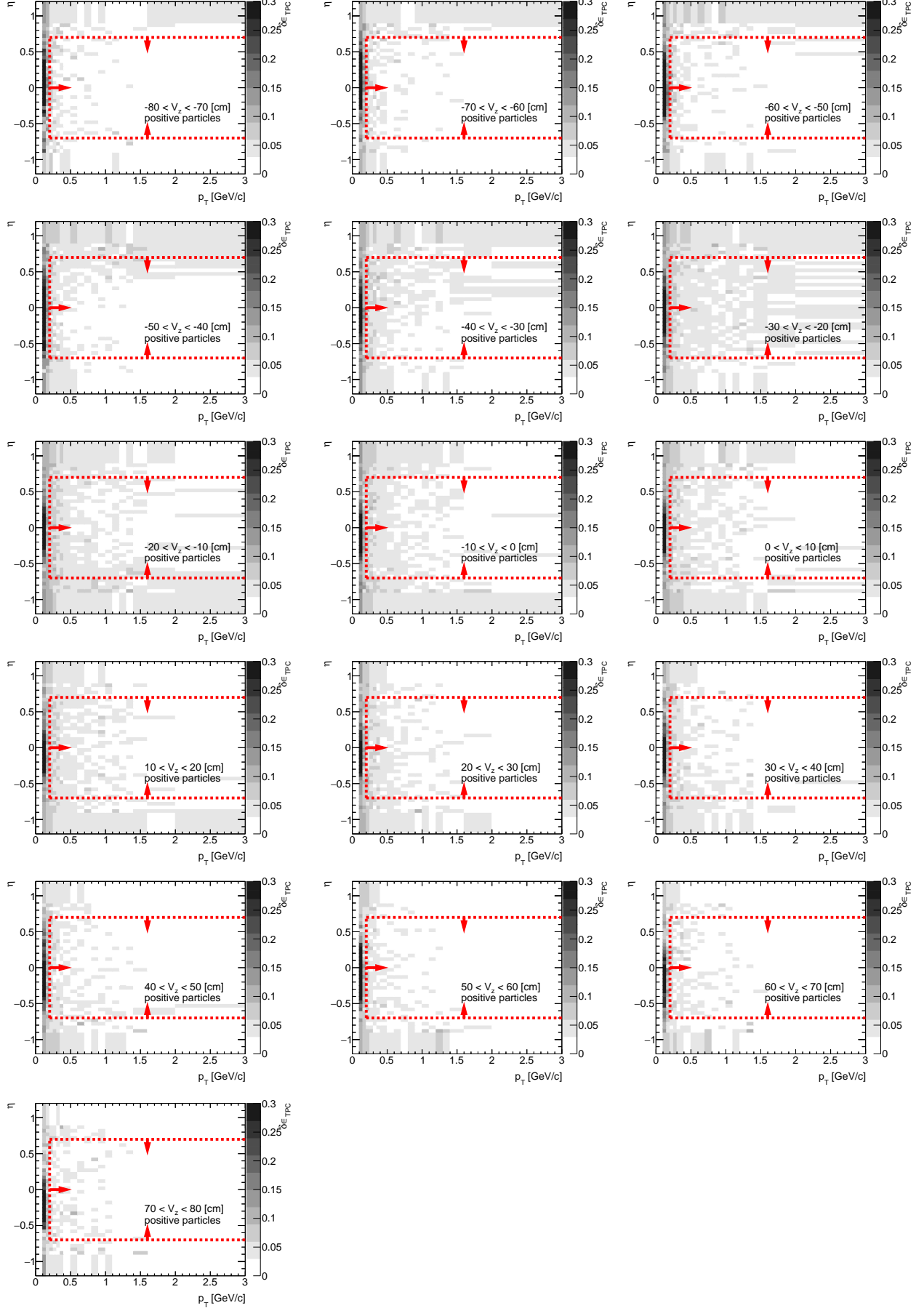
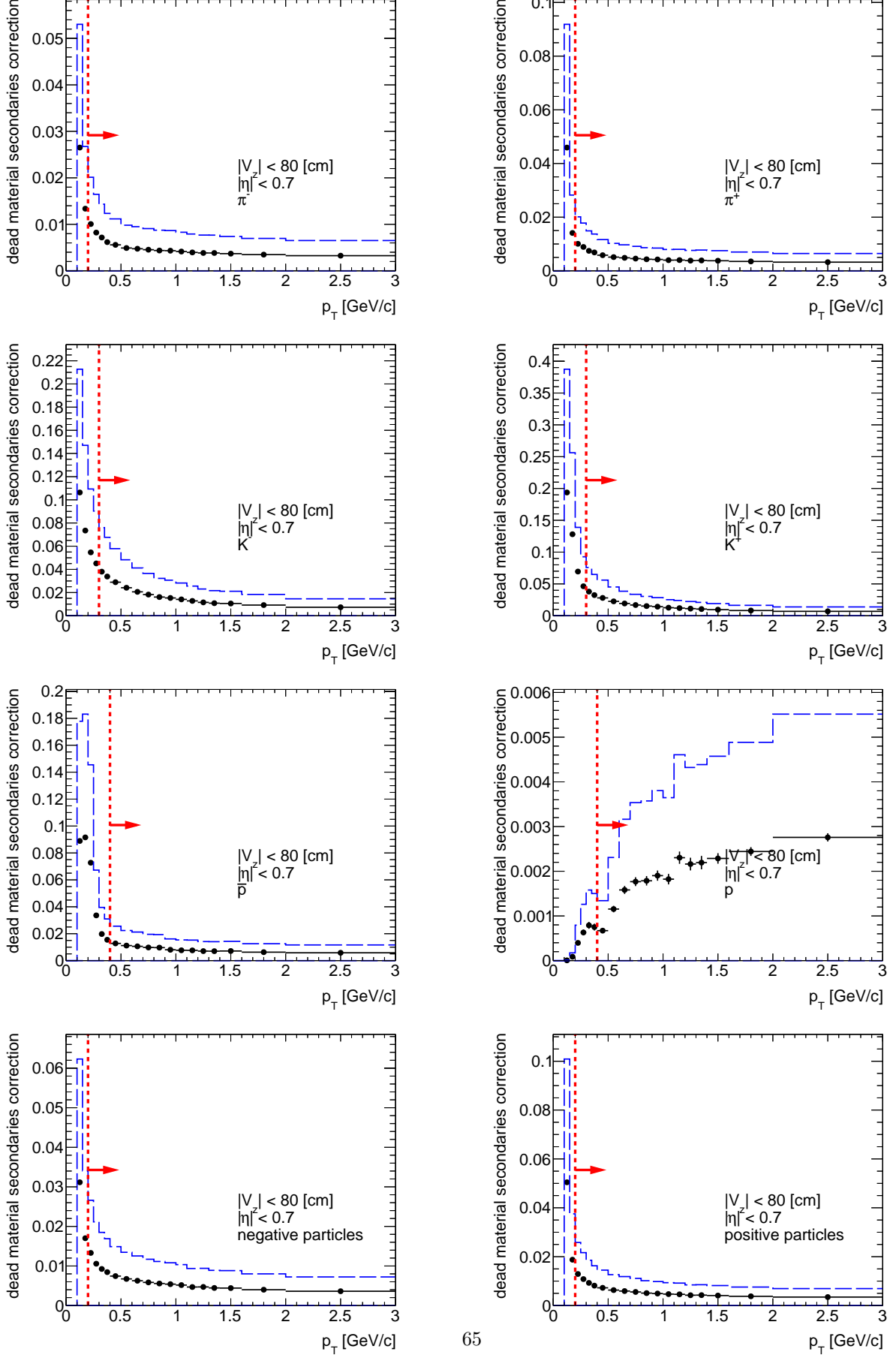


Figure B.16: The correction to the TPC track reconstruction efficiency $|0.2 \cdot \delta\epsilon_{TPC}|$ due to underestimated amount of dead material in front of TPC using MC samples for SD. Each plot represents the correction as a function of true particle p_T ($|\eta| < 0.7, |V_z| < 80$ cm) for given particle species: $\pi^-, \pi^+, K^-, K^+, \bar{p}$ and p . It was also calculated for negative and positive particles without identification. The corresponding systematic uncertainties are show with blue dotted lines.



List of Figures

1.1	TPC acceptance and reconstruction efficiency of π^- .	4
1.2	TPC acceptance and reconstruction efficiency of π^+ .	6
1.3	TPC acceptance and reconstruction efficiency of K^- .	8
1.4	TPC acceptance and reconstruction efficiency of K^+ .	10
1.5	TPC acceptance and reconstruction efficiency of \bar{p} .	12
1.6	TPC acceptance and reconstruction efficiency of p .	14
1.7	TOF acceptance, reconstruction and matching efficiency of π^- .	17
1.8	TOF acceptance, reconstruction and matching efficiency of π^+ .	19
1.9	TOF acceptance, reconstruction and matching efficiency of K^- .	21
1.10	TOF acceptance, reconstruction and matching efficiency of K^+ .	23
1.11	TOF acceptance, reconstruction and matching efficiency of \bar{p} .	25
1.12	TOF acceptance, reconstruction and matching efficiency of p .	27
4.1	Fits to dE/dx spectra from the data.	33
4.2	Parameters of track dE/dx as a function of reconstructed momentum for a few particle species.	34
4.3	Comparison of dE/dx spectra between data and MC.	35
5.1	Sketch of helix modification procedure and d_0 calculation.	36
5.2	Example of comparison of d_0 histograms in the data and embedded MC in the procedure of TPC pointing resolution adjustment.	37
5.3	Example of $-\chi^2/NDF$ map in a parameter space in the procedure of TPC pointing resolution adjustment.	37
5.4	Best-fit parameters obtained in the procedure of the TPC track pointing resolution adjustment.	37
5.5	Comparison of distribution of pion d_0 and components of DCA vector in the data and embedded MC, before and after adjustment of TPC pointing resolution.	38
6.1	39
6.2	40
6.3	41
6.4	41
7.1	Number of events in embedded MC as a function of BBC_AND rate.	42
7.2	π^\pm TPC track reconstruction efficiency as a function of p_T ($ \eta < 0.7, V_z < 80$ cm) for embedded MC samples with $<\text{BBC_AND}> = 700$ kHz and $<\text{BBC_AND}> = 1400$ kHz	42
7.3	The difference $\Delta\epsilon_{TPC} = \Delta\epsilon_{TPC}^{1400\text{ kHz}} - 2 \cdot \Delta\epsilon_{TPC}^{700\text{ kHz}}$ for π^\pm as a function of p_T and η ($ V_z < 80$ cm)	43
7.4	π^\pm TOF matching efficiency as a function of p_T ($ \eta < 0.7, V_z < 80$ cm) for embedded MC samples with $<\text{BBC_AND}> = 700$ kHz and $<\text{BBC_AND}> = 1400$ kHz	43
7.5	The difference $\Delta\epsilon_{TOF} = \Delta\epsilon_{TOF}^{1400\text{ kHz}} - 2 \cdot \Delta\epsilon_{TOF}^{700\text{ kHz}}$ for π^\pm as a function of p_T and η ($ V_z < 80$ cm)	44
7.6	The amount of lost π^- due to the interaction with dead material in front of TPC as a function of p_T , η and z -vertex in CD	45
7.7	The correction to the TPC track reconstruction efficiency $ 0.2 \cdot \delta\epsilon_{TPC} $ due to underestimated amount of dead material in front of TPC using MC samples for CD	47
B.1	The amount of lost π^+ due to the interaction with dead material in front of TPC as a function of p_T , η and z -vertex in CD	49
B.2	The amount of lost K^- due to the interaction with dead material in front of TPC as a function of p_T , η and z -vertex in CD	51
B.3	The amount of lost K^+ due to the interaction with dead material in front of TPC as a function of p_T , η and z -vertex in CD	52

B.4	The amount of lost \bar{p} due to the interaction with dead material in front of TPC as a function of p_T , η and z -vertex in CD	53
B.5	The amount of lost p due to the interaction with dead material in front of TPC as a function of p_T , η and z -vertex in CD	54
B.6	The amount of lost negative particles due to the interaction with dead material in front of TPC as a function of p_T , η and z -vertex in CD	55
B.7	The amount of lost positive particles due to the interaction with dead material in front of TPC as a function of p_T , η and z -vertex in CD	56
B.8	The amount of lost π^- due to the interaction with dead material in front of TPC as a function of p_T , η and z -vertex in SD	57
B.9	The amount of lost π^+ due to the interaction with dead material in front of TPC as a function of p_T , η and z -vertex in SD	58
B.10	The amount of lost K^- due to the interaction with dead material in front of TPC as a function of p_T , η and z -vertex in SD	59
B.11	The amount of lost K^+ due to the interaction with dead material in front of TPC as a function of p_T , η and z -vertex in SD	60
B.12	The amount of lost \bar{p} due to the interaction with dead material in front of TPC as a function of p_T , η and z -vertex in SD	61
B.13	The amount of lost p due to the interaction with dead material in front of TPC as a function of p_T , η and z -vertex in SD	62
B.14	The amount of lost negative particles due to the interaction with dead material in front of TPC as a function of p_T , η and z -vertex in SD	63
B.15	The amount of lost positive particles due to the interaction with dead material in front of TPC as a function of p_T , η and z -vertex in SD	64
B.16	The correction to the TPC track reconstruction efficiency $ 0.2 \cdot \delta\epsilon_{TPC} $ due to underestimated amount of dead material in front of TPC using MC samples for SD	65

List of Tables

4.1	Parameters of functions from Fig. 4.2 describing track dE/dx as a function of reconstructed momentum for a few particle species (STARsim MC).	33
-----	---------------------------------------------------------------------------------------------------------------------------------------------------------	----

References

- [1] https://github.com/rafalsikora/CEP-STAR-AnalysisNote/blob/master/CEP_AnalysisNote.pdf.
- [2] http://home.agh.edu.pl/~fulek/PID_AnalysisNote.pdf.
- [3] S. Das, “A simple alternative to the Crystal Ball function,” [arXiv:1603.08591 \[hep-ex\]](https://arxiv.org/abs/1603.08591).
- [4] <https://www.star.bnl.gov/rt3/SelfService/Display.html?id=3332>.